AB INITIO STUDY OF INORGANIC NANOWIRES

By

SHELLY L. ELIZONDO

Bachelor of Science in Mathematics
University of Central Oklahoma
Edmond, Oklahoma
2000

Master of Science in Natural and Applied Sciences
Oklahoma State University
Stillwater, Oklahoma
2005

Submitted to the Faculty of the
Graduate College of the
Oklahoma State University
in partial fulfillment of
the requirements for
the Degree of
DOCTOR OF PHILOSOPHY
July, 2006

AB INITIO STUDY OF INORGANIC NANOWIRES

Dissertation Approved:

Dr. John Mintmire
Dissertation Adviser

Dr. Tim Wilson

Dr. Paul Westhaus

Dr. Nicholas Materer

Dr. A. Gordon Emslie
Dean of the Graduate College

To Lee, my parents, and the rest of my family…

ACKNOWLEDGMENTS

I would like to acknowledge everyone who has helped make this research possible, especially my family for their support. I offer a special thanks to Lee, my husband and best friend of nearly 7 years, for believing in me, giving me the confidence to keep going, and most of all for continually making me laugh.

I offer a very special thank you to my advisor Dr. John Mintmire for providing me with the opportunity to work for him and undertake this research project. I am very thankful for his generosity, support, and seemingly infinite patience. He is truly an exceptional person and advisor. I recently came across a list of characteristics to look for in a good advisor. It came with a disclaimer stating that it is unreasonable to expect one person to have all these qualities. Therefore, I consider myself exceptionally lucky, as Dr. Mintmire possesses all of the qualities listed and more. To summarize, these traits involve: trustworthiness, good personal and communication skills, good technical skills, and respect by others in the field. I am very thankful for his guidance and expertise, for without it this research would not be possible.

I offer another very special thank you to Dr. Tim Wilson, who I consider my other advisor. He has supported me from the beginning of this venture, and for that I will always be grateful. We've shared some good times – St. Simons Island and key lime pie! What more can I say? I thank him for serving on my committee and offering his advice, knowledge, and support. This experience would not have been the same without him.

I also thank Dr. Paul Westhaus for being an extraordinary professor and serving on my committee. He is always willing to discuss a concept until the "light-bulb" comes on, even though developing such an understanding takes time and multiple office visits. I am grateful for his patience and willingness to share his knowledge.

I thank Dr. Nick Materer for serving on my committee. I sincerely appreciate the time he has spent on various committees throughout my graduate education.

I would like to thank the other members of the research group for their help and discussions about research. In particular, I would like to thank Dr. Thushari Jayasekera, Kirk Haines, and Vasantha Jogireddy.

I would like to thank the rest of the faculty and staff of the Physics Department, especially Susan Cantrell, Stephanie Hall, Cindy Raymond, and Warren Grider.

Finally, I thank the following for their financial support:

US Office of Naval Research

Naval Research Laboratory:

DoD HPCMO CHSSI program

NSF Oklahoma EPSCoR

NSF IGERT Program

University of Florida Quantum Theory Project:

IBM-Zerner Fellowship

TABLE OF CONTENTS

Chapter Page

1. INTRODUCTION 1

1.1 Overview 1

1.2 Low-Dimensional Structures 1

1.3 Organization of Dissertation 4

2. THEORETICAL APPROACH AND COMPUTATIONAL METHODS 6

2.1 Overview 6

2.2 DFT Methods 8

2.2.1 Basic Quantum Mechanics 8

2.2.2 Preliminaries to Modern DFT 9

2.2.3 Hohenberg-Kohn and Kohn-Sham Theorems 12

2.3 Band Structure Methods 15

2.4 Gaussian Basis Sets 19

2.5 Mulliken Population Analysis 21

2.6 First-Principles Optical Absorption Spectra 23

2.7 Computational Methods Used 25

2.7.1 NRL/OSU POLYXA 25

2.7.2 CRYSTAL03 29

3. HELICAL SILVER SINGLE-WALL NANOTUBES AND NANOWIRES 30

3.1 Introduction.....30

3.2 Computational Methods and Models.....34

3.2.1 Theoretical Approach.....34

3.2.2 Geometry and Notation of Silver Single-Wall Nanotubes 34

3.3 Method I: Conventional Helical Geometry and Unit Cell Sizes.....42

3.3.1 Overview.....42

3.3.2 Energetic Results 45

3.3.3 Band Structures, Densities of States, and Conduction Channels.....50

3.3.4 Orbital Densities 56

3.3.5 Summary and Conclusions 59

3.4 Method II: Strand by Strand – A Complementary Approach to Conventional Helical Symmetry.....60

3.4.1 Overview.....60

3.4.2 Energetic Results 61

3.4.3 Band Structures, Densities of States, and Conduction Channels.....64

3.4.4 Orbital Densities 66

3.4.5 Summary and Conclusions 68

3.5 Perspectives and Future Work 69

4. ZnO NANOSTRUCTURES

4.1 Introduction.....71

4.2 Computational Methods.....73

4.3 Nanotubes: Single-Wall.....74

4.3.1 Overview.....74

4.3.2 Geometries 75

4.3.3 Energetic Results 78

4.3.4 Band Structures and Densities of States 83

4.3.5 Optical Absorption Spectra 85

4.3.6 Structural Deformation Effects I:

Longitudinal, Transverse, and Shear Strain 95

4.3.7 Structural Deformation Effects II: Puckering 108

4.3.8 Summary of Results 113

4.4 Nanowires and Nanotubes: Bulk-Like 115

4.4.1 Overview 115

4.4.2 Geometries 116

4.4.3 Energetic Results 123

4.4.4 Band Structures and Densities of States 133

4.4.5 Optical Absorption Spectra 136

4.4.6 Summary of Results 141

4.5 Assessment of Results:

Single-Wall Nanotubes vs. Bulk-Like 1D Structures 143

4.6 A Comparative Analysis with POLYXA and Crystal03 144

4.6.1 Overview 144

4.6.2 Hexagonal Wurtzite in 3D 145

4.6.3 ZnO in a 2D Graphitc-Like Sheet 148

4.6.4 The (4,4) ZnOSWNT Revisited 150

4.6.5 Graphitic-Like Strips in 1D 153

4.6.6 Interpretation of Results.....157

4.7 Perspectives and Future Work 159

5. FINAL STATEMENTS.....160

BIBLIOGRAPHY.....162

LIST OF TABLES

Table Page

I. Total energies relative to the (5,2) AgNW 46

II. Total energies given by strand count relative to the (6,0) AgNW 62

III. The total energies per structure, listed by increasing radii 79

IV. Mulliken population analysis for ZnO single-wall nanotubes.....82

V. Energies of the first two excitation peaks due to parallel polarizations for ZnOSWNTs. 94

VI. Total energies of the ZnO Bulk-like nanotubes and nanowires 124

VII. Energies for the first two optical absorption peaks corresponding to parallel excitations for the ZnO bulk-like nanowires and nanotubes. 140

VIII. Total energies and band gaps of all ZnO nanotube and nanowire structures considered. 143

IX. Energetic results obtained in this study using Crystal03 along with selected results from literature for ZnO in the bulk hexagonal wurtzite structure 146

X. Total energy and band gap summary of 1D ZnO strips, along with the expected extrapolated energy for a 2D ZnO sheet. 155

XI. Summary of energetic results for ZnO structures.....158

LIST OF FIGURES

Figure Page

3-1. Triangular network of silver (or gold) atoms 36

3-2. Models of selected AgSWNTs and the (5,2) AgNW (AgSWNT + inserted silver atomic chain). 37

3-3. Triangular network of silver (or gold) atoms where two different notational styles are presented for comparison. 39

3-4. Model of the (5,0) AgNW (a) looking down the axis of the nanotube and (b) along the side. 44

3-5. Total energy per silver atom versus nanotube radius 45

3-6. Total energy per silver atom versus nanotube radius for all (n_1, 0) AgSWNTs 48

3-7. Total energy per silver atom versus nanotube radius for all (n_1 ,1) type AgSWNTs. 49

3-8. (a) Band structure and (b) density of states for the (7,1) AgSWNT.....51

3-9. (a) Band structure and (b) density of states for the (3,2) AgSWNT.....52

3-10. Band structure for the (3,2) AgSWNT shown within a zone-folding scheme. 53

3-11. Band structures for the (a) (4,3) AgSWNT, (b) silver atomic chain, and (c) the (7,4) AgNW. 55

3-12. Orbital densities for the (3,2) AgSWNT. 57

3-13. Orbital densities for the (a) (7,4) AgSWNT, (b) silver atomic chain, and (c) (7,4) AgNW. 58

3-14. (a-f) The (6,0) AgSWNT assembled strand by strand. (g) The (6,0) AgSWNT with an inserted silver chain along the axis of the nanotube. 60

3-15. Total energy versus the number of strands for $n_1 = n_2$ type structures. 63

3-16. (a-f) Band structures for the (6,0) AgSWNT, assembled strand by strand, corresponding to the respective structures in Figure 14.....65

3-17. Orbital densities for the (6,0) AgSWNT and AgNW. 67

4-1. Irreducible wedge of a honeycomb lattice indicating ZnO single-wall nanotube geometry 76

4-2. Ball and stick models of selected ZnO nanotubes: (a) (4,0) zigzag, (b) (4,4) armchair, and (c) (7,3) chiral nanotube 77

4-3. Total energy versus nanotube radius for all ZnOSWNTs 78

4-4. Change in atomic populations versus nanotube radius according to Mulliken population analysis data given in Table X 81

4-5. First-principles band structure and density of states for the (4,0) ZnOSWNT.....83

4-6. First-principles band structure and density of states for the (4,4) ZnOSWNT.....84

4-7. First-principles band structure and density of states for the (7,3) ZnOSWNT.....84

4-8. Optical absorption spectra and corresponding band structure and density of states for the (4,0) ZnOSWNT 87

4-9. Optical absorption spectra and corresponding band structure and density of states for the (4,4) ZnOSWNT 88

4-10. Optical absorption spectra and corresponding band structure and density of states for the (7,3) ZnOSWNT 89

4-11. Schematic of energies corresponding to the first two excitations in the (4,4) ZnOSWNT due to parallel polarizations.....91

4-12. Energies corresponding to the band gap and first two excitations due to parallel polarizations versus nanotube radius for all ZnOSWNTs 92

4-13. Zoomed-in perspective of the energies corresponding to the band gap and first excitation due to parallel polarizations versus nanotube radius for all ZnOSWNTs.....93

4-14. Total energy versus longitudinal strain for the (4,0), (4,4), and (7,3) ZnOSWNTs. 97

4-15. Total energy versus transverse strain for the (4,0), (4,4), and (7,3) ZnOSWNTs 97

4-16. Total energy versus shear strain for the (4,0), (4,4), and (7,3) ZnOSWNTs 98

4-17. Mulliken atomic population versus longitudinal strain for the (4,0), (4,4), and (7,3) ZnOSWNTs 99

4-18. Mulliken atomic population versus transverse strain for the (4,0), (4,4), and (7,3) ZnOSWNTs 100

4-19. Mulliken atomic population versus shear strain for the (4,0), (4,4), and (7,3) ZnOSWNTs 100

4-20. Changes in optical absorption spectra for the (4,0) ZnOSWNT due to transverse strain 101

4-21. E_1 optical absorption peak position versus longitudinal strain for the (4,0), (4,4), and (7,3) ZnOSWNTs. 102

4-22. E_1 optical absorption peak position versus transverse strain for the (4,0), (4,4), and (7,3) ZnOSWNTs. 102

4-23. E_2 optical absorption peak position versus longitudinal strain for the (4,0), (4,4), and (7,3) ZnOSWNTs. 103

4-24. E_2 optical absorption peak position versus transverse strain for the (4,0), (4,4), and (7,3) ZnOSWNTs. 103

4-25. Optical absorption spectra for the unstrained and shear strained (-0.10 ε_s) (4,0) ZnOSWNT 105

4-26. Optical absorption spectra for the unstrained and shear strained (-0.10 ε_s) (4,4) ZnOSWNT 106

4-27. Optical absorption spectra for the unstrained and shear strained (-0.10 ε_s) (7,3) ZnOSWNT 107

4-28. Puckered geometry of the (4,4) ZnOSWNT 109

4-29. Total energy versus change in oxygen radius for the (4,4) ZnOSWNT 110

4-30. Mulliken atomic population versus change in oxygen radius for the (4,4) ZnOSWNT....111

4-31. E_1 optical absorption peak position versus change in oxygen radius for the (4,4) ZnOSWNT....112

4-32. E_2 optical absorption peak position versus change in oxygen radius for the (4,4) ZnOSWNT....112

4-33. Ball and stick model of the ZnO wire segments constructed from the following bulk structures: hexagonal wurtzite and rocksalt....117

4-34. Schematic diagram illustrating nanotubes of the 3yH type....119

4-35. Schematic diagram illustrating nanotubes of the 6yH type....120

4-36. Models of the (1,2) 3yH ZnO nanotube....121

4-37. Models of the (2,3) 6yH ZnO nanotube....122

4-38. Total energies of the ZnO Bulk-like nanotubes and nanowires versus radius....124

4-39. Ball and stick model of the unit cell for the wurtzite structure ZnO wire. Charges associated with the Mulliken population analysis are indicated in units of *e*....127

4-40. Ball and stick model of the unit cell for the (1,2) 3yH ZnO nanotube. Charges associated with the Mulliken population analysis are indicated in units of *e*....127

4-41. Change in atomic populations versus distance from nanowire/nanotube origin for Zn and O atoms in the hexagonal wurtzite nanowire and the (1,2) 3yH nanotube, respectively....128

4-42. Ball and stick model of the unit cell for the (2,3) 6yH ZnO nanotube. Charges associated with the Mulliken population analysis are indicated in units of *e*....129

4-43. Change in atomic populations versus distance from nanotube origin for Zn and O atoms in the (2,3) 6yH ZnO nanotube....129

4-44. Ball and stick model of the unit cell for the rocksalt structure ZnO wire. Charges associated with the Mulliken population analysis are indicated in units of *e*....131

4-45. Ball and stick model of the unit cell for the rocksalt structure ZnO tube. Charges associated with the Mulliken population analysis are indicated in units of *e*. 131

4-46. Change in atomic populations versus distance from nanowire/nanotube origin for Zn and O atoms in the rocksalt nanowire and nanotube....132

4-47. Band structure and density of states for the hexagonal wurtzite ZnO nanowire 133

4-48. Band structure and density of states for the (1,2) 3yH ZnO nanotube 134

4-49. Band structure and density of states for the (2,3) 6yH ZnO nanotube 134

4-50. Band structure and density of states for the rocksalt ZnO nanowire.....135

4-51. Band structure and density of states for a rocksalt ZnO nanotube 135

4-52. Optical absorption spectra for a hexagonal wurtzite ZnO nanowire and the (1,2) 3yH nanotube....137

4-53. Optical absorption spectra for the (2,3) 6yH ZnO nanotube 138

4-54. Optical absorption spectra for a rocksalt ZnO nanowire and nanotube 139

4-55. First Brillioun Zone of the hexagonal wurtzite crystal structure.....147

4-56. Energy bands of ZnO in the hexagonal wurtzite crystal structure within the LDA approximation obtained using Crystal03. 147

4-57. Ball and stick model of a 2D ZnO sheet in a graphitic structure....149

4-58. Energy bands of ZnO in a 2D graphitic-like structure within the LDA approximation obtained using Crystal03 149

4-59. Energy bands of the (4,4) ZnO SWNT within the LDA approximation generated with POLYXA and CRYSTAL03....152

4-60. Ball and stick models of 1D Graphitic-Like ZnO Strips, periodic along the *z*-axis, depicted in (a – d) with increasing strip width....153

4-61. Band structures obtained using POLYXA for the ZnO 1D strips in a graphitic configuration with (a) 5, (b) 7, (c) 9, and (d) 11 ZnO atom pairs per unit cell. 156

CHAPTER 1

INTRODUCTION

1.1 Overview

Since the discovery of carbon nanotubes by Iijima,[1] research involving nano-scale quasi one-dimensional materials has increased at a revolutionary pace. The wide range of current applications and potential devices drives the need for a better theoretical understanding of these novel materials. Two types of inorganic one-dimensional structures are considered herein: silver and zinc-oxide nanotubes and nanowires. Through undertaking this study, we explore some of the lesser understood characteristics of these materials, including their electronic structures and unique optical properties. We begin by introducing the defining characteristics of low-dimensional materials along with their distinctive properties and applications. The remainder of this chapter introduces the topics comprising this dissertation. We present the theoretical background and computational methods employed, and we introduce the separate studies regarding silver and zinc-oxide quasi one-dimensional structures, the primary focus of this work.

1.2 Low-Dimensional Structures

Nanotechnology encompasses structures with dimensions on the order of a nanometer, one-billionth of a meter, and one thousand times smaller than a micron. A material may be classified as a nanomaterial if at least one dimension is confined on the

order of 1 to 100 nanometers. These materials may be confined in all three spatial dimensions, two dimensions, or only one dimension. The dimensionality of the material refers to how many dimensions are unconstrained, or free to extend periodically, as such crystalline bulk materials are three-dimensional. Materials with all three spatial dimensions confined to the nanoscale are zero-dimensional materials called quantum dots. If only one dimension is constrained to the nanoscale, the material is two-dimensional and is termed a quantum well. If two dimensions are constrained to the nanoscale, the material is one-dimensional. Examples of these materials are nanowires or nanotubes, and are the focus of this dissertation.

Meeting the current and future needs of nanoscale electronic devices, will require a better understanding of the components associated with these devices. Novel properties of materials can arise when the size and dimensionality are reduced. These unique properties include: quantum confinement, mechanical and thermal stability, lasing, phonon transport, photoconductivity and chemical sensing, magnetic effects, and electronic and ionic transport.[2] Changes in the electronic properties upon reducing the dimensionality and varying the geometries of the materials are the primary focus of this work.

Nanotechnology will have an extensive impact on many aspects of our lives due to current and potential applications including electronic devices, national security, and even health care. Silver nanowires have uses ranging from interconnects to chemical sensing.[2] P. Yang reported Langmuir-Blodgett silver nanowire monolayers for molecular sensing using Surface-Enhanced Raman Spectroscopy (SERS) where they successfully demonstrated their use for the detection of 2,4 – dinitrotoluene (2,4 – DNT),

the nitroaromatic compound most commonly used as a marker for detecting buried landmines and other explosives.[3]

The optical properties of these materials are directly linked to size-induced changes in the electronic structure. Zinc oxide is one of the few oxides that show quantum confinement effects in an experimentally accessible size range (<8nm), which makes it a particularly promising material.[2] Yin et al, [4] observed quantum confinement effects in ZnO nanorods with radii of 1.1 ± 0.1 nm, smaller than the exciton Bohr radius of approximately 2.34 nm. In semiconductors, size confinement effects can result in bandgap tunability. Wang et al. reported a 120 meV blueshift in the spectra of ZnO nanobelts with widths of 200 nm and 6 nm.[5]

Zinc oxide has a wide range of applications from use in sunscreen lotion to use in sensors and photovoltaics.[6] Due to many unique properties including versatile geometrical configurations and a vast array of novel applications, ZnO is predicted to become one of the most widely used one-dimensional nanostructures.[7] As an added bonus, ZnO is "bio-friendly" and is very stable under high-energy radiation, indicating possible uses in medicine and space-oriented applications.[7-9] Applications pertaining to nanotechnology will likely have a widespread influence on health care as they are expected to revolutionize cancer diagnostics, imaging, and treatment which could ultimately lead to an era of personalized medicine.[10] These potentially life-changing applications serve as inspiration as we explore the modifications in the properties upon reducing the dimensionality and varying the structures of these materials.

1.3 Organization of Dissertation

Chapter 2 provides details regarding the theoretical background and the computational methods utilized throughout this dissertation. We briefly review the theoretical formalism underlying the work carried out herein of density functional theory (DFT), band structure methods and Gaussian basis sets. Next, we discuss the computational methods used including the NRL/OSU POLYXA code and CRYSTAL03 [11].

Chapter 3 presents results from a study carried out on helical silver single-wall nanotubes and nanowires. The primary motivation for this study was the experimental work reported by Takayanagi and co-workers for constructing helical gold nanowires and a single-wall gold nanotube, with diameters as small as 0.40 nm.[12, 13] Herein, we elected to model similar geometrical systems using silver instead of the more complex systems involving gold. In this study, we address similar trends in our first-principles electronic structure results compared with other theoretical work using gold and silver. We have published results pertaining to this study in the refereed literature.[14-16]

Chapter 4 describes the study carried out involving ZnO nanotubes and nanowires. ZnO is a direct band-gap (E_g = 3.37 eV) semiconductor with a large exciton binding energy (60meV), exhibiting near-UV emission, transparent conductivity, and piezoelectricity. ZnO, a very versatile II-VI semiconductor material, can form a variety of nanostructures including: nanodots, nanorods, nanowires, nanobelts, nanotubes, nanobridges and nanonails, nanowalls, nanohelixes, nanorings, and nanocages.[17-26] In a recent theoretical study, a new energetically favorable 'graphitic-like' structure was predicted for ZnO thin films.[27] These findings raise the possibility of ZnO existing in

single-wall structures similar to carbon nanotubes. Herein, we examine the electronic properties for different geometrical configurations of ZnO including: single-wall graphitic-like nanotubes, single-wall bulk-like nanotubes, and ultrathin nanowires. The optical cross sections are calculated using an Ehrenreich – Cohen formalism.[28] The single-wall graphitic-like structures are the primary focus, with the nanotubes and nanowires with bulk-like geometries used primarily for comparison. Portions of this chapter will be submitted for publication.

Chapter 5 provides a final overview of the dissertation, emphasizing the highlights and the most relevant findings. We discuss the results from the helical silver nanotube and nanowire study, presented in Chapter 3. A few closing remarks are made concerning the zinc oxide nanostructure study, presented in Chapter 4.

CHAPTER 2

THEORETICAL APPROACH AND COMPUTATIONAL METHODS

2.1 Overview

The electronic and structural properties of quasi one-dimensional systems are modeled within the framework of density functional theory (DFT). The fundamental theoretical background is discussed, including basic quantum mechanics and the theorems of Hohenberg-Kohn and Kohn-Sham, along with band structure methods. A description of the computational methods follow, including the framework behind the NRL/OSU POLYXA code and CRYSTAL03 [29].

Most of the simulations reported in this work have used the NRL/OSU POLYXA code, developed by Mintmire and colleagues at the Naval Research Laboratory and Oklahoma State University. This computational package models the electronic structures of quasi-one-dimensional systems using first-principles calculations. [30-32] This software differs from other available software in that it has been adapted for helical symmetry and can therefore model a broader range of structures. Employing helical symmetry allows for the use of a smaller unit cell size which is particularly important for calculations pertaining to chiral systems with helical periodicity. Applying purely translational symmetry to such systems can require excessively large unit cell sizes, greatly increasing the computational expense. Reducing the computational size of the

electronic structure calculation using helical symmetry is a unique approach, first proposed by Imamura and Fujita [33, 34] for semiempirical methods and further developed by Mintmire and colleagues at the NRL. This approach has proven successful in a range of applications with polymers and carbon nanotubes; perhaps most notable is the prediction of metallic carbon nanotubes prior to experimental observation.[35]

The CRYSTAL03 package, developed at the University of Torino, has also been used in our study. This software package models systems with 0D, 1D, 2D, and 3D using purely translational periodicity, was implemented in the ZnO study primarily for the purposes of better interpreting our results.

2.2 DFT Methods

2.2.1 Basic Quantum Mechanics

The time-independent non-relativistic Schrödinger equation is expressed as,

$$\hat{H}\,\Psi_i(\vec{x}_1,\vec{x}_2,...,\vec{x}_N,\,\vec{R}_1,\vec{R}_2,...,\vec{R}_M) = E_i\Psi_i(\vec{x}_1,\vec{x}_2,...,\vec{x}_N,\,\vec{R}_1,\vec{R}_2,...,\vec{R}_M) \quad (2.1)$$

where $\hat{H}$ is the Hamiltonian operator for a molecular system with *N* electrons and *M* nuclei.

$$\hat{H} = -\frac{1}{2}\sum_{i=1}^{N}\nabla_i^2 - \frac{1}{2}\sum_{A=1}^{M}\frac{1}{M_A}\nabla_A^2 - \sum_{i=1}^{N}\sum_{A=1}^{M}\frac{Z_A}{r_{iA}} + \sum_{i=1}^{N}\sum_{j>i}^{N}\frac{1}{r_{ij}} + \sum_{A=1}^{M}\sum_{B>A}^{M}\frac{Z_A Z_B}{R_{AB}} \qquad (2.2)$$

E_i is the numerical value of the energy of the state described by the wave function Ψ_i which contains all the information about the quantum system. The Born-Oppenheimer approximation further simplifies the Schrödinger equation. Because the massive nuclei move much slower than the electrons, the electrons are considered as moving in the field of fixed nuclei. Equation (2.1) reduces to what is known as the electronic Schrödinger equation where $\hat{H}_{elec}$ is the electronic Hamiltonian.

$$\hat{H}_{elec} = -\frac{1}{2}\sum_{i=1}^{N}\nabla_i^2 - \sum_{i=1}^{N}\sum_{A=1}^{M}\frac{Z_A}{r_{iA}} + \sum_{i=1}^{N}\sum_{j>i}^{N}\frac{1}{r_{ij}} = \hat{T}_e + \hat{V}_{Ne} + \hat{V}_{ee} \qquad (2.3)$$

where T_e is the kinetic energy of the electrons, V_{Ne} is the electron-nuclear attractive Coulomb potential, and V_{ee} is the electron-electron repulsive Coulomb potential. Together with the electronic wave function, ψ_{elec}, which is dependent upon the electronic coordinates, the electronic Schrödinger equation is expressed as

$$\hat{H}_{elec}\psi_{elec} = E_{elec}\psi_{elec} \qquad (2.4)$$

The Schrödinger equation can only be solved exactly for the simplest one-electron systems, therefore one has to rely on approximate methods to solve most systems of interest.

With these aspects in mind, we pursue the development of density functional theory. The following references were consulted [31, 36-40] and can provide more rigorous derivations too lengthy for this overview.

2.2.2 Preliminaries to Modern DFT

Before introducing the more prevalent concepts associated with density functional theory, we must first take a step back in time and address some preliminary concepts including the Thomas-Fermi model along with Dirac's local exchange approximation. [39] The approximations that Thomas and Fermi made were in the calculation of the density of states and the kinetic energy. Start with the Fermi distribution function

$$f_i = \frac{1}{\exp(\varepsilon_i - \varepsilon_F)/kT + 1}\ , \qquad (2.5)$$

which means that at the absolute zero temperature all one-electron energy levels with energy below ε_f will be occupied with $f_i = 1$, and all one-electron energy levels above ε_f will be empty, with $f_i = 0$. Thomas and Fermi obtained the charge density at an arbitrary point in space by assuming that the electron distribution in the neighborhood of that point could be treated as part of a homogeneous electron gas. If all the states with energy less than *E* are occupied, and if we take into account the two orientations of spin and charge of an electron, the charge density can be expressed as

$$\rho = -e\frac{8\pi}{3h^3}(2mE)^{3/2} \qquad (2.6)$$

with *e* being the magnitude of the electronic charge. Homogenous electron gas theory indicates that at the point where the potential is V(r), electrons have kinetic energies from zero up to *e*V(r), so that the total energy of the electron with maximum kinetic energy is zero. The assumption that Thomas and Fermi made was that the charge density of electrons at this point was

$$\rho = -e\frac{8\pi}{3h^3}[2meV(r)]^{3/2} \qquad (2.7)$$

Within their method, an electron in an *N*-electron atom would move in the field of the nucleus and all *N* electrons, rather than in the field of *N*-1 electrons. Dirac developed a method to overcome this difficulty by adding an exchange term proportional to the cube root of the charge density. In 1951, Slater suggested a model in which the kinetic energy would be treated as in the Hartree-Fock model, but where the statistical approximation would be used for the exchange term.[41] This work led to what is known as the Xα – SCF method. Slater obtained the one-electron exchange potential, in Hartree atomic units,

$$V_x = -3(3\rho/4\pi)^{1/3} \qquad (2.8)$$

where ρ is the total electronic charge density.

In 1954, Gáspár published a paper in which he obtained the same kind of dependence of the exchange correlation energy on the charge density, but instead of the coefficient of $3(3/4\pi)^{1/3}$ he found a coefficient of only two-thirds the value, or $2(3/4)^{1/3}$. This is an interesting piece of information, as Gáspár seems to get lost in the shuffle these days, with Kohn and Sham getting most of the credit. In fact, very little attention was paid to Gáspár's paper at the time, as nobody had a way to make practical use of it. Eleven years after Gáspár's paper, Kohn and Sham, unaware of Gáspár's work, again

found the coefficient two-thirds the size of Slater's. Interestingly, Slater had noticed Gáspár's result and thought his arguments were valid. In one of his books, Slater addresses the discrepancy in detail, concluding that his method is suitable for one-electron energies, but the other method is more appropriate for treating the total energy of the system.[39] The approach became known as the Xα method (X for exchange and α for the parameter), where the exchange-correlation term is written in the form

$$-3\alpha\left(\frac{3}{4\pi}\right)^{1/3}\rho^{1/3} \qquad (2.9)$$

with $\alpha = 1$ for Slater's original value and $\alpha = \frac{2}{3}$ for that of Gáspár, Kohn, and Sham.

Our LDF approach, described in section 2.7.1, employs the Gáspár-Kohn-Sham exchange-correlation potential. This approach is also commonly referred to as the local density approximation (LDA). Next we review the breakthroughs of Hohenberg, Kohn, and Sham, which laid the foundation for DFT.

2.2.3 Hohenberg-Kohn and Kohn-Sham Theorems

The basic idea behind DFT is that a relationship exists between the total electronic energy and the overall electronic density. Hohenberg and Kohn showed that the ground-state energy and other properties of a system could be uniquely determined by the electron density.[42] Hohenberg and Kohn also showed that there exists a universal functional $F[\rho(\vec{r})]$ such that, for a given external potential $\upsilon_{ext}(\vec{r})$, the actual ground state energy *E* and charge density $\rho(\vec{r})$ are obtained by minimizing an unknown energy functional, given below, with respect to variations in the charge density.

$$E[\rho(\vec{r})] = F[\rho(\vec{r})] + \int \upsilon_{ext}(\vec{r})\rho(\vec{r})\, d^3r \qquad (2.10)$$

The charge density of the system is the sum of the squares of a set of one-electron orthonormal orbitals:

$$\rho(\vec{r}) = \sum_{i=1}^{N} \left|\psi_i(\vec{r})\right|^2 \qquad (2.11)$$

Before the energy is minimized, a constraint is placed on the electron density as the number of electrons (*N*) is fixed:

$$N = \int \rho(\vec{r})\, d\vec{r} \qquad (2.12)$$

To proceed with minimizing the energy, this constraint is introduced as a Lagrangian multiplier ($-\mu$)

$$\frac{\delta}{\delta\rho(\vec{r})}\left[E[\rho(\vec{r})] - \mu\int \rho(\vec{r})d\vec{r}\right] \qquad (2.13)$$

From Eq. 2.13 the Lagrangian multiplier is expressed as:

$$\left(\frac{\delta E[\rho(\vec{r})]}{\delta\rho(\vec{r})}\right)_{\upsilon_{ext}(\vec{r})} = \mu \qquad (2.14)$$

This equation (Eq. 2.14) is the DFT equivalent of the Schrödinger equation.

In their landmark paper, Kohn and Sham[43] devised a practical way to solve the Hohenberg-Kohn[42] theorem for a set of interacting electrons. Kohn and Sham suggested that the functional $F[\rho(\vec{r})]$ should be approximated as the sum of three terms: the kinetic energy $E_{KE}[\rho(\vec{r})]$, the electron-electron Coulombic energy $E_H[\rho(\vec{r})]$, and the exchange and correlation energy $E_{XC}[\rho(\vec{r})]$:

$$F[\rho(\vec{r})] = E_{KE}[\rho(\vec{r})] + E_H[\rho(\vec{r})] + E_{XC}[\rho(\vec{r})] \qquad (2.15)$$

The kinetic energy term is defined as the kinetic energy of a system of *non-interacting* electrons with the same density $\rho(\vec{r})$ as the real system:

$$E_{KE}[\rho(\vec{r})] = \sum_{i=1}^{N}\int \psi_i(\vec{r})\left(-\frac{\nabla^2}{2}\right)\psi_i(\vec{r})\,d\vec{r} \qquad (2.16)$$

The electron Coulombic energy term is also known as the Hartree electrostatic energy. This electrostatic energy arises from the classical interaction between two charge densities; when summed over all possible pairwise interactions it is expressed as:

$$E_H[\rho(\vec{r})] = \frac{1}{2}\int\int \frac{\rho(\vec{r}_1)\rho(\vec{r}_2)}{|r_1 - r_2|}\,d\vec{r}_1\,d\vec{r}_2 \qquad (2.17)$$

Upon combining these two terms and adding the electron-nuclear interaction, the full expression for the energy becomes

$$\begin{aligned} E[\rho(\vec{r})] = &\sum_{i=1}^{N}\int \psi_i(\vec{r})\left(-\frac{\nabla^2}{2}\right)\psi_i(\vec{r})d\vec{r} + \frac{1}{2}\iint \frac{\rho(\vec{r}_1)\rho(\vec{r}_2)}{|\vec{r}_1 - \vec{r}_2|}d\vec{r}_1 d\vec{r}_2 \\ &+ E_{XC}[\rho(\vec{r})] - \sum_{A=1}^{M}\int \frac{Z_A}{|\vec{r} - \vec{R}_A|}\rho(\vec{r})d\vec{r} \end{aligned} \qquad (2.18)$$

Upon introducing this expression for the electron density and applying the appropriate variational condition, the following one-electron Kohn-Sham equations result (adding the electron-nuclear interactions):

$$\left\{-\frac{\nabla_1^2}{2}-\left(\sum_{A=1}^{M}\frac{Z_A}{r_{1A}}\right)+\int\frac{\rho(\vec{r}_2)}{r_{12}}d\vec{r}_2+V_{XC}[\vec{r}_1]\right\}\psi_i(\vec{r}_1)=\varepsilon_i\psi_i(\vec{r}_1) \qquad (2.19)$$

The orbital energies are ε_i, and the exchange-correlation functional is given by V_{XC}, which is related to the exchange-correlation energy by

$$V_{XC}[\vec{r}]=\left(\frac{\delta E_{XC}[\rho(\vec{r})]}{\delta\rho(\vec{r})}\right) \qquad (2.20)$$

The Kohn-Sham equations are solved self-consistently.

The exchange-correlation functional is unknown. Kohn and Sham proposed the local-density approximation (LDA) to deal with this problem,

$$E_{XC}\approx E_{XC}^{LDA}=\int\rho(\vec{r})\varepsilon_{xc}^{\text{hom}}(\rho(\vec{r}))d^3r \qquad (2.21)$$

where $\varepsilon_{xc}^{\text{hom}}$ is the exchange-correlation energy per particle in the homogeneous electron gas. There are a broad range of density functionals available, but LDA was used throughout the current work.

2.3 Band Structure Methods

We have presented the basics behind density functional theory for atoms and molecules, and now we must incorporate extended systems into this discussion. We first introduce Bloch's theorem and explain the linear combination of atomic orbitals (LCAO) approach for modeling band structures. The following references were consulted and provide a nice review of the concepts described: Refs.[44] and [45].

Bloch's theorem describes electrons in solids moving about in a periodic potential. The theorem proves that the solutions of the Schrödinger equation for a periodic potential can be expressed in the form:

$$\psi_k(\vec{r}) = u_k(\vec{r})\exp(i\vec{k}\cdot\vec{r}), \qquad (2.22)$$

where $u_k(\vec{r})$ has the period of the crystal lattice with $u_k(\vec{r}) = u_k(\vec{r}+\vec{T})$. The eigenfunctions of the wave equation for a periodic potential are the product of a plane wave $\exp(i\vec{k}\cdot\vec{r})$ times a function $u_k(\vec{r})$ with the periodicity of the crystal lattice. The value of $\vec{k}$ is used as an index to label the eigenfunction ψ_k; it is called the Bloch wave vector and $\hbar\vec{k}$ is the crystal momentum. For a given value of $\vec{k}$, there may exist many energy eigenvalues, which are frequently labeled by a band index *n*, expressed in Dirac notation as:

$$\hat{H}\left|\psi_{nk}\right\rangle = \varepsilon_{nk}\left|\psi_{nk}\right\rangle, \qquad (2.23)$$

where ε_{nk} are the band energies. There are various methods available to calculate these band energies including: pseudopotentials and orthogonalized plane waves (OPW), linear combination of atomic orbitals (LCAO), linear augmented plane waves (LAPW), and linearized muffin tin orbitals (LMTO).

We implement the LCAO approach throughout this work, and describe it in the remainder of this section. The one-dimensional periodicity present in nanowires and nanotubes results in a delocalization of electron states like that in crystals, but the finiteness in other dimensions calls for the use of localized wavefunctions as in molecular approaches, making an LCAO approach the natural choice for one-dimensional systems. The approach has been modified for the use of helical symmetry, and as such it is described within that context. If one wishes to use purely translational symmetry, the screw operator, described as follows, may be replaced by the translational operator. Reducing the computational size of the electronic structure calculation using helical symmetry is an approach, first proposed by Imamura and Fujita [33, 34] for semiempirical methods and further developed by Mintmire and colleagues at NRL for use in first-principles calculations. The following references provide additional information [30, 31, 46-49].

Analogous to a translation operator used in translational systems, a screw operator is used in helical systems. We define a screw operation S in terms of a translation h units down the z axis along with a right-handed rotation ϕ about the z axis:

$$S(h,\phi)\vec{r} \equiv \begin{pmatrix} x\cos\phi - y\sin\phi \\ x\sin\phi + y\cos\phi \\ z + h \end{pmatrix} \tag{2.24}$$

The symmetry group generated by the screw operation S is isomorphic with the one-dimensional translation group. Bloch's theorem can therefore be generalized so that the one-electron wavefunctions will transform under S according to:

$$S^m \psi_i(\vec{r};\kappa) = \exp(i\kappa m)\psi_i(\vec{r};\kappa)\,. \tag{2.25}$$

The quantity κ is a dimensionless quantity which is conventionally restricted to a range of $-\pi < \kappa \leq \pi$, a central Brillouin zone, and the quantity *m* represents the m^{th} unit cell. If $\phi = 0$, *S* represents a pure translation, and κ corresponds to *k*, the traditional wavevector from Bloch's theorem in solid-state band-structure theory.

The one-electron wavefunctions ψ_i are constructed from a linear combination of Bloch functions φ_j, which are constructed from a linear combination of nuclear-centered Gaussian-type orbitals χ_j,

$$\psi_i(\vec{r};\kappa) = \sum_j c_{ji}(\kappa)\varphi(\vec{r};\kappa) \tag{2.26}$$

$$\varphi_j(\vec{r};\kappa) = \sum_m \exp(-i\kappa m) S^m \chi_j(\vec{r}) . \tag{2.27}$$

The one-electron density matrix is then given by

$$\rho(\vec{r};\vec{r}') = \sum_i \frac{1}{2\pi} \int_{-\pi}^{\pi} d\kappa\, n_i(\kappa) \psi_i^*(\vec{r}';\kappa)\psi_i(\vec{r};\kappa) \tag{2.28}$$

$$= \sum_{jj'} \sum_m P_{j'j}^m \sum_{m'} \chi_{j'}^{m+m'}(\vec{r}')\, \chi_j^{m'}(\vec{r}) , \tag{2.29}$$

where $n_i(\kappa)$ are the occupation numbers of the one-electron states, χ_j^m denotes $S^m \chi_j(\vec{r})$, and P_{ij}^m are the coefficients of the real lattice expansion of the density matrix given by

$$P_{j'j}^m = \sum_i \frac{1}{2\pi} \int_{-\pi}^{\pi} d\kappa\, n_i(\kappa) c_{j'i}^*(\kappa) c_{ji}(\kappa) \exp(i\kappa m) \tag{2.30}$$

The total energy for the system is given by

$$
\begin{aligned}
E = & \sum_{ij}\sum_{m} P_{ij}^{m}\left\{-\frac{1}{2}\left\langle \chi_i^m \middle| \nabla^2 \middle| \chi_j^0 \right\rangle + \left\langle \chi_i^m \middle| \varepsilon_{xc}[\rho(\vec{r})] \middle| \chi_j^0 \right\rangle\right\} \\
& + \frac{1}{2}\sum_{m''}\left\{\left(\sum_{n}\sum_{n'}\frac{Z_n Z_{n'}}{\left|\vec{R}_n^0 - \vec{R}_{n'}^{m''}\right|}\right)\right. \\
& + \sum_{ij}\sum_{m} P_{ij}^{m}\left(\sum_{i'j'}\sum_{m'} P_{i'j'}^{m'}[\chi_i^m \chi_j^0 \,|\chi_{i'}^{m'+m''} \chi_{j'}^{m''}]\right. \\
& \left.\left. - 2\sum_{n}\left\langle \chi_i^m \middle| \frac{Z_n}{\left|\vec{r} - \vec{R}_n^{m''}\right|} \middle| \chi_j^0 \right\rangle\right)\right\}
\end{aligned}
\tag{2.31}
$$

where Z_n and $\vec{R}_n$ denote the nuclear charges and coordinates within a single unit cell, $\vec{R}_n^m$ denotes the nuclear coordinates in unit cell m ($\vec{R}_n^m \equiv S^m \vec{R}_n$), and $[\rho_1 \mid \rho_2]$ denotes the electrostatic interaction integral

$$
[\rho_1 \mid \rho_2] \equiv \int d^3 r_1 \int d^3 r_2 \, \frac{\rho_1(\vec{r}_1)\rho_2(\vec{r}_2)}{r_{12}} \,. \tag{2.32}
$$

2.4 Gaussian Basis Sets

Basis sets composed of atomic functions are often used in quantum mechanical calculations. The following discussion is adapted from Ref. [37]. Slater type orbitals would be suitable, but many of the required integrals are difficult, if not impossible, to calculate. It is therefore common to use Gaussian functions which have the form $\exp(-\alpha r^2)$, comprised of integral powers of x, y and z multiplied by $\exp(-\alpha r^2)$,

$$x^a y^b z^c \exp(-\alpha r^2) \tag{2.33}$$

where α determines the spread of the function. The order of the function is determined by the summation of the powers of the Cartesian variables. For example, a zeroth-order function has $a+b+c=0$ and a first-order function has $a+b+c=1$. Replacing a Slater type orbital by a single Gaussian function leads to undesirable errors. This problem is overcome by representing each atomic basis function as a linear combination of Gaussian functions. Each linear combination has the form

$$\phi_\mu = \sum_{i=1}^{L} d_{i\mu}\phi_i(\alpha_{i\mu}) \tag{2.34}$$

where $d_{i\mu}$ is the coefficient of the primitive Gaussian function ϕ_i which has the exponent $\alpha_{i\mu}$.

A Gaussian expansion has two parameters: the coefficient and the exponent. These Gaussians can be uncontracted (primitive) or contracted. Calculations with primitive Gaussians are computationally more expensive. Therefore basis sets that consist of contracted Gaussian functions are commonly used. In a contracted function the coefficients and exponents are predetermined and remain constant during the calculation.

A minimal basis set contains just the number of functions that are required to accommodate all the filled orbitals in each atom. It is found that at least three Gaussian functions are required to minimally represent each Slater type orbital, therefore the STO-3G basis set is considered the 'absolute minimum'. A *double zeta* basis set doubles the number of functions in the minimal basis set. A *split valence* basis set is an alternative to the double zeta basis approach in which the number of functions used to describe the valence electrons is doubled but a single function is used for the inner shells. The reasoning is that the valence orbitals have a greater affect on chemical properties. In the 3-21G basis set, three Gaussian functions describe the core orbitals. The valence electrons are also represented by three Gaussians: the contracted part by two Gaussians and the diffuse part by one Gaussian. Throughout this work, we use a 3-21G split valence set to model the silver nanotubes and nanowires discussed in Chapter3, and we use 6-31G split valence basis sets to model zinc-oxide nanotubes and nanowires in the study presented in Chapter 4.

2.5 Mulliken Population Analysis

Population analysis partitions the electron density of the nuclei in a system so that each nucleus has a number of electrons associated with it, although not necessarily an integral number. This method offers a way to calculate the atomic charge on each nucleus. The partitioning scheme is arbitrary, and consequently many methods exist. Herein, we employ the approach proposed by R. S. Mulliken in which the contribution is equally partitioned between two atoms.[50] Refs. [36] and [37] provide a detailed background of this topic.

We begin our discussion with the equation below which relates the total number of electrons, N, to the density matrix, P, and to the overlap integrals, S

$$N = \sum_{\mu=1}^{K} P_{\mu\mu} + 2\sum_{\mu=1}^{K}\sum_{\nu=\mu+1}^{K} P_{\mu\nu}S_{\mu\nu} \qquad (2.35)$$

All of the electron density $P_{\mu\mu}$ in an orbital is allocated to the atom on which ϕ_μ originates, while the remaining electron density is related the overlap population, $\phi_\mu\phi_\nu$. For each element $\phi_\mu\phi_\nu$ of the density matrix, half of the density is assigned to the atom on which ϕ_μ is located and half to the atom on which ϕ_ν is located. The net charge on an atom A is then calculated by subtracting the number of electrons from the nuclear charge, Z_A [37]:

$$q_A = Z_A - \sum_{\mu=1;\,\mu\,on\,A}^{K} P_{\mu\mu} - \sum_{\mu=1;\,\mu\,on\,A}^{K}\sum_{\nu=1;\nu\neq\mu}^{K} P_{\mu\nu}S_{\mu\nu} \qquad (2.36)$$

The Mulliken population analysis depends on the use of a balanced basis set, in which an equivalent number of basis functions is present on each atom in the molecule, and it assumes that basis functions are centered on the nuclei. The atomic charges are

dependent upon the basis set being used. Although we can accurately compare our results with other results obtained within this study, caution should be used when comparing our conclusions with those presented elsewhwere.

2.6 First-Principles Optical Absorption Spectra

We have calculated the optical absorption spectra of ZnO quasi one-dimensional systems using an Ehrenreich-Cohen perturbation theory approach using the LDF electronic structure results.[28, 51] The approach used here, implemented in the NRL/OSU POLYXA code, has been discussed in detail elsewhere.[31, 32, 52] The optical cross sections are calculated as the imaginary component of the dielectric response tensor in the long wavelength limit,

$$\varepsilon_2^{\alpha\beta}(\omega) = \frac{2\pi\hbar e^2}{m\omega\Omega}\sum_{k,k'} f_{k,k'}^{\alpha\beta}\,\delta(\varepsilon_{k'} - \varepsilon_k - \hbar\omega) \qquad (2.37)$$

using a notation similar to that used by Harrison.[53] The summation in Eq. 2.37 is over occupied electron states at *k* and unoccupied states at *k'*, and Ω represents the volume of the unit cell. The quantities $f_{k,k'}^{\alpha,\beta}$ are dimensionless oscillator strengths given in terms of the matrix elements of the gradient operator

$$f_{k,k'}^{\alpha\beta} = \frac{2\hbar^2}{m\,(\varepsilon_{k'} - \varepsilon_k)} P_{k,k'}^{\alpha} P_{k',k}^{\beta}; \qquad (2.38)$$

where

$$P_{k,k'}^{\alpha} = \left\langle \psi_k \left| \frac{\partial}{\partial x_\alpha} \right| \psi_{k'} \right\rangle. \qquad (2.39)$$

Herein, we consider the diagonal elements of the dielectric tensor of the form $\varepsilon_2^{\alpha\alpha}(\omega)$. For polarizations parallel to the helical axis, the gradient operator matrix elements will be non-zero for direct transitions in the Brillouin zone, i.e., for transitions between electronic states *k* and *k'*, with the same value of κ. Polarizations transverse to the axis lead to

indirect transitions from an occupied state at κ in the Brillouin zone to an unoccupied state at $\kappa \pm \phi$, where ϕ is the twist angle.

2.7 Computational Methods Used

2.7.1 NRL/OSU POLYXA

The local-density band structure approach discussed herein was developed by Mintmire and colleagues originally to treat helical polymer systems.[31] The charge density (in the Coulomb potential) and the exchange-correlation potential are fit to linear combinations of Gaussian-type functions.[52, 54-57]

Fitting the charge density, $\rho(\mathbf{r})$, for use in the Coulomb interaction terms of the total energy expression was introduced for DFT calculations by Sambe and Felton as a means of reducing computational effort. Rather than using the bilinear expansion of the charge density, the approximate charge density, $\tilde{\rho}(\mathbf{r})$, is given by a linear combination of fitting functions, $\mathrm{F}_i(\mathbf{r})$,

$$\tilde{\rho}(\mathbf{r}) = \sum_i f_i \mathrm{F}_i(\mathbf{r}) . \qquad (2.40)$$

The POLYXA code implements this fitting approach for helical systems using an auxiliary basis set of s, p, and d type atom-centered Gaussian functions generated from the totally symmetry combination of local functions

$$\mathrm{F}_i(\mathbf{r}) = \sum_m S^m \, F_i(\mathbf{r}) . \qquad (2.41)$$

These functions are equivalent to Bloch functions with $\kappa=0$. Dunlap, et al. [54] and Mintmire [52] showed that methods developed for minimizing the error in the Coulomb error [58] could be used in molecular DFT-based calculations. These methods are based on minimizing the self-interaction of the error in the charge density, $\Delta\rho(r) = \rho(r) - \tilde{\rho}(r)$. The exact expression for the electron repulsion energy, $\mathrm{E_c}$, can be written

$$E_c = \frac{1}{2}[\rho \mid \rho] \\ = [\rho \mid \tilde{\rho}] - \frac{1}{2}[\rho \mid \rho] + \frac{1}{2}[\Delta\rho \mid \Delta\rho] \tag{2.42}$$

Minimization of the Coulomb self-interaction of the error density, $[\Delta\rho \mid \Delta\rho]$, leads to the condition for best fit,

$$[\rho - \tilde{\rho} \mid \mathrm{F}_i] = 0\,, \tag{2.43}$$

This condition leads to the corresponding matrix equations for solution of the above equation for molecular systems,

$$\sum_j [\mathrm{F_i} \mid \mathrm{F_j}] f_j = [\rho \mid \mathrm{F_j}]. \tag{2.44}$$

The Coulomb integrals given above are not well defined for periodic, extended systems and this scheme for molecular systems could not be extended directly to helical systems in the POLYXA code. Inclusion of Coulomb interactions involving the nuclei allowed the development of a mathematically well-defined algorithm. Defining the ratio, η_i of the total charge in a fitting function to the total nuclear charge in a unit cell,

$$\eta_i = \left\{ \int d^3r \; F_i(\mathbf{r}) \right\} / \sum_n Z_n\,, \tag{2.45}$$

the above condition for best fit can then be written

$$[\tilde{\rho} - \rho_N \mid \mathrm{F_i} - \eta_i \rho_N] - [\rho - \rho_N \mid \mathrm{F_i} - \eta_i \rho_N] = \eta_i [\rho_N \mid \tilde{\rho} - \rho]. \tag{2.46}$$

These equations are solved by treating the electrostatic interaction on the right-hand side as an undetermined multiplier, $\lambda = [\rho_N \mid \tilde{\rho} - \rho]$ and solve the matrix equations

$$\sum_j [\mathrm{F}_i - \eta_i \rho_N \mid \mathrm{F_j} - \eta_j \rho_N] f_j = [\mathrm{F}_i - \eta_i \rho_N \mid \rho - \rho_N] + \lambda \eta_i\,, \tag{2.47}$$

subject to the charge neutrality constraint,

$$\sum_i f_i \eta_i = 1 . \tag{2.48}$$

Formally the approximate Coulomb energy using the fitting functions includes the approximate electron-electron interaction but includes the exact electron-nuclear and nuclear-nuclear interactions using

$$\begin{aligned} E_{approx} &= [\rho - \rho_N \mid \widetilde{\rho} - \rho_N] - \frac{1}{2}[\widetilde{\rho} - \rho_N \mid \widetilde{\rho} - \rho_N] \\ &= [\rho \mid \widetilde{\rho}] - \frac{1}{2}[\widetilde{\rho} \mid \widetilde{\rho}] - [\rho \mid \rho_N] + \frac{1}{2}[\rho_N \mid \rho_N] \end{aligned} . \tag{2.49}$$

Analytic integrals cannot be directly calculated for the matrix elements of the exchange-correlation potential or exchange-correlation energy density. Rather than use numerical integration techniques to evaluate the matrix elements needed for the secular equation and the total energy evaluation, the POLYXA code uses a least-squares fitting technique to approximate the exchange-correlation potential (and exchange-correlation energy density) with a linear combination of periodic fitting functions, similar to the expansion used for fitting the charge density, using the form below

$$\widetilde{v}_{xc}(\mathbf{r}) = \sum_i g_i \mathrm{G}_i(\mathbf{r}) , \tag{2.50}$$

where

$$\mathrm{G}_i(\mathbf{r}) = \sum_m S^m G_i(r) . \tag{2.51}$$

The coefficients g_ℓ are chosen by minimizing the least-squares sum over a weighted set of points,

$$\sum_\ell w_\ell \left(v_{xc}(\mathbf{r}_\ell) - \sum_i g_i \mathrm{G}_i(\mathbf{r}) \right)^2 , \tag{2.52}$$

to yield the best-fit condition in algebraic form

$$\sum_j g_j \sum_\ell w_\ell G_i(\mathbf{r}_\ell) G_j(\mathbf{r}_\ell) = \sum_\ell w_\ell G_i(\mathbf{r}_\ell)\, v_{xc}(\mathbf{r}_\ell)\,. \qquad (2.53)$$

Dunlap and Cook [59] found that an optimum choice of weighting functions, w_ℓ, can be generated by multiplying the normal quadrature weights v_ℓ, appropriate for normal quadrature over space, with a factor proportional to the charge density divided by the exchange-correlation energy density. For LDA these quantities are related by:

$$w_\ell = v_\ell\, \rho^{2/3}(\mathbf{r}_\ell)\,. \qquad (2.54)$$

The numerical integration grid points, $\mathbf{r}_\ell$, and quadrature weights, v_ℓ, are chosen using techniques for smoothly combining nuclear-centered grids developed by Becke. [60]

2.7.2 CRYSTAL03

CRYSTAL03 [11] is utilized for comparison of results obtained using POLYXA. It performs *ab initio* calculations of the ground state energy, energy gradient, electronic wave function and properties of periodic systems using the LCAO approach. CRYSTAL03 has the capabilities of modeling structures in 0D, 1D, 2D, and 3D. Although crystal symmetry is taken into account by CRYSTAL03, only translational periodicity is implemented, thus limiting the variety of structures that we modeled. CRYSTAL03 operates within the framework of Hartree-Fock or Kohn-Sham and utilizes Gaussian basis sets. Although CRYSTAL03 uses different numerical grids and uses the full Coulomb interaction, it has similar fitting of the exchange potential used in POLYXA.

CHAPTER 3

HELICAL SILVER SINGLE-WALL NANOTUBES AND NANOWIRES

3.1 Introduction

As the miniaturization of electronic devices continues to advance, nanotubes and nanowires will become increasingly important in the development of these devices. A variety of procedures have been reported for constructing both gold and silver wires with nanoscale diameters.[12, 13, 61-68] Only one method has successfully produced gold nanowires exhibiting helical periodicity.[12, 13] This unique fabrication method reported by Takayanagi *et al.*, for constructing gold nanowires with diameters as small as 0.4 nm relies on the surface reconstruction properties present in gold.[12, 13, 69] The *in situ* fabrication method entails using high-resolution transmission electron microscopy (HRTEM) to irradiate a gold (001) film 3 to 5 nm in thickness until holes form, creating a bridge between two holes. As this bridge narrows to less than 1.5 nm in diameter, it reconstructs into a helical nanowire suspended between two bulk-like gold tips.

Rodrigues, *et al*.[64] implemented the above technique using silver. They successfully synthesized silver nanowires exhibiting a tube-like contrast pattern with an especially stable atomic structure. Although the silver wires were produced with diameters comparable to the gold nanowires reported by Takayanagi,[12, 13] the silver wires did not undergo a surface reconstruction leading to the helical structure, observed

for gold nanowires. However, a different fabrication method, one that does not rely directly upon surface reconstruction, may successfully yield silver nanowires exhibiting helical periodicity. For example, Hong *et al*.,[61] synthesized single-crystalline silver nanowires in an ambient solution phase. These silver nanowires, with 0.4 nm diameter, are comparable to the {4,2} silver nanowire (see the following section for notational description) discussed here with an energetic local minima. The structure of this silver nanowire is markedly different than bulk, and although not immediately apparent, this structure does exhibit helical periodicity.

Nevertheless, we are particularly interested in the helical multi-shell nanowires and a helical single-wall gold nanotube synthesized by Takayanagi *et al.*,[12, 13] which are favorable structures for our method of calculation based on the use of helical symmetry. As a starting point, we decided to model silver instead of more complex systems involving gold. Calculations for gold require treating relativistic effects, which is beyond the capability of our current first-principles approach. In this preliminary work, we will address similar trends in our results compared with theoretical work using gold and silver described elsewhere.[70-76]

The single-wall gold nanotube and the smallest multi-shell gold nanowire reported experimentally[12, 13] have been studied theoretically by others.[64, 71-73, 75] Calculations on several gold nanotube structures published elsewhere report results in terms of energy per unit length of wire, defined by the positive work done in drawing the wire out of the bulk-like gold tips, denoted as the string tension.[73, 74] Based upon first-principles calculations, Senger *et al.* studied a variety of possible structures for gold single-wall nanotubes.[73] In addition to the {5,3} gold nanotube fabricated

experimentally[13], they calculated six additional single-walled nanotubes as either tip-suspended or free-standing structures. The {5,5} tube was determined to be the most energetically favorable free-standing single-wall gold nanotube, and they predicted one other tube, the tip-suspended {4,3}, as another energetically favorable single-wall gold nanotube yet to be observed experimentally.[73] First-principles calculations by Yang *et al.*, showed that the {5,3} gold nanotube was capable of enduring large elongation without change in conductivity.[75] Perhaps the most interesting theoretical analysis is a recent first-principles study of the smallest helical multi-shell gold nanowire, a single-wall gold nanotube with an inserted chain, in which the authors conclude that helical gold nanowires are good candidates for nanometer-scale solenoids.[72]

The conductivity of the related gold nanowires[72, 73, 75] and very thin silver nanowires[70, 76] has been addressed in other theoretical studies. It is of interest due to the observation of quantized conductance in both gold and silver nanowires.[63, 64] Takayanagi *et al*., observed quantized conductance through individual rows of tip-suspended gold atoms.[63] The conductance was observed in units of $G_0 = 2e^2/h$, where *e* is the electron charge and *h* is Planck's constant. Consistent with this interpretation, the conductance is quantized such that it increases by a quantum conductance $2e^2/h$ whenever a band crosses the Fermi level.[77, 78] For an individual atomic chain only one conductance channel (i.e., $N_c = 1$) or band crosses the Fermi level. With each gold atomic chain contributing one channel of conductance, the quantized conductance for an *N*-channel system is expressed as $N_c G_0$.

The observation of quantum transport effects in nanowires requires structures with widths comparable to the Fermi wavelength (less than 1 nm for metals). [2] All of

the nanowire and nanotube structures within this study are certainly within this size requirement. Within the (n_1, n_2) notation scheme used herein, described in detail in Section 3.2.2, $n_1 + n_2 = N$ is equal to the number of helical strands comprising the tube. Because helical gold nanowires are essentially comprised of N-atom strands winding about the wire axis, the natural question to ask is whether quantized conductance is observed in steps of NG_0 in the helical nanotubes and nanowires. Other studies have found that the number of bands crossing the Fermi level, or the number of putative conduction channels, do not always correspond to the numbers of atom rows in the helical gold nanowires.[72-75] Similar studies have addressed the quantum transport mechanism present in silver nanowires.[70, 76]

Herein, we study the electronic structures of a variety of silver single-wall nanotubes and nanowires. We are particularly interested in the behavior of the total energies with respect to structural changes such as increasing nanotube radii. In addition, we studied the number of conduction channels associated with the calculated band structures of these systems. The methodology behind our approach and the geometrical models considered are the subject of the following section.

3.2 Computational Methods and Models

3.2.1 Theoretical Approach

We examined the electronic structures of extended silver single-wall nanotubes (AgSWNTs) within a first-principles, all-electron self-consistent LDF approach adapted for helical symmetry. A 3-21G basis set was used [79], along with 512 k points in the central Brillioun zone. The approach used here has been discussed in detail elsewhere.[14, 30, 31] All structures were calculated at or near equilibrium conformations. The specific tubes were chosen based on theoretical work published elsewhere for gold systems,[73, 75] as well as the single-wall gold nanotube fabricated in Ref. [13]. We carried out calculations on twenty-one different AgSWNTs ranging in radii from approximately 1.3 Å to 3.6 Å. AgSWNTs with radii greater than 2.2 Å were also calculated with a silver atomic chain inserted along the axis of the nanotube – these structures are termed silver nanowires (AgNWs).

3.2.2 Geometry and Notation of AgSWNTs

Modeling the silver nanotubes involves "rolling up" a triangular sheet of silver atoms and mapping the atoms onto the surface of a cylinder, comparable to rolling up a graphite sheet for a carbon nanotube. For the triangular sheet depicted in Fig. 1, each Bravais lattice vector, $\boldsymbol{R}$, is defined by two primitive lattice vectors $\boldsymbol{a}_1$ and $\boldsymbol{a}_2$ and the pair of integers (n_1, n_2), so that the lattice vector

$$\boldsymbol{R} = n_1\boldsymbol{a}_1 + n_2\boldsymbol{a}_2. \qquad (3.1)$$

Basis vectors are defined as

$$\boldsymbol{a}_1 = d\hat{i} \qquad (3.2a)$$

$$\boldsymbol{a}_2 = \frac{d}{2}\hat{i} + \frac{d\sqrt{3}}{2}\hat{j}\,, \qquad (3.2b)$$

where d is the Ag-Ag or Au-Au bond distance, and $\hat{i}$ and $\hat{j}$ are the unit vectors along the x and y directions. The radius for an (n_1, n_2) nanotube is given by

$$\rho = \frac{|\boldsymbol{R}|}{2\pi} = \frac{d}{2\pi}\sqrt{n_1^2 + n_2^2 + n_1 n_2}\,, \qquad (3.3)$$

where d is the Ag-Ag bond length from the triangular sheet. The notation chosen here with a 60° angle formed between the two basis vectors is related to the convention used for carbon nanotubes. As shown in Fig. 3-1, a line of symmetry extends through the triangular lattice for $n_1 = n_2$, and another line of symmetry is present for $n_2 = 0$. All possible AgSWNTs can be reduced by symmetry to an irreducible wedge formed between the two lines of symmetry. Analogous to carbon nanotubes, each $\boldsymbol{R}$ within this wedge defines a different AgSWNT, and all unique AgSWNTs defined by rolling up the triangular sheet of silver atoms can be generated by this set of $\boldsymbol{R}$'s.[32]

The twenty-one different nanotubes considered herein are labeled with a solid marker in Fig. 3-1. Structures to the left of the bold line were modeled as single-wall nanotubes only, as their radii are too small to contain an axial chain. Structures to the right of the bold line were modeled as single-wall tubes both with and without an inserted axial chain. The (3,2) nanotube and (4,3) nanotube and nanowire were treated in my M.S. report. [80] Herein, we study a much larger assortment of possible structures, using an improved basis set, and the orbital densities are plotted for the first time.

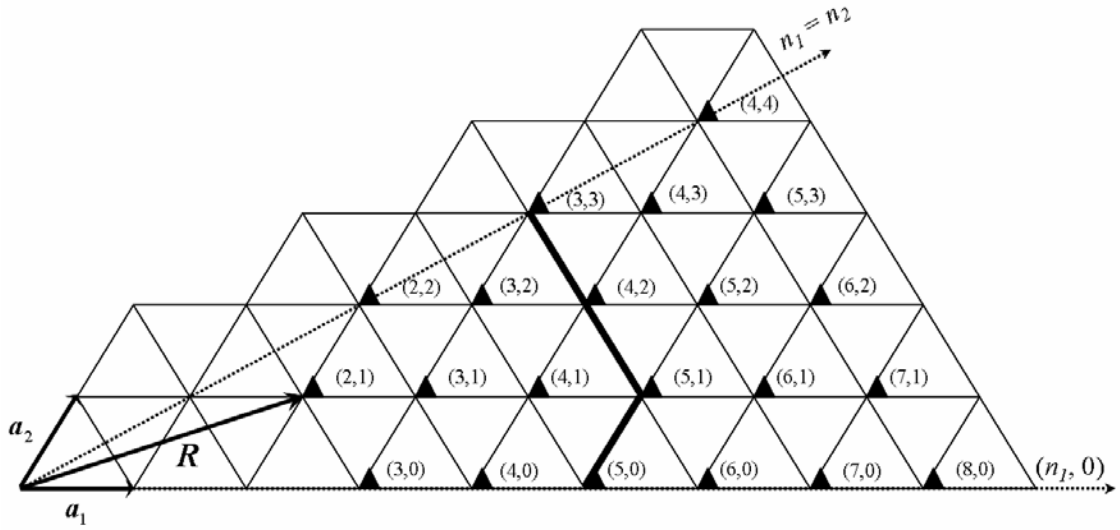

Figure 3-1. Triangular network of silver (or gold) atoms. Basis vectors are designated as $\boldsymbol{a}_1$ and $\boldsymbol{a}_2$. Each tube is labeled by two integers, (n_1, n_2), where the rollup vector is $\boldsymbol{R} = n_1\boldsymbol{a}_1 + n_2\boldsymbol{a}_2$. The dashed lines represent lines of symmetry; an irreducible wedge is formed between the two lines. AgSWNTs labeled with a solid marker correspond to the nanotubes that we consider in the present study. AgSWNTs located to the right of the bold line were also modeled with a silver atomic chain inserted along the axis of the nanotube. AgSWNTs containing an axial chain are designated as nanowires (AgNWs).

Models of selected AgSWNTs and a AgNW are given in Fig. 3-2. The (2,2) and (6,0) SWNTs are located along the lines of symmetry depicted in Fig. 3-1. Nanotubes with geometries lying between these lines of symmetry such as the (3,2) and (5,2) AgSWNTs are chiral.

The notation chosen scheme used throughout this dissertation is somewhat different than the notation used elsewhere which utilizes a 120° angle between basis vectors.[12, 13, 15, 16, 71, 73-75] Our decision to use this second notation scheme from previously published works[15, 16] was simply to be consistent with the works of others. For completeness we now discuss the differences between the two notation schemes and why we chose the notation scheme presented in Fig. 3-1 throughout this chapter. For comparison, we shall also provide a simple mechanism to convert from one notation to the other.

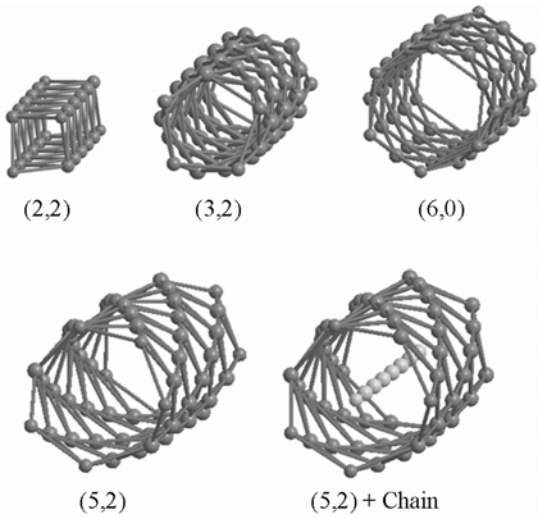

Figure 3-2. Models of selected AgSWNTs and the (5,2) AgNW (AgSWNT + inserted silver atomic chain).

Figure 3-3 illustrates the two different notational styles. Our notational style is indicated by parentheses, and the notational style adopted by others is indicated by curly brackets. Within the second notational style depicted in Fig. 3-3, each Bravais lattice vector, $\boldsymbol{R}$, is defined by two primitive lattice vectors $\boldsymbol{b_1}$ and $\boldsymbol{b_2}$ and the pair of integers $\{n_1', n_2'\}$, so that the lattice vector

$$\boldsymbol{R} = n_1'\boldsymbol{b_1} + n_2'\boldsymbol{b_2}. \tag{3.4}$$

Basis vectors are defined as:

$$\boldsymbol{b}_1 = d\hat{i} \tag{3.5a}$$

$$\boldsymbol{b}_2 = \frac{d}{2}\hat{i} - \frac{d\sqrt{3}}{2}\hat{j}, \tag{3.5b}$$

where d is the Ag-Ag or Au-Au bond distance, and $\hat{i}$ and $\hat{j}$ are the unit vectors.

The radius for an $\{n_1', n_2'\}$ nanotube is given by

$$\rho = \frac{|\boldsymbol{R}|}{2\pi} = \frac{d}{2\pi}\sqrt{n_1^2 + n_2^2 - n_1 n_2}, \tag{3.6}$$

where d is the Ag-Ag bond length from the triangular sheet, prior to rolling up the nanotube.

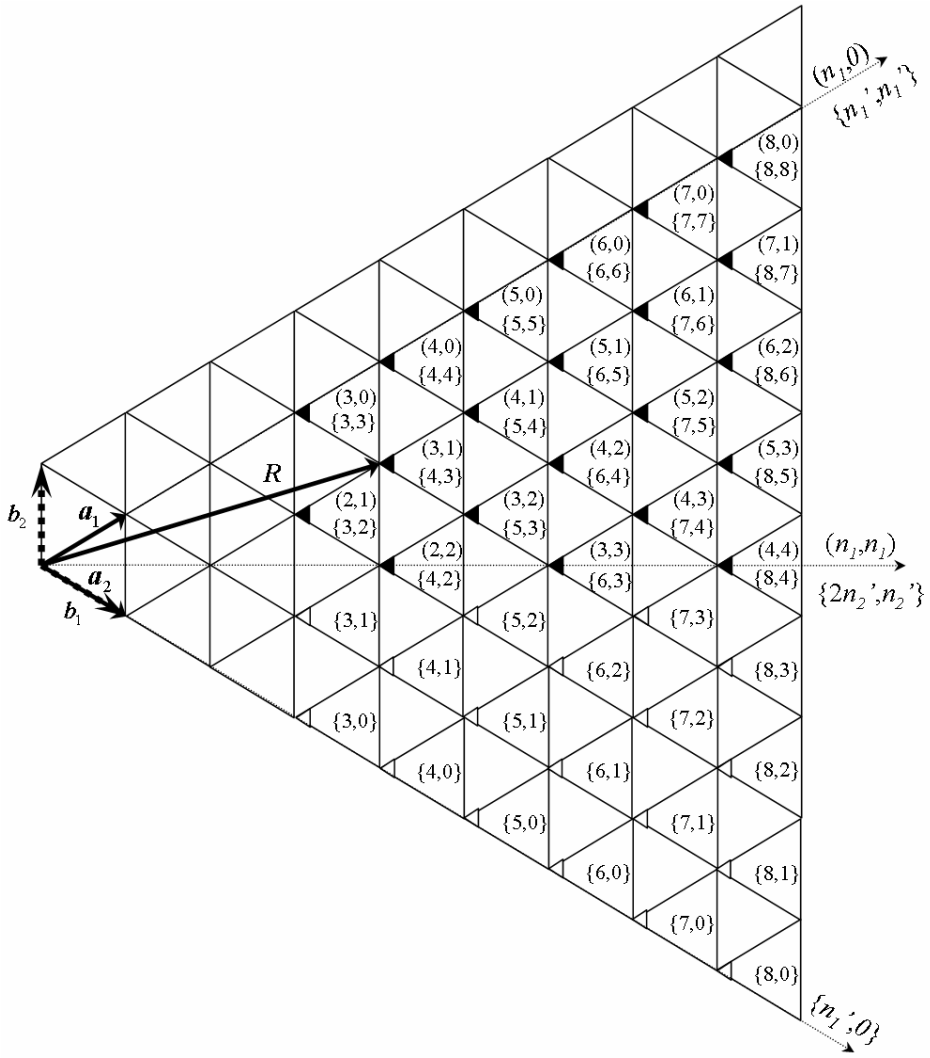

Figure 3-3. Triangular network of silver (or gold) atoms where two different notational styles are presented for comparison. Basis vectors for the preferred notational style are designated as $\boldsymbol{a}_1$ and $\boldsymbol{a}_2$ where the rollup vector is $\boldsymbol{R} = n_1\boldsymbol{a}_1 + n_2\boldsymbol{a}_2$. (Note: These basis vectors are interchanged without loss of generality with respect to Fig. 3-1.) Basis vectors corresponding to the second notational style are indicated as $\boldsymbol{b}_1$ and $\boldsymbol{b}_2$, and each nanotube is labeled by two integers $\{n_1', n_2'\}$ where the rollup vector is $\boldsymbol{R} = n_1'\boldsymbol{b}_1 + n_2'\boldsymbol{b}_2$. The dashed lines represent lines of symmetry.

Although both notation schemes are acceptable, we prefer the first notation method which utilizes a 60° angle between basis vectors because the numbering scheme is self contained. Within both notation schemes, each ***R*** within the wedge defines a different AgSWNT, and all unique AgSWNTs defined by rolling up the triangular sheet of silver atoms can be generated by that set of ***R***'s.[32] Within the first notation scheme which utilizes a 120° angle between basis vectors, the irreducible wedge is formed between two lines of symmetry: $n_1 = n_2$ and $n_2 = 0$. In other words, the first numbering method starts at (n_1, 0) and ends at (n_1, n_2) where $n_1 = n_2$. However, within the second notation scheme, the irreducible wedge is formed between two other lines of symmetry: $n_1 = n_2$ and $n_1 = 2n_2$. This means that the second numbering format starts at $\{2n_2', n_2'\}$, as opposed to $\{n_1', 0\}$, and ends at $\{n_1', n_2'\}$.

There are two problems associated with the second notational style which are best explained by example. Consider the nanotubes along the $n_1' = 2n_2'$ line of symmetry. Since the numbering scheme does not start at zero, this means that the {5,3} AgSWNT located on one side of the line of symmetry is also the {5,2} AgSWNT, located on the other side of the line of symmetry. The {7,4} is also the {7,3}, etc. Another confusing but important implication within the second numbering scheme is that the {7,7} and {7,0} would be the same nanotube! In other words, the second numbering scheme is not self-contained within the irreducible wedge.

To prevent any further confusion, we will follow the first notation scheme. If one finds it necessary to convert from one notation to the other, a simple algorithm follows. Letting the unprimed values in soft brackets represent our notation and the primed values

in curly brackets represent notation used by others, one can convert from one notation to the other through the following translation:

$$(n_1, n_2) \rightarrow (n_1 + n_2,\ n_1) \rightarrow \{n_1', n_2'\} \tag{3.7a}$$

$$\{n_1', n_2'\} \rightarrow \{n_2',\ n_1' - n_2'\} \rightarrow (n_1, n_2). \tag{3.7b}$$

For example, the (3,2) AgSWNT within our notation corresponds to the {5,3}AgSWNT within the second notation scheme. Within this study we will refer to all structures using our notation unless stated otherwise.

3.3 Method I: Conventional Helical Geometry and Unit Cell Sizes

3.3.1 Overview

We define the helical periodicity of the AgSWNTs in terms of a unit cell of a small number of silver atoms and a screw operation $S(h,\phi)$ that will generate the lattice of the nanotube nuclear coordinates. For mathematical convenience we define the screw operation in terms of a translation *h* units down the z axis in conjunction with a right-handed rotation ϕ about the z axis. Once we know (n_1,n_2) and the rollup vector $\boldsymbol{R} = n_1\boldsymbol{a}_1 + n_2\boldsymbol{a}_2$, as discussed in the previous section, the procedure for determining the necessary parameters is straightforward. The appropriate unit cell size, *N*, for generating the AgSWNT is simply the greatest common factor of the nanotube indices.

$$N = GCF(n_1, n_2) \tag{3.8}$$

Hence, for the (3,2) AgSWNT, only one silver atom comprises the unit cell. By repeatedly applying the screw operation to that one silver atom, we generate the entire (3,2) AgSWNT. For the (2,2) AgSWNT, there are two silver atoms in the unit cell, and for the (6,0) AgSWNT six silver atoms are contained within the unit cell. The unit cell sizes associated with the use of helical periodicity are typically much smaller than those associated with using the more traditional translational periodicity.

The procedure for determining *h* and ϕ is as follows. First, we find the appropriate $\boldsymbol{H}$ in terms of m_1 and m_2 that satisfies:

$$(n_1 m_2) - (n_2 m_1) = \pm N \tag{3.9}$$

$$\boldsymbol{H} = m_1\boldsymbol{a}_1 + m\boldsymbol{a}_2 \tag{3.10}$$

Once we have determined $\boldsymbol{H}$, it is straightforward to calculate *h* and ϕ:

$$h = \frac{\left|\boldsymbol{H} \times \boldsymbol{R}\right|}{\left|\boldsymbol{R}\right|} \tag{3.11}$$

$$\phi = 2\pi \frac{\boldsymbol{H} \cdot \boldsymbol{R}}{\left|\boldsymbol{R}\right|^2} \tag{3.12}$$

Establishing the geometry and unit cell sizes for the AgNWs (AgSWNTs with an inserted chain) is less straightforward. A super-cell was used to match the helical periodicity and translational spacing of the chain with the AgSWNT. The bond lengths of the inserted chains range from 2.43 Å to 2.88 Å and were chosen in order to match the periodicity of the respective nanotube. The atomic chain with the lowest total energy in this study had a bond length of 2.61 Å, which is comparable to the 2.64 Å optimized bond length recently reported by Agrawal et al.[70]

The approach for determining the unit cell size for the nanowires is best explained by way of example. Consider the (5,2) AgSWNT with an inserted chain. The following parameters define the (5,2) AgSWNT: h = 0.39106 Å, ϕ = 2.6583, and ρ = 2.8029 Å. To determine how many silver atoms are needed to generate the nanotube component of the super-cell, we first determine how many silver atoms are needed to match the translational periodicity of the chain with the nanotube. We know that h = 0.3911 Å in this case for the AgSWNT, but we want *h'*, the translational parameter of the super-cell, to be approximately 2.6 Å. Thus, if N_{tube} represents the number of atoms corresponding to the nanotube in the super-cell, we evaluate: $N_{tube} \cdot h = h' \approx 2.6$. The closest match in this case is N_{tube} = 7, resulting in *h'* = 2.7374 Å. One additional silver atom is used for the inserted chain, resulting in a total of 8 silver atoms for the super-cell of the (5,2) AgNW. The twist angle of the supercell ϕ' is determined by:

$$\phi' = (N_{tube}\phi) \bmod 2\pi \qquad (3.13)$$

Therefore, in this example, ϕ'=6.0415.

In almost all cases the chain was placed precisely at the origin, but in some cases it proved energetically favorable to displace the chain slightly along the z – axis, relative to the exterior AgSWNT. For example, the (5,0) AgSWNT shown in Fig. 3-4 with a radius of 1.4801 Å is the smallest nanotube considered in this study with an inserted axial chain. The nanotube radius corresponds to a bond length much too short to be energetically favorable or even plausible. By staggering the chain along the z – axis, the nearest neighbor bond length between atoms in the chain and atoms in the nanotube increases to approximately 2.5 Å.

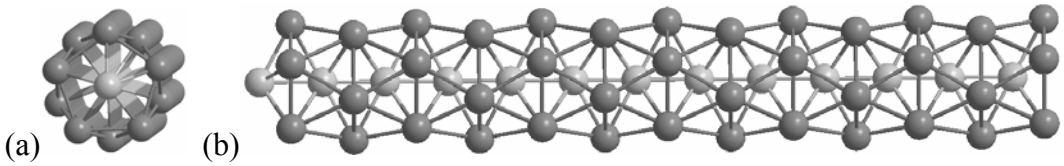

Figure 3-4. Model of the (5,0) AgNW (a) looking down the axis of the nanotube and (b) along the side.

3.3.2 Energetic Results

The optimized total energies for the AgSWNTs and AgNWs are given with respect to radius in Table I and are plotted in Fig. 3-5. As a result of our calculations, we find local minima in total energy to exist for the (2,2), (3,2), (3,3), (4,3), (5,2), (5,3), and (7,1) AgSWNTs. Upon inserting the chain into the (5,2) nanotube, this structure becomes the most energetically favorable AgNW, with the (6,0) and (4,3) AgNWs following within 10^{-4} eV. We find the (2,1) and (3,0) to be the highest in total energy, and therefore the least favorable structures within this study.

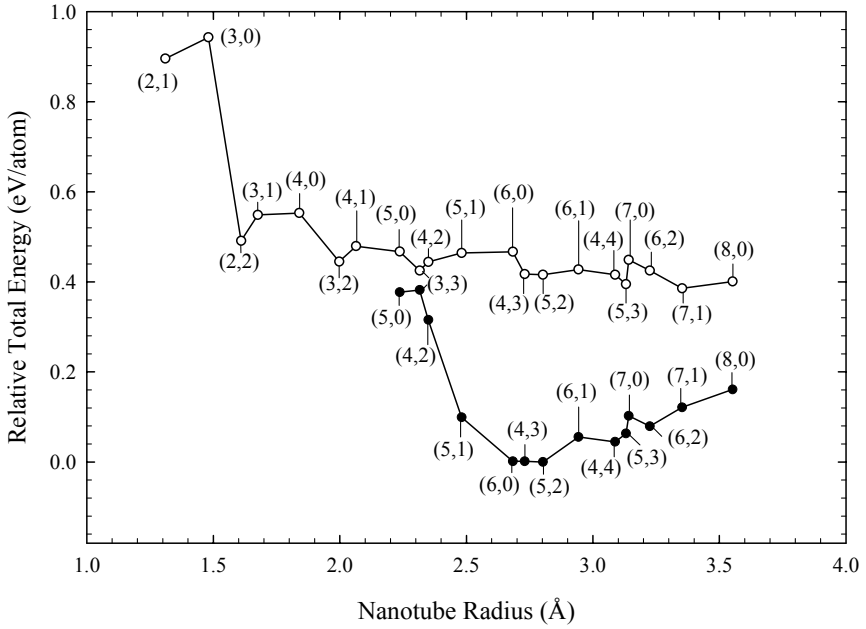

Figure 3-5. Total energy per silver atom versus nanotube radius. Open circles represent AgSWNTs and closed circles represent AgNWs. The (5,2) AgNW has the lowest energy and is centered about zero; the energies of all other tubes are plotted with respect to zero. Local minima in total energy are shown for the (2,2), (3,2), (3,3), (4,3), (5,2), (5,3) and (7,1) AgSWNTs. [16]

		AgSWNT		AgNW *(AgSWNT + Center Chain)*	
Structure	Radius (Å)	N_{Ag}	eV/N_{Ag}	N_{Ag}	eV/N_{Ag}
(2,1)	1.3096	1	0.8956	-	-
(3,0)	1.4801	3	0.9430	-	-
(2,2)	1.6099	2	0.4911	-	-
(3,1)	1.6756	1	0.5488	-	-
(4,0)	1.8398	4	0.5528	-	-
(3,2)	1.9972	1	0.4448	-	-
(4,1)	2.0640	1	0.4794	-	-
(5,0)	2.2361	5	0.4671	6	0.3772
(3,3)	2.3156	3	0.4251	7	0.3817
(4,2)	2.3497	2	0.4443	7	0.3156
(5,1)	2.4812	1	0.4640	7	0.0994
(6,0)	2.6834	6	0.4668	7	***0.0014***
(4,3)	2.7300	1	0.4173	8	***0.0015***
(5,2)	2.8029	1	0.4158	8	***0.0000***
(6,1)	2.9431	1	0.4272	8	0.0554
(4,4)	3.0874	4	0.4158	9	0.0446
(5,3)	3.1306	1	0.3945	9	0.0634
(7,0)	3.1417	7	0.4491	8	0.1022
(6,2)	3.2250	2	0.4250	9	0.0795
(7,1)	3.3524	1	***0.3857***	10	0.1212
(8,0)	3.5523	8	0.4006	9	0.1610

Table I. Total energies relative to the (5,2) AgNW. The structures are listed by increasing radii, and N_{Ag} represents the number of silver atoms per unit cell. Super cells were used for the AgNWs to match the periodicity of the chains with their respective AgSWNTs. Shown in bold italics, the (6,0), (4,3), and (5,2) are the most energetically favorable AgNWs, while the (7,1) is the most energetically favorable AgSWNT.

Energetic trends for the AgSWNTs with respect to nanotube radius differ from what we would expect; the total energy does not necessarily decrease monotonically as radius increases. In some cases, between local minima, the total energy per silver atom increases as nanotube radius increases. Elastic strain models, such as those used for carbon SWNTs, would predict that the total strain energy should increase as the radius decreases. The strain energy per carbon atom in carbon nanotubes relative to an unstrained graphite sheet scales as $1/R^2$ (where R is the tube's radius).[35] A smooth $1/R^2$ trend is not present within our results for the AgSWNTs. If we group the AgSWNTs by their geometries, the total energy versus radius curve becomes smoother, but we see a trend where the calculated energy initially falls off at a rate faster than $1/R^2$. We grouped the applicable (n_1,n_2) AgSWNTs as belonging to either the (n_1, 0) group (i.e. the (5,0) AgSWNT) or the (n_1 ,1) group (i.e. the (4,1) AgSWNT). The plots for the (n_1, 0) and (n_1 ,1) groups are given in Figs. 3-6 and 3-7 respectively. Although there are two additional groups present, the (n_1 , 2) and the (n_1 , 3) group, these later two groups do not contain AgSWNTs with small enough diameters to see the trend – their curves are essentially flat.

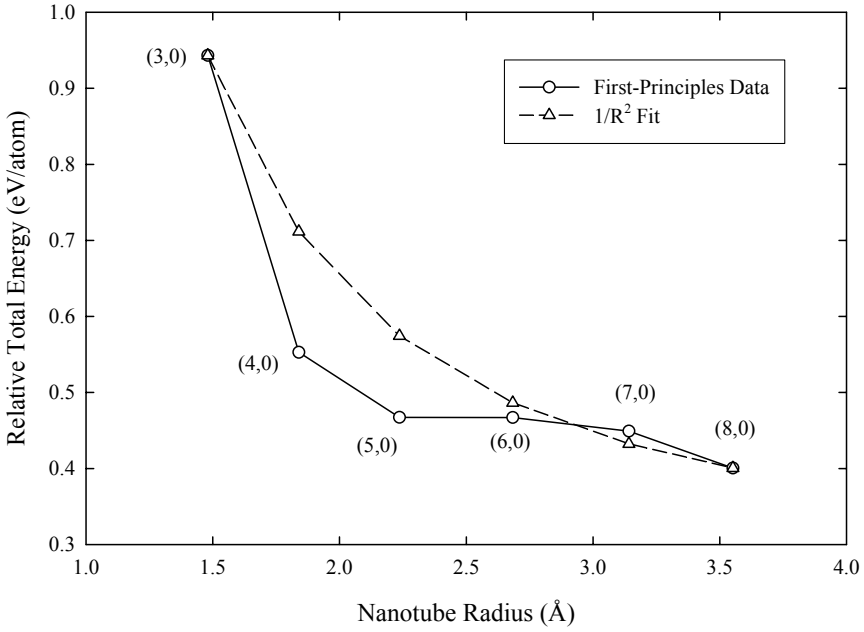

Figure 3-6. Total energy per silver atom versus nanotube radius for all (n_1, 0) AgSWNTs. The solid line represents calculated values, while the dashed line represents a $1/R^2$ fit. In each case, the calculated values fall off at a rate faster than $1/R^2$. Calculated values are given in Table 1. [16]

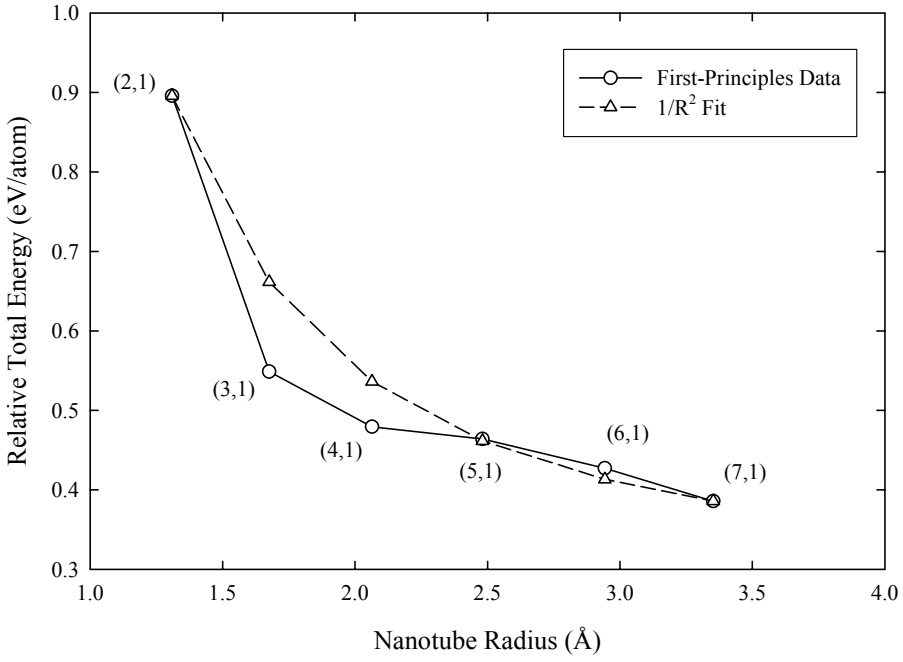

Figure 3-7. Total energy per silver atom versus nanotube radius for all (n_1,1) type AgSWNTs. The solid line represents calculated values, while the dashed line represents a $1/R^2$ fit. In each case, the calculated values fall off at a rate faster than $1/R^2$. Calculated values are given in Table 1. [16]

3.3.3 Band Structures, Densities of States, and Conduction Channels

The band structures and densities of states for the (7,1) and (3,2) AgSWNTs are shown in Figs. 3-8 and 3-9. The (7,1) AgSWNT has the lowest total energy of all AgSWNTs. The (3,2) AgSWNT is of interest because it has the same structure as the helical gold single-wall nanotube reported by Takayanagi et al. [13] That is, it structurally corresponds to the only single-wall gold nanotube ever observed experimentally. Again, for the (n_1, n_2) notation scheme chosen here, $n_1 + n_2$ is equal to the number of helical strands comprising the tube. The (7,1) AgSWNT comprised of eight strands has seven Fermi crossings, while the (3,2) AgSNWT with five strands has five Fermi crossings. Lower-lying flatter bands observed in the band structures correspond to *d*-orbitals. Because the density of states is inversely proportional to the slope of the energy versus $\boldsymbol{k}$ curve, the densities of states are much greater for these lower-lying bands.

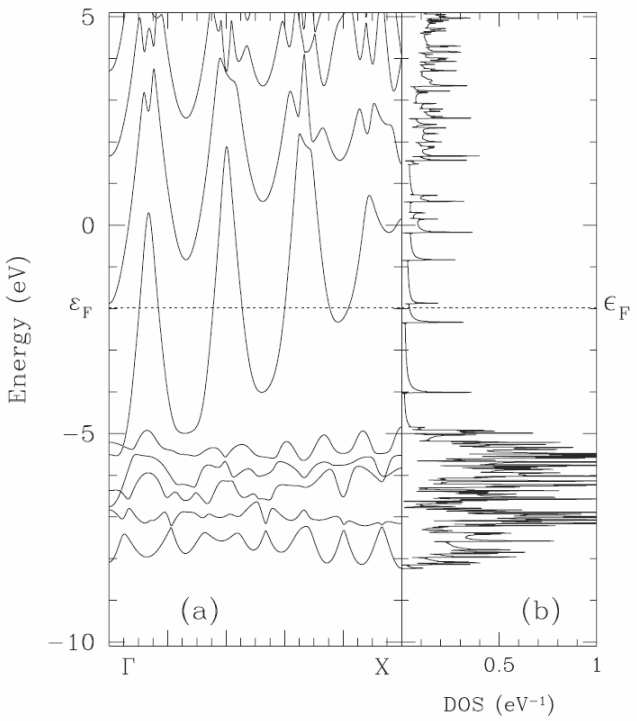

Figure 3-8. (a) Band structure and (b) density of states for the (7,1) AgSWNT. The Fermi level is indicated at -1.9795 eV.

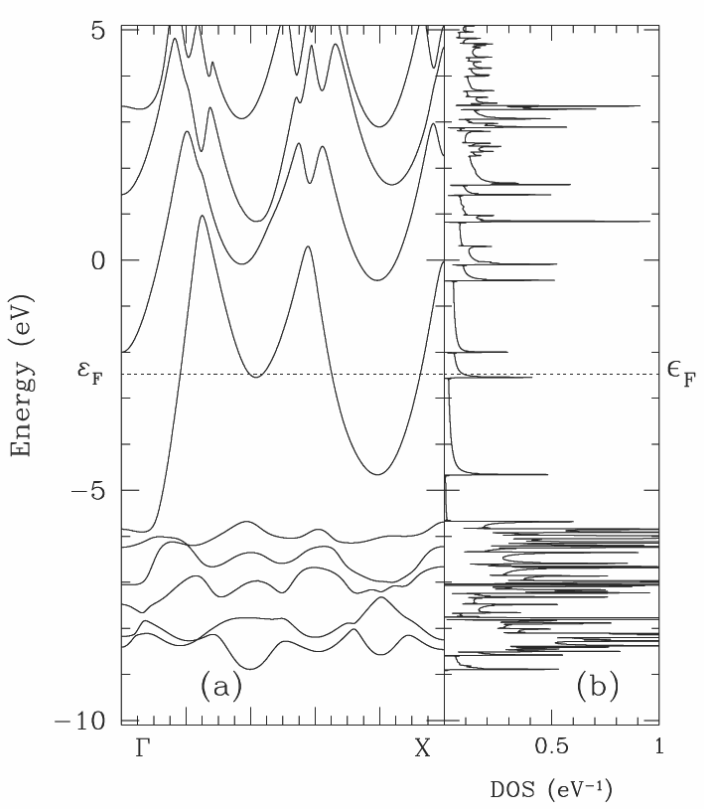

Figure 3-9. (a) Band structure and (b) density of states for the (3,2) AgSWNT. The Fermi level is indicated at -2.4342 eV.

The band structures comprising the (4,3) AgNW is shown in Fig. 1.11. The (4,3) AgNW corresponds to the smallest helical gold nanowire observed experimentally.[12]

Although the number of conduction channels in a AgSWNT does not always correspond to the number of atom rows, inserting an atomic chain along the nanotube axis always contributes one additional conduction channel. The band structures from our calculations are shown in Fig. 1.10 for the (3,2) AgSWNT. The band structure is depicted within a zone folding scheme to better illustrate the number of bands crossing the Fermi level. The points correspond to locations where the bands cross the Fermi

level, and they correspond to the orbital density figures generated in Fig. 1.12. This nanotube with $n_1 + n_2 = 5$ exhibits five conduction channels.

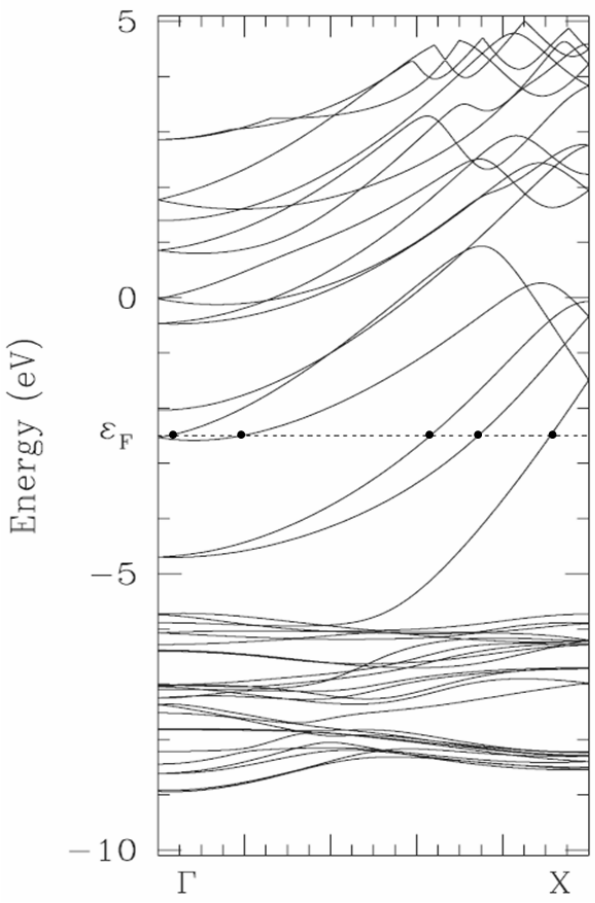

Figure 3-10. Band structure for the (3,2) AgSWNT shown within a zone-folding scheme. Points correspond to the orbital density images shown in Figure 12.

Band structures for the (4,3) AgSWNT, the silver atomic chain, and the (4,3) with the inserted chain are shown in Fig. 3-11. The (4,3) AgNW corresponds to the smallest multishell gold nanowire found experimentally[12] and has recently been suggested as a possible nano-solenoid.[72] The inserted atomic chain contributes one conduction channel, while the (4,3) tube without an inserted chain with $n_1 + n_2 = 7$, contributes five

conduction channels. The composite structure with $n_1 + n_2 = 8$, has six conduction channels. These results agree with results for the number of conduction channels from first-principles calculations on the 7-1 helical gold nanowires.[72, 74] The band crossing the Fermi level associated with the chain, shown in bold in Fig. 3-11(b), is shifted higher in energy into the conduction band upon being placed inside the AgSWNT, as shown in Fig. 3-11(c). The band that lies just above the Fermi level in the AgSWNT shown in Fig. 3-11(a) dips below the Fermi level upon inserting the chain, as shown in Fig. 3-11(c). Inserting the chain lowers the energies of the bands from the AgSWNT with respect to the Fermi level, resulting in one additional conduction channel.

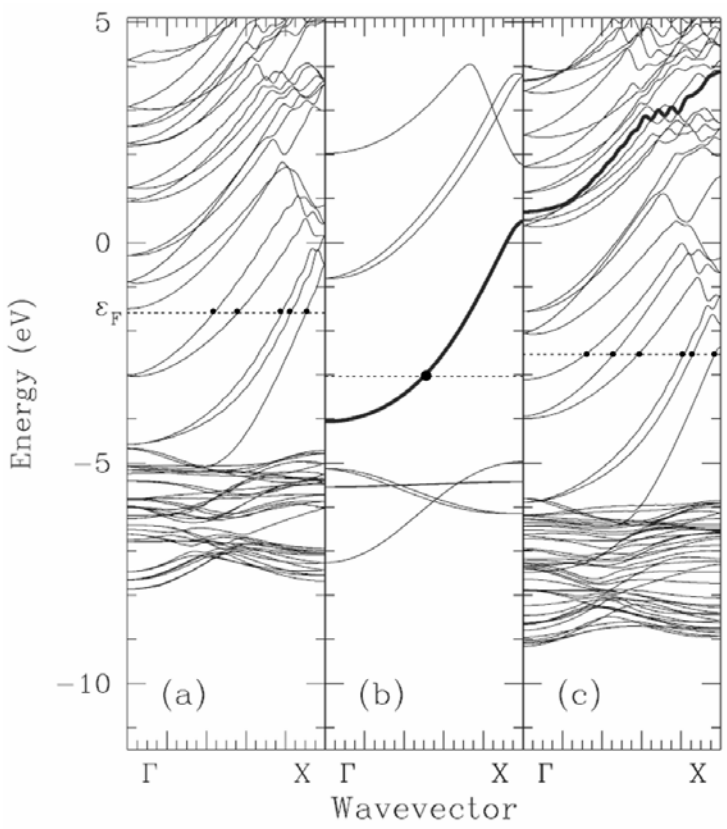

Figure 3-11. Band structures for the (a) (4,3) AgSWNT, (b) silver atomic chain, and (c) the (7,4) AgNW. Fermi levels are shown with a dashed line. Points correspond to the orbital density images shown in Figure 6. The band crossing the Fermi level in (b), shown in bold, is shifted higher in energy into the conduction band in (c). The band that lies just above the Fermi level in the AgSWNT shown in (a) dips below the Fermi level upon inserting the chain, as shown in (c). The number of Fermi crossings corresponds to the number of conduction channels in a particular structure. There are five Fermi crossings in (a), one Fermi crossing in (b), and six Fermi crossings in (c). [16]

3.3.4 Orbital Densities

The orbital densities for the (3,2) AgSWNT are shown in Fig. 3-12, and orbital densities for the (4,3) AgSWNT, the inserted silver atomic chain, and (4,3) AgNW are shown in Fig. 3-13. The images correspond to bands at specific points within the Brillioun zone, depicted in Figs. 3-10 and 3-11 by points located from left to right respectively. Upon close inspection of the band structures, we note that the band crossing the Fermi level in Fig. 3-11(b), from the chain alone does not correspond directly to the extra band crossing the Fermi level in Fig. 3-11(c). Rather, the band lying just above the Fermi level in the AgSWNT shown in Fig. 3-11(a) dips below the Fermi level upon inserting the chain, as shown in Fig. 3-11(c). Inserting the chain lowers the energies of the bands from the AgSWNT with respect to the Fermi level, resulting in one additional conduction channel. The bands mix and introduce substantial chain character into multiple bands near the Fermi level. The band crossing the Fermi level in Fig. 3-11(b) does not simply disappear – it is shifted higher in energy into the conduction band. This behavior upon inserting the chain consistently results in an extra conduction channel for all AgNWs considered in this study.

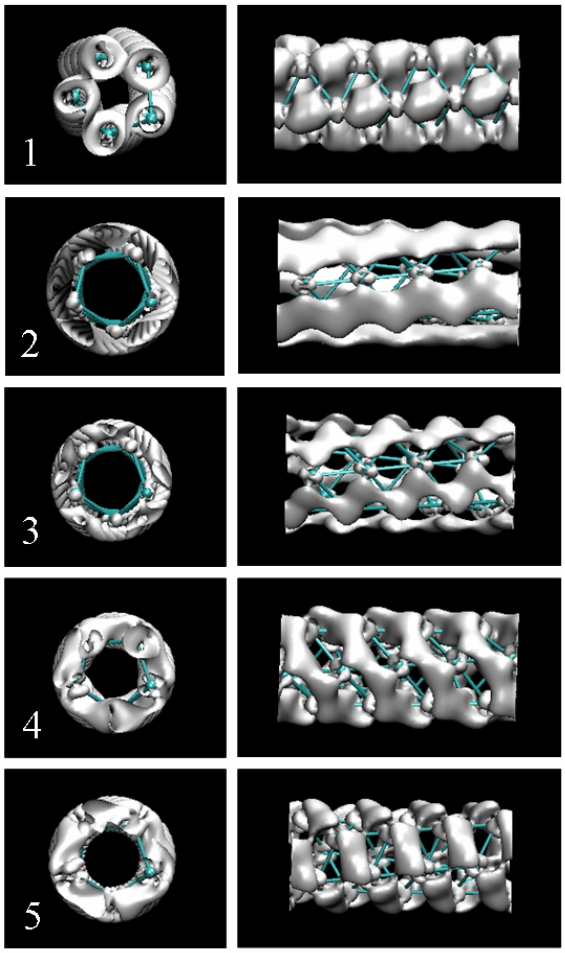

Figure 3-12. Orbital densities for the (3,2) AgSWNT. The images correspond to bands at specific points within the Brillioun zone, as indicated in Figure 10 by points. The numbering scheme from 1 to 5 corresponds to the solid points located from left to right respectively.

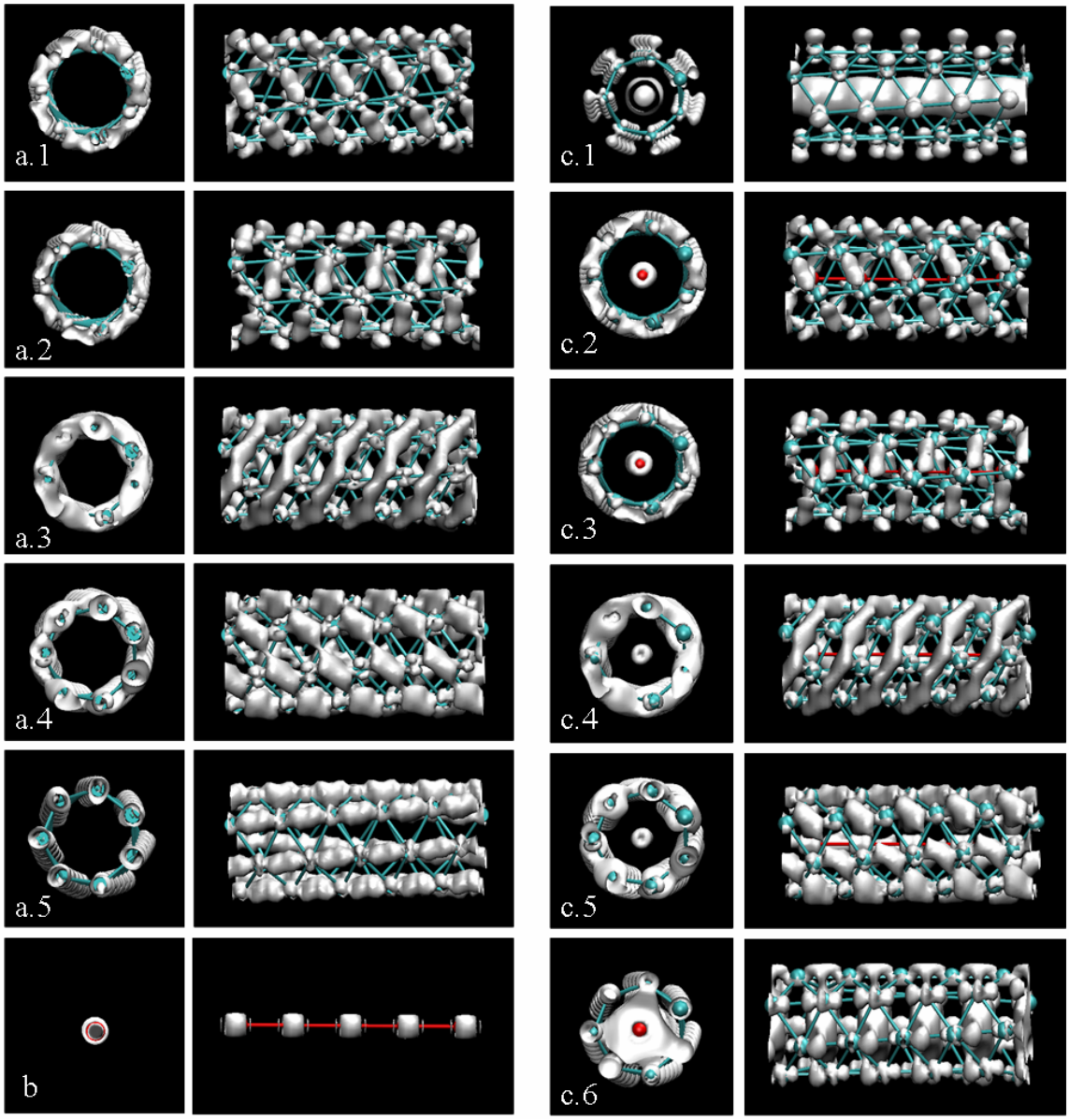

Figure 3-13. Orbital densities for the (a) (7,4) AgSWNT, (b) silver atomic chain, and (c) (7,4) AgNW. The structure of the inserted chain (c) is shown in red to aid in visualization. The images correspond to bands at specific points within the Brillioun zone, as indicated in Figure 11 by solid dots. The numbering scheme from 1 to 6 corresponds to the solid dots located from left to right respectively. [16]

3.3.5 Summary and Conclusions

The calculated energetic results were not as expected. The total energies for the AgSWNTs do not decrease monotonically as radius increases. We find a series of local minima to exist for the AgSWNTs, with the (7,1) AgSWNT having the lowest energy among the hollow nanotubes. Upon inserting the chain into the nanotubes, the (5,2), (6,0) and (4,3) AgNWs have the lowest total energies. We observe the following for all AgSWNTs considered here: three conduction channels are present if $n_1 + n_2 = 3$ or 4, five conduction channels are present if $n_1 + n_2 = 5$, 6, or 7, and seven conduction channels are present if $n_1 + n_2 = 8$. In agreement with Senger *et al*.,[73] our band structure calculations for the (3,2), (4,1) and (5,0) AgSWNTs, with $n_1 + n_2 = 5$ silver atom strands, all have densities of states corresponding to five conduction channels. In agreement with other theoretical work the structure corresponding to the (4,2) AgSWNT with $n_1 + n_2 = 4$ helical strands exhibits three conductance channels.[72, 76]

3.4 Method II: Strand by Strand – A Complementary Approach to Conventional Helical Geometry

3.4.1 Overview

Within the (n_1,n_2) notation scheme chosen here, $n_1 + n_2$ is equal to the number of helical strands comprising the tube. In this approach we calculate the band structures of these AgSWNTs by "building" these structures strand by strand. This section explains how the number of silver atoms per unit cell is determined when modeling these structures strand by strand. Although this approach may be used for all types of AgSWNT within this study, we choose to focus on the $(n_1, 0)$ – type AgSWNTs and AgNWs. Figure 1.14(a-f) illustrates this concept for a (6,0) AgSWNT, and Figure 3-14 (g) shows the insertion of the atomic chain along the axis of the nanotube.

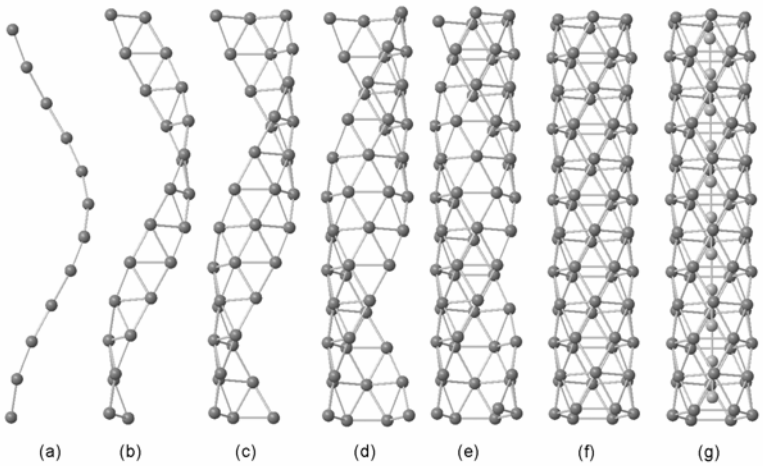

Figure 3-14. (a-f) The (6,0) AgSWNT assembled strand by strand. (g) The (6,0) AgSWNT with an inserted silver chain along the axis of the nanotube. The nanotube is tilted at a slight angle to aid in visualization. [15]

As explained in Section 3.3.1, supercells were used for the AgNWs to match the helical periodicity and translational spacing of the chain with the AgSWNT. We also recall that the unit cell size, N, for a AgSWNT is simply the greatest common factor of the nanotube indices. Therefore, for all $(n_1,0)$ – type AgSWNTs, $N = n_1$. In other words, by repeatedly applying the screw operation to all N atoms in the unit cell, the entire AgSWNT is generated. This also means that repeatedly applying the screw operation to only 1 atom in the unit cell generates only $1/N^{th}$ of the AgSWNT. Therefore, the nanotube can be built by adding one atom at a time to the unit cell until the entire tube is generated. Specifically, the number of silver atoms in a unit cell is equal to the number of strands desired. Lastly, for the $(n_1, 0)$ – type systems, the translational periodicity h conveniently corresponds to the approximate bond length desired for the inserted chain.

We are interested in the correlation between the total energies and the number of strands within a given system as the structures is built strand by strand. We are also concerned with how the number of available conduction channels change upon successive addition of each strand. Through using this approach, we shall see the properties of these systems change as the nanotubes and nanowires are being built.

3.4.2 Energetic Results

Numerical values for the total energies per number of strands are given in Table II, and the total energy versus the number of strands is shown in Fig. 3-15. The (6,0) AgSWNT with the inserted chain has the lowest total energy, therefore it is set to zero and all other energies are plotted with respect to zero. With the addition of each strand, from 1 to $n-1$, the total energy falls off inversely proportional to the number of strands.

Upon adding the n^{th} chain, there is an abrupt lowering of the total energy, and the energy drops even further upon inserting the axial chain into the (6,0), (7,0), and (8,0) AgSWNTs.

Structure / N_{Ag}	eV/N_{Ag}								
	1	*2*	*3*	*4*	*5*	*6*	*7*	*8*	*9*
(4,0)	2.0762	1.2381	0.8789	*0.4980*	-----	----	----	----	----
(5,0)	2.0191	1.1647	0.8408	0.6939	*0.4109*	----	----	----	----
(6,0)	2.0230	1.1540	0.8300	0.7211	0.6531	*0.4112*	***0.0000***	----	----
(7,0)	2.0463	1.1538	0.8164	0.7129	0.6422	0.5733	*0.3946*	***0.0463***	----
(8,0)	2.0273	1.1266	0.8000	0.6912	0.6286	0.5796	0.5225	*0.3456*	***0.1116***

Table II. Total energies given by strand count relative to the (6,0) AgNW. The energies associated with the completed AgSWNTs are italicized, and the energies associated with the completed AgNWs are given in bold italics.

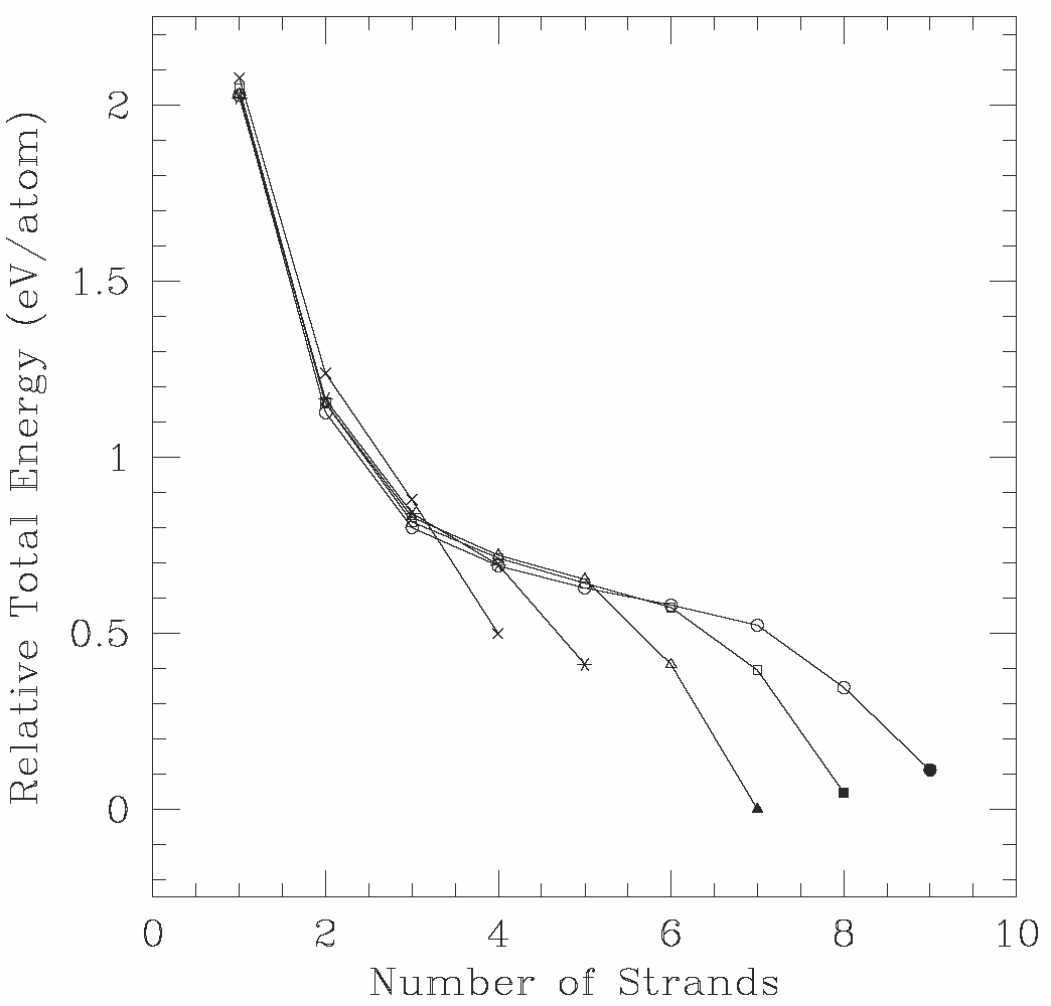

Figure 3-15. Total energy versus the number of strands for $n_1 = n_2$ type structures. x's represent the (4,0) AgSWNT, *'s represent the (5,0) AgSWNT, Δ's represent the (6,0) AgSWNT, □'s represent the (7,0) AgSWNT, and ○'s represent the (8,8) AgSWNT. Solid markers, ▲, ■, and ●, represent the (6,0), (7,0), and (8,0) AgSWNTs with inserted chains along their axis. [15]

3.4.3 Band Structures, Densities of States, and Conduction Channels

For each individual configuration shown in Fig. 3-15, the corresponding band structure is given in Fig. 3-16. While the structures with one or two strands supply one or two channels of conductance, respectively, this trend begins to decline with the addition of the third strand. Upon adding the sixth strand, thus completing the (6,0) AgSWNT, there are only five channels of conductance present. The addition of the seventh strand along the axis of the nanotube results in one additional conduction channel; there are now six channels of conductance available for the seven-stranded composite system. We note that the Fermi level generally rises with the addition of more strands, while decreasing upon inserting the axial chain. Furthermore, inserting the chain lowers the energies of the bands from the AgSWNT with respect to the Fermi level resulting in one additional conduction channel**.** The band lying just above the Fermi level in the AgSWNT indicated dips below the Fermi level upon inserting the chain, as shown in Fig. 3-16(g).

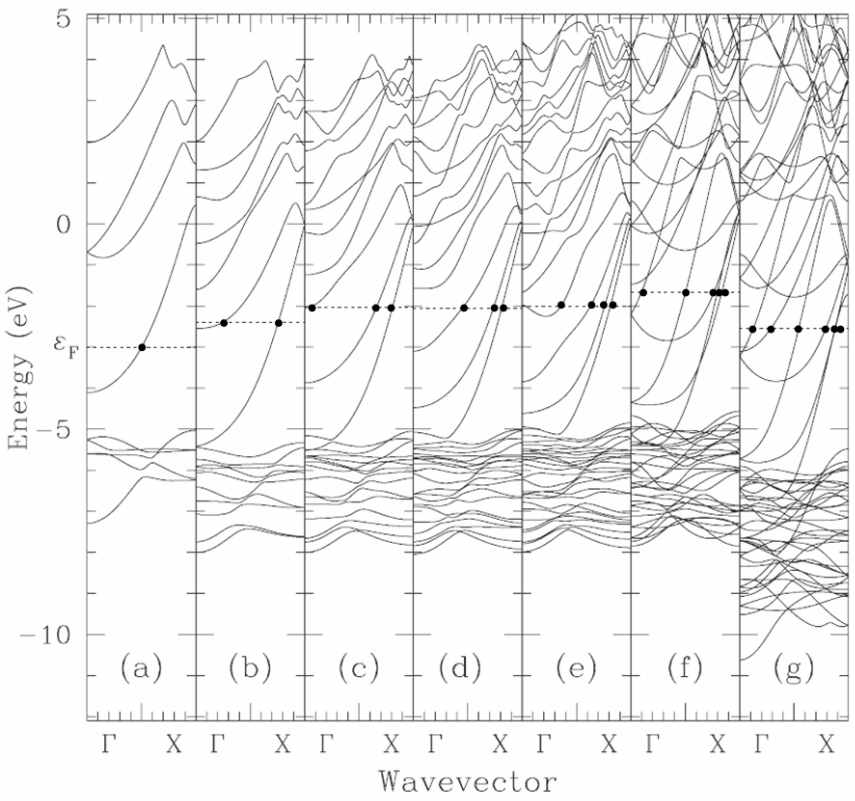

Figure 3-16. (a-f) Band structures for the (6,0) AgSWNT, assembled strand by strand, corresponding to the respective structures in Figure 3-15. (g) Band structure for the (6,0) AgSWNT with the inserted silver chain along the axis of the nanotube.

3.4.4 Orbital Densities

The orbital densities corresponding to locations where the bands cross the Fermi level in the (6,0) AgSWNT and AgNW are shown in Fig. 3-17. Labels (a – g) denote orbital densities corresponding to Fig. 3-16. The numbering scheme corresponds to the points in Fig. 3-16., from left to right respectively. The inset shows a close-up view of the orbital density corresponding to the extra band crossing the Fermi level upon inserting the axial atomic chain.

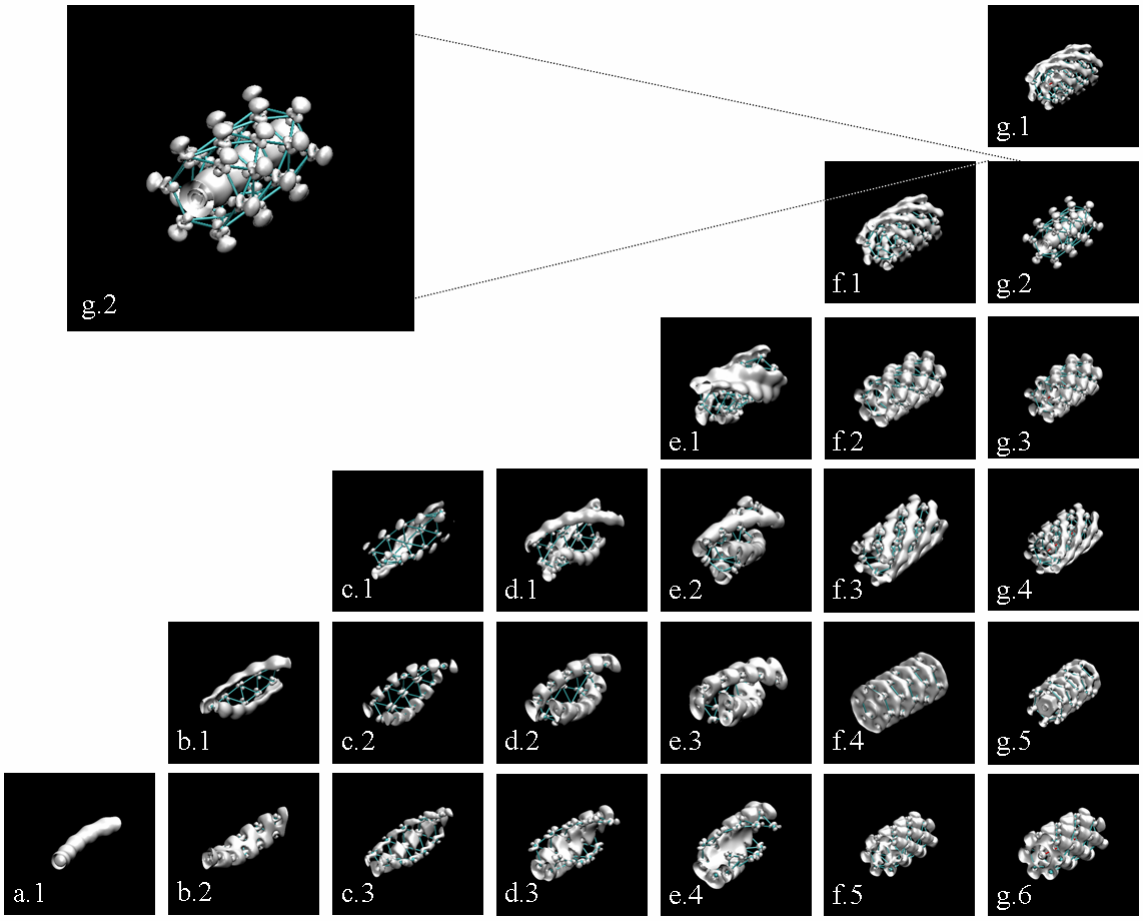

Figure 3-17. Orbital densities for the (6,0) AgSWNT and AgNW as the system is built starting with one strand and consecutively adding one additional strand until the structure is complete.

3.4.5 Summary and Conclusions

With the addition of each strand, the total energy falls off inversely proportional to the number of strands. Upon adding the final strand and thus completing the nanotube structure, there is an abrupt lowering of the total energy. The total energies are the lowest for the nanotubes containing an axial chain. The number of conduction channels does not always correspond to the number of atomic strands comprising the structure. By calculating the band structures for the AgSWNTs considered here, we observe the following: the (4,0) AgSWNT has three conduction channels, the (5,0), (6,0), and (7,0) AgSWNTs have five conduction channels, and the (8,0) AgSWNT has seven conduction channels. The addition of the central chain to the (6,0), (7,0), and (8,0) AgSWNTs contributes one additional channel of conductance. We also note that the Fermi level rises with the addition of each strand, while decreasing upon inserting the axial chain.

3.5 Perspectives and Future Work

Relativistic effects are most likely responsible for the experimentally observed differences in gold and silver. Rodrigues et al., [8] implemented the same approach for making helical gold nanowires reported by Takayanagi et al., [2,3] using silver. They successfully made silver nanowires, but the silver wires did not undergo the surface reconstruction phase which leads to the helical structures observed for gold nanowires.

Studies by Takeuchi et al. cite relativistic effects as the underlying reason behind surface reconstruction differences in gold and silver. For example, the ideal un-reconstructed (100) surface of Au should be a square lattice, but experiments indicate that the ground state of this surface corresponds to a contracted hexagonal-close-packed overlayer on top of a square substrate. The differences in both bulk and surface properties of gold and silver originate from relativistic effects which lower the position of the *s*-like electrons relative to the *d* bands. Herein, we are primarily interested in the reconstruction of this top layer itself, as it ultimately forms the helical gold nanowires. Using first-principles techniques, they show that for isolated monolayers it is energetically favorable for both gold and silver to transform into hexagonal-close-packed arrangements. However, it is more energetically favorable for gold to contract than silver, leading to the observed surface reconstruction for gold. Silver gains approximately 23 mRy per atom in contracting, while gold gains more than 60 mRy per atom, or about 2.5 times more energy than silver.

As a starting point we carried out calculations for silver, with an atomic number of 47 and a ground state configuration of $[81].4d^{10}.5s^{1}$, instead of gold, with an atomic number of 79 and a ground state configuration of $[Xe].4f^{14}.5d^{10}.6s^{1}$. Modeling gold

nanotubes requires addressing the added complexities due to the increased number of electrons and complications due to relativistic effects. Therefore calculations for analogous gold systems are left for future work.

If the systems of gold are to be tackled in the future one needs to account for the added complexities due to the increased number of electrons per atom and relativistic effects. One way to handle both issues is by incorporating effective core potentials that model the core as a whole and address the valence electrons involved in bonding as opposed to an all-electron conventional basis set.[82] Effective core potentials incorporate relativistic effects internally, which means that the existing code would not need modification with respect to the addition of extra terms in the Hamiltonian to account for relativistic effects. One may also incorporate relativistic treatments using Douglas-Kroll-Hess approaches. [81, 83-85]

CHAPTER 4

ZnO NANOSTRUCTURES

4.1 Introduction

ZnO, a geometrically versatile II-VI semiconductor material, can form nanodots, nanorods, nanowires, nanobelts, nanotubes, nanobridges, nanonails, nanowalls, nanohelixes, nanorings, and nanocages.[17-26] ZnO is a direct band-gap (E_g = 3.37 eV) semiconductor with a large exciton binding energy (60meV), exhibiting near-UV emission, transparent conductivity, and piezoelectricity. Due to its many favorable characteristics, including bio-friendliness, it has received considerable attention lately, particularly with respect to applications involving optoelectronics and sensing.

Wireless devices are particularly attractive for biomedical applications, and self-powered devices are especially ideal. Wang and Song recently converted nanoscale mechanical energy into electrical energy by deforming piezoelectric zinc oxide nanowires with an atomic force microscope (AFM) tip.[86] As a consequence of their findings, we are interested in not only how the electronic and optical properties of these systems vary according to geometry but also how these properties change further upon slight deformations (i.e. stretching and twisting) of their structural configurations. Herein, we examine the electronic properties for different geometrical configurations of ZnO single-wall nanotubes and bulk-like nanowires and nanotubes, and we study the optical cross sections using an Ehrenreich – Cohen formalism.[28]

Nanotubular structures are typically grown from materials with a layered structure, such as graphite or graphite-like structures (BN, BCN, WS_2, MoS_2). [87] To date, however, no related ZnO nanotubular structures, i.e. single-wall ZnO nanotubes, have been reported. Nonetheless, despite limitations in the experimental realm recent theoretical reports have addressed this possibility. It is with this motivation and the desire to understand fundamental properties of these potential systems that we pursue the current study involving ZnO single-wall nanotubes.

A variety of procedures have been reported for constructing ZnO nanowires and nanorods.[4, 88, 89] Perhaps the most interesting is a study by Yin et al., in which nanorods with radii of 1.1 ± 0.1 nm were fabricated.[4] Due to the radii of the nanorods being smaller than the exciton Bohr radius (2.34 nm), quantum confinement effects were observed. Most notably, the exciton binding energy was significantly enhanced. Changes in the spectra of ZnO nanobelts have also been observed. In a study by X. Wang et al., a 120 meV blueshift was observed in the spectra of ZnO nanobelts.[5] These nanobelts were recently converted into super-lattice structured nanohelices.[7]

Although ZnO nanowires and nanorods have received comparatively more attention than ZnO nanotubes, a large variety of studies do exist involving the fabrication of ZnO nanotubes with bulk-related geometries.[26, 87, 90-103] For example, Xu et al. observed ZnO nanotubes with 'thick' single and double walls;[92] these tubes were grown along the [0001] direction of the hexagonal wurtzite structure and had wall thicknesses of approximately 15 nm (as opposed to a monolayer-sheet thickness as in carbon nanotubes) with diameters ranging from 50 to 100 nm. Xing et al. also synthesized ZnO nanotubular structures with geometries related to the hexagonal

structure of the ZnO crystal; they produced tubes with wall thicknesses as small as 4 nm with diameters ranging from 30 to 100 nm.[87]

4.2 Computational Methods

Herein, we study the electronic and optical properties of ZnO single-wall graphitic-like nanotubes, ZnO single-wall bulk like nanotubes, and ZnO ultrathin nanowires. We are particularly interested in the behavior of the total energies and optical cross sections with respect to structural changes. The methodology behind our approach and details of the geometrical models considered are the subject of the following sections. The first-principles optical absorption spectra calculated within an Ehrenreich – Cohen formalism was discussed in Section 2.6.[28] A discussion reviewing the details of the Mulliken Population analysis used throughout the ZnO study is available in Section 2.5.

4.3 ZnO Nanotubes: Single-Wall

4.3.1 Overview

In a recent theoretical study using *ab initio* density functional methods, Claeyssens et al. calculated a new energetically favorable 'graphitic'-like structure for ZnO thin films (< 10 layers).[27] If it is indeed possible for ZnO to exist in a graphitic-like structure, it certainly fuels the question as to whether ZnO could exist in single-wall structures similar to carbon nanotubes. In another theoretical study, Erkoç and Kökten examined the structural and electronic properties of armchair and zigzag single-wall ZnO nanotubes by carrying out semiempirical molecular orbital self-consistent field calculations at the level of AM1 method within the RHF formulation.[104] Erkoç and Kökten obtained an energy gap of 0.02 eV for the (4,4) armchair ZnO nanotube, while they calculated an energy gap of 4.40 eV for the (4,0) zigzag ZnO nanotube. [104] Therefore, their results suggested that armchair ZnO nanotubes behave like narrow-gap semiconductors whereas zigzag ZnO nanotubes are insulating. In sharp contrast, we determined all ZnO single-wall nanotube structures to be semiconducting with little variation in the bandgap.

Herein we calculated the electronic and optical properties of ZnO single-wall nanotubes with varying geometries, both chiral and non-chiral, with radii ranging from approximately 2.10 Å to 5.38 Å. The geometry was optimized according to bond length, which varied from 1.87 Å to 1.90 Å according to structure. The LDF method discussed in section 1.3.6 was implemented, with 128 k points in the Brillioun zone along with a 6-31G basis set. [105] The optical properties were calculated using the LDF results within the Ehrenreich – Cohen formalism outlined in section 1.3.9.

4.3.2 Geometries

ZnO single-wall nanotubes were modeled using the same geometrical approach as for carbon nanotubes.[32] Each Bravais lattice vector, $\boldsymbol{R}$, is defined by two primitive lattice vectors $\boldsymbol{R}_1$ and $\boldsymbol{R}_2$ illustrated in Figure 2.1 and a pair of integers (n_1,n_2) so that

$$\boldsymbol{R} = n_1\boldsymbol{R}_1 + n_2\boldsymbol{R}_2 \qquad (4.1)$$

Basis vectors are defined as

$$\boldsymbol{R}_1 = a\hat{i} \qquad (4.2a)$$

$$\boldsymbol{R}_2 = \frac{a}{2}\hat{i} + \frac{a\sqrt{3}}{2}\hat{j}, \qquad (4.2b)$$

where $a = \sqrt{3}d$ is the nearest-neighbor bond distance within a ZnO pair, and $\hat{i}$ and $\hat{j}$ are the unit vectors along the x and y directions. The radius for an (n_1, n_2) nanotube is given by

$$\rho = \frac{|\boldsymbol{R}|}{2\pi} = \frac{a}{2\pi}\sqrt{n_1^2 + n_2^2 + n_1 n_2}, \qquad (4.3)$$

Each $\boldsymbol{R}$ within this wedge defines a different ZnO SWNT and all unique ZnO SWNTs are generated by this set of $\boldsymbol{R}$'s. The (n_1,0) – type structures are referred to as zigzag while the (n_1,n_2) – type structures are referred to as armchair nanotubes. All other structures are chiral. In this study, we consider twenty-six different zigzag, armchair, and chiral structures labeled in Figure 4-1 with selected nanotubes illustrated as ball and stick models in Figure 4-2.

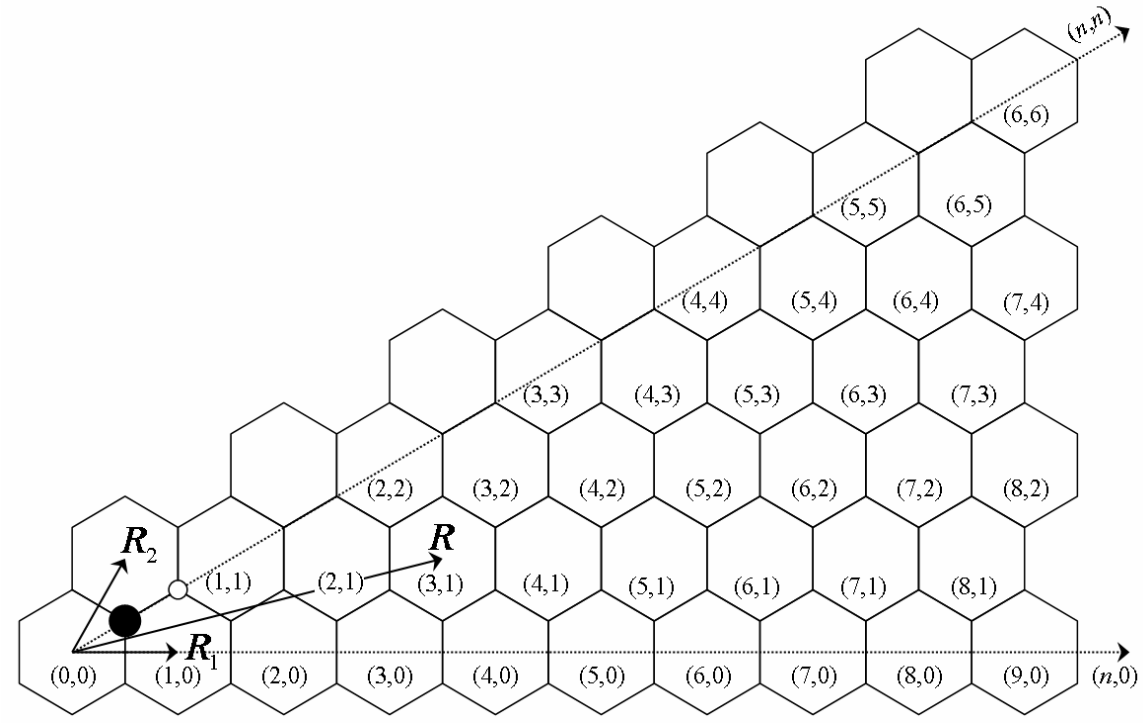

Figure 4-1. Irreducible wedge of a honeycomb lattice indicating ZnO single-wall nanotube geometry. The same numbering scheme as carbon nanotubes is used with zigzag nanotubes defined by rollup vectors along the (n,0) direction and armchair nanotubes defined by rollup vectors along the (n,n) direction.

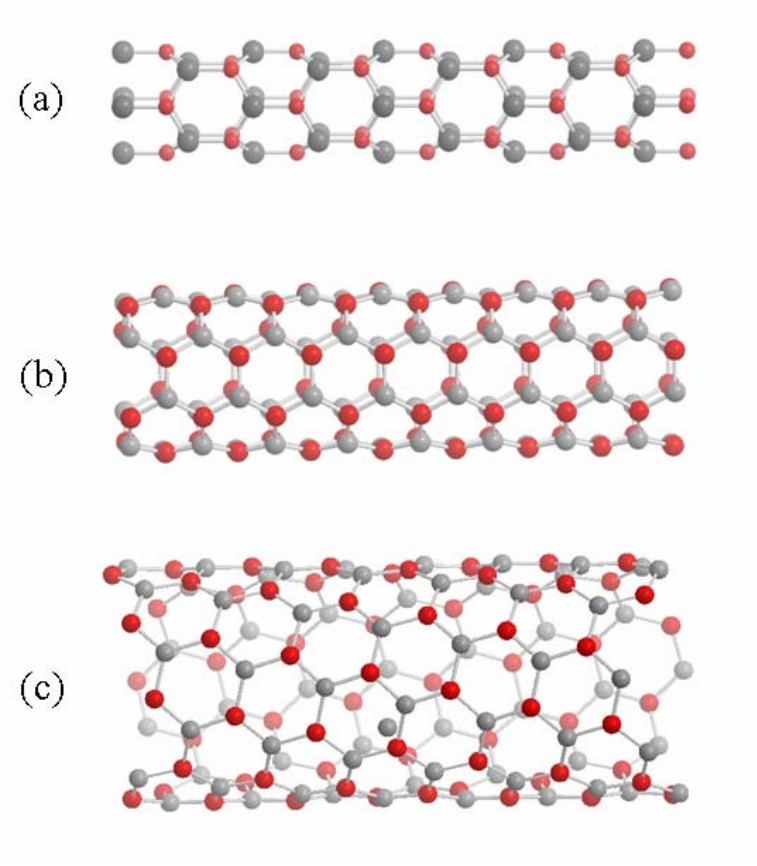

Figure 4-2. Ball and stick models of selected ZnO nanotubes: (a) (4,0) zigzag, (b) (4,4) armchair, and (c) (7,3) chiral nanotube.

4.3.3 Energetic Results

Energetic trends for the ZnOSWNTs with respect to nanotube radius differ from what we would expect; the total energy does not exhibit any dependence on nanotube radius. Elastic strain models, such as those used for carbon SWNTs, would predict that the total strain energy should increase as the radius decreases. The strain energy per carbon atom in carbon nanotubes relative to an unstrained graphite sheet scales as $1/R^2$ (where R is the tube's radius).[35] Instead of a smooth $1/R^2$ trend, we observe a random pattern within our results, as shown in Fig. 4-3. The corresponding numerical data is given in Table III. In addition, contrary to the AgSWNTs, grouping the nanotubes by geometry does not result in any improvements or alternative energetic dependencies on nanotube radius.

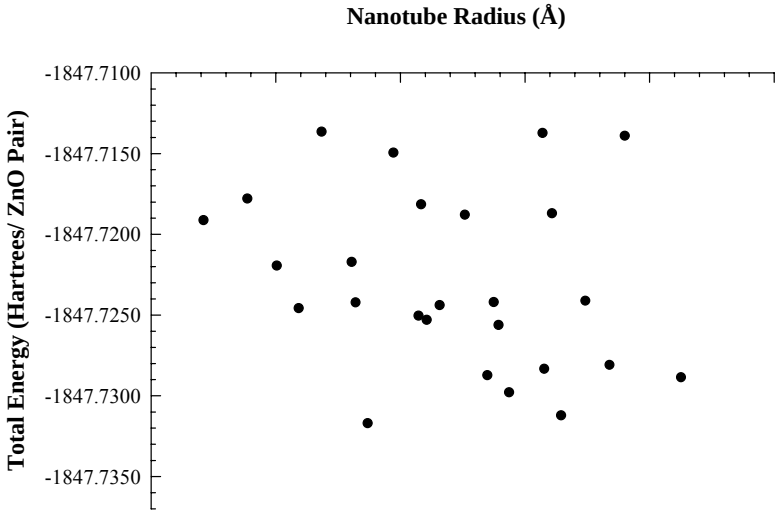

Figure 4-3. Total energy versus nanotube radius for all ZnOSWNTs considered herein. Unlike single-wall carbon nanotubes, there is no energetic dependency on nanotube radius.

Structure	Radius (Å)	N_{ZnO}	Total Energy (Hartrees/N_{ZnO})
(4,0)	2.0951	4	-1847.7191
(4,1)	2.4002	1	-1847.7178
(5,0)	2.6050	5	-1847.7219
(4,2)	2.7569	2	-1847.7246
(5,1)	2.9162	1	-1847.7136
(6,0)	3.1260	6	-1847.7217
(4,3)	3.1524	1	-1847.7242
(5,2)	3.2365	1	***-1847.7317***
(6,1)	3.4165	1	-1847.7149
(4,4)	3.5905	4	-1847.7250
(5,3)	3.6084	1	-1847.7181
(7,0)	3.6470	7	-1847.7253
(6,2)	3.7371	2	-1847.7244
(7,1)	3.9127	1	-1847.7188
(5,4)	4.0692	1	-1847.7287
(6,3)	4.1135	3	-1847.7242
(8,0)	4.1460	8	-1847.7256
(7,2)	4.2195	1	-1847.7298
(8,1)	4.4515	1	-1847.7137
(5,5)	4.4643	5	-1847.7283
(6,4)	4.5180	2	-1847.7187
(7,3)	4.5818	1	-1847.7312
(8,2)	4.7498	2	-1847.7241
(6,5)	4.9175	1	-1847.7281
(7,4)	5.0244	1	-1847.7139
(6,6)	5.3838	6	-1847.7289

Table III. The total energies per structure are listed by increasing radii, and N_{ZnO} represents the number of ZnO pairs per unit cell. The structure with the lowest total energy, the (5,2) ZnOSWNT, is shown in bold italics.

Although the nanotube radii for all the nanotubes considered herein ranged from 2.0951 Å to 5.3838 Å, the (5,2) ZnOSWNT with a radius of 1.8686 Å had the lowest total energy of -1847.7317 Hartrees per ZnO pair, while the (5,1) ZnOSWNT with a radius of 2.9162 Å had the highest total energy of -1847.7136 Hartrees per ZnO pair. Despite the absence of an energetic trend with respect to nanotube radius, the total energies of the single-wall structures are comparable with the other structures examined herein. For example, a ZnO nanowire with a radius of approximately 4 Å oriented along the *c*-axis has a total energy per ZnO pair of -1847.7239 Hartrees, while a ZnO nanowire with a comparable radius in the rock-salt structure has a total energy per ZnO pair of -1847.7243 Hartrees.

Results from the Mulliken population analysis are presented in Table IV. The atomic populations for Zinc and Oxygen are plotted versus nanotube radius in Fig. 4-4. In general, there is a charge transfer on the order of 0.72*e* from Zinc to Oxygen. Although there is not a monotonic linear trend, the amount of charge transfer from Zinc to Oxygen is slightly less overall for nanotubes of smaller radii and more for nanotubes of larger radii. Erkoç and Kökten present a similar trend in the finite armchair and zigzag nanotubes.[104] They report a charge transfer on the order of 0.64*e*, from Zn to O, for the (4,0) ZnOSWNT and on the order of 0.67*e*, from Zn to O, for the (4,4) ZnOSWNT. (For comparison, we find a charge transfer of 0.70*e*, from Zn to O, for the (4,0) ZnOSWNT and 0.72*e* for the (4,4) ZnOSWNT.) In their results, they report that atomic charges are developed almost equally on all atoms (negative on O, positive on Zn), except the end atoms of the zigzag model. Our results for extended systems show that

charge develops equally on all atoms, Zn and O respectively, regardless of their positions within the unit cell.

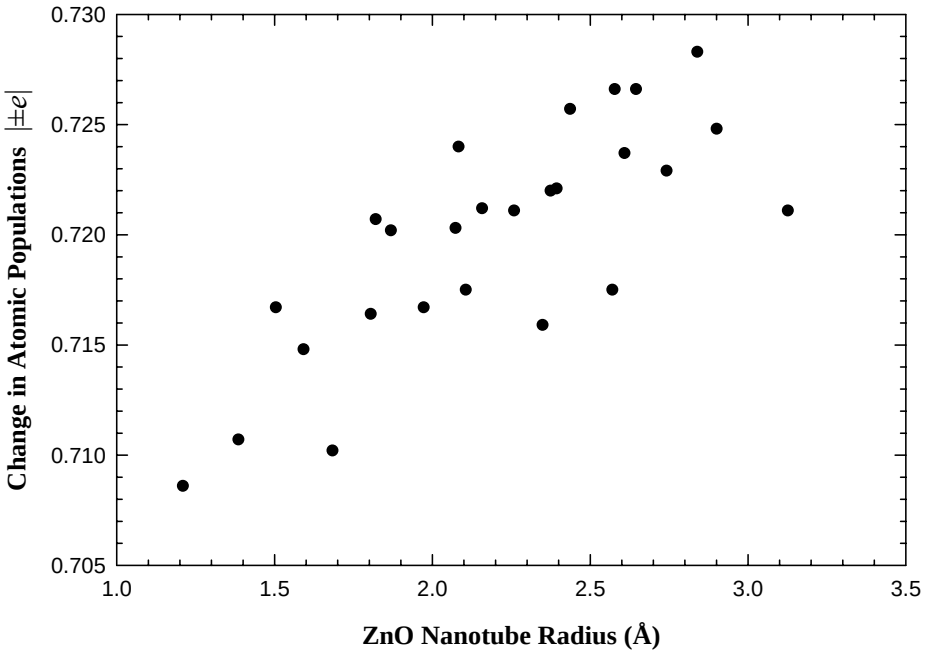

Figure 4-4. Change in atomic populations versus nanotube radius according to Mulliken population analysis data given in Table IV.

Structure	Radius (Å)	*Change in Atomic Populations* $\lvert\pm\Delta e\rvert$ (+Zn, -O)
(4,0)	2.0951	0.7086
(4,1)	2.4002	0.7107
(5,0)	2.6050	0.7167
(4,2)	2.7569	0.7148
(5,1)	2.9162	0.7102
(6,0)	3.1260	0.7164
(4,3)	3.1524	0.7207
(5,2)	3.2365	0.7202
(6,1)	3.4165	0.7167
(4,4)	3.5905	0.7203
(5,3)	3.6084	0.7240
(7,0)	3.6470	0.7175
(6,2)	3.7371	0.7212
(7,1)	3.9127	0.7211
(5,4)	4.0692	0.7159
(6,3)	4.1135	0.7220
(8,0)	4.1460	0.7221
(7,2)	4.2195	0.7257
(8,1)	4.4515	0.7175
(5,5)	4.4643	0.7266
(6,4)	4.5180	0.7237
(7,3)	4.5818	0.7266
(8,2)	4.7498	0.7229
(6,5)	4.9175	0.7283
(7,4)	5.0244	0.7248
(6,6)	5.3838	0.7211

Table IV. Mulliken population analysis for ZnO single-wall nanotubes.

4.3.4 Band Structures and Densities of States

The first-principles band structures and densities of states for the (4,0), (4,4), and (7,3) ZnOSWNT are shown in Figs. 4-5 through 4-7, respectively. Their band gaps are similar to each other, on the order of 1.1 eV, despite different radii and geometries. Our results are remarkably different than those by Erkoç and Kökten where they indicated that armchair (4,4) ZnO nanotubes behave like narrow-gap semiconductors, with an energy gap of 0.20 eV, while zigzag (4,0) ZnO nanotubes exhibit insulating behavior, with an energy gap of 4.40 eV.[104]

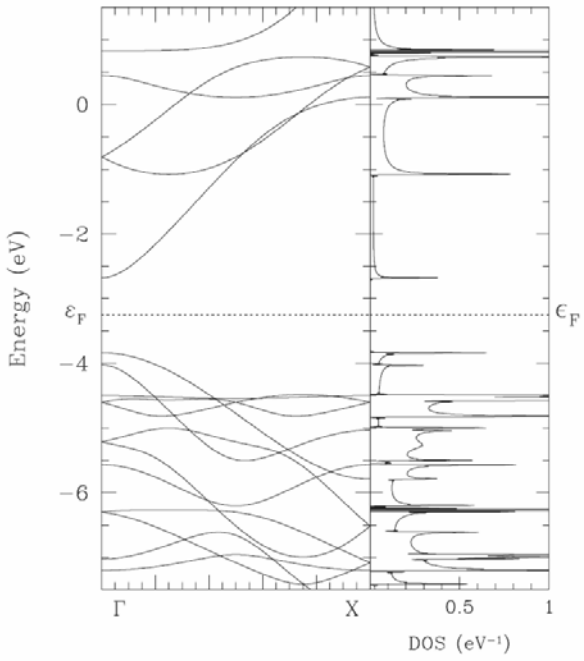

Figure 4-5. First-principles LDF band structure and density of states for the (4,0) ZnOSWNT. The Fermi level is indicated at -3.2576 eV.

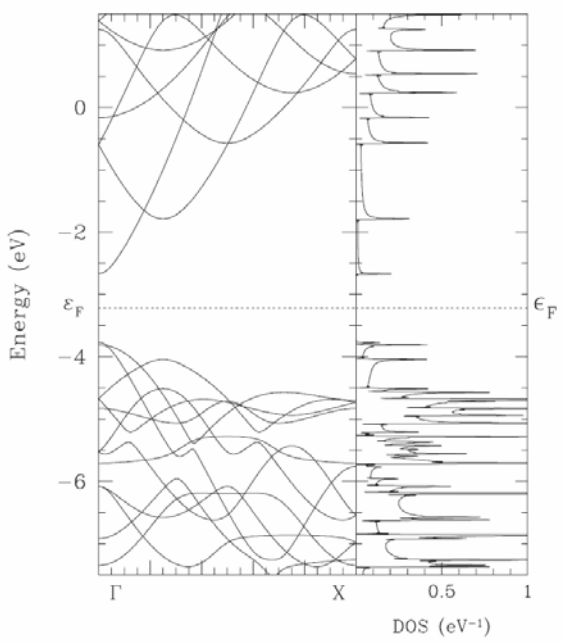

Figure 4-6. First-principles band structure and density of states for the (4,4) ZnOSWNT. The Fermi level is indicated at -3.2177 eV.

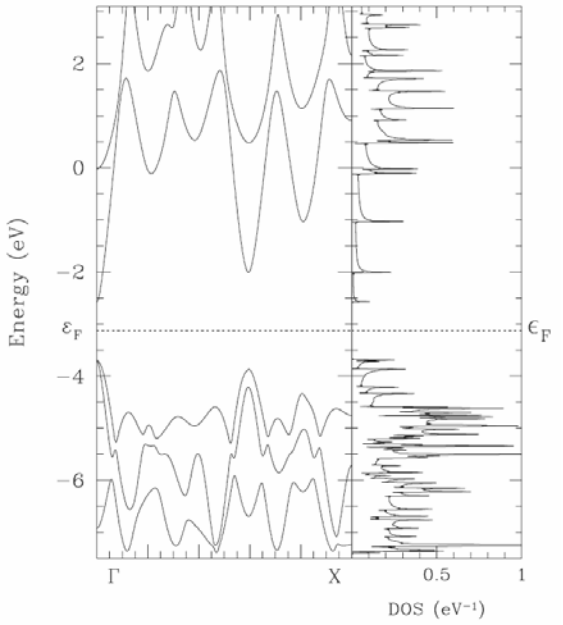

Figure 4-7. First-principles band structure and density of states for the (7,3) ZnOSWNT. The Fermi level is indicated at -3.1333 eV.

4.3.5 Optical Absorption Spectra

The optical spectra and the corresponding transitions within the band structures and densities of states for the (4,0), (4,4), and (7,3) ZnO single-wall nanotubes are given in Figs. 4-8 through 4-10, respectively. Solid blue lines represent direct transitions corresponding to polarizations parallel to the helical axis, while red dashed lines represent indirect transitions associated with polarizations perpendicular to the helical axis. Black solid lines represent the composite spectra. The spectra are mostly dominated by parallel transitions, while the peaks corresponding to perpendicular transitions are greatly suppressed in comparison.

The location of the first parallel peak, associated with the band gap, is fairly consistent throughout all the structures considered, irrespective of nanotube radii. However, the location of the second parallel peak increases with decreasing nanotube radii. For example, the radii of the (4,0), (4,4) and (7,3) ZnO SWNTs are: 2.10 Å, 3.59 Å, and 4.58 Å, while the locations of their second peaks are: 3.50 eV, 2.27 eV, and 1.88 eV.

The allowed transitions are best explained using symmetry arguments for the (4,0) and (4,4) nanotubes. The (4,0) zigzag nanotube has C_{4v} symmetry while the (4,4) armchair nanotube has C_4 symmetry. For the C_{4v} case, there are two types of *a* representations, a_1 and a_2, because the screw operator, $\hat{S}$, commutes with the reflection operator, $\hat{\sigma}$, over the set of *a* representation functions. On the other hand, for the C_4 case, $\hat{S}$ does not commute with $\hat{\sigma}$, and therefore there is only one *a* representation.

In the (4,0) zigzag nanotube with C_{4v} - type symmetry, the first few allowed transitions depicted in Fig. 4-8 are described as follows. The first peak corresponding to

parallel excitations occurs at 1.36 eV. This is a direct transition between two bands of a_1 - type symmetry. The second peak associated with a parallel excitation, occurring at 3.50 eV, is a direct transition between two bands of e_1 - type symmetry. There are two indirect transitions present, occurring between bands with different symmetries. The first peak associated with perpendicular polarization occurs at 2.34 eV; it arises from an indirect transition between bands of a_1 and e_1 type symmetries. The second peak arising from a perpendicular excitation occurs at 2.77 eV, and it is due to an indirect transition between bands of a_2 and e_1 type symmetries.

We shall now describe the allowed transitions occurring for the (4,4) armchair nanotube with C_4 type symmetry, as shown in Fig. 4-9. The first peak arising from a parallel excitation occurs at 1.11 eV. It is a direct transition between states of *a*- type symmetry. The second peak due to parallel excitations is located at 2.27 eV, and it is a direct transition between bands with e_1 – type symmetry. The third peak associated with a direct transition occurs at 4.16 eV, and it is between states of *b* – type symmetry. The peaks arising from perpendicular polarizations occur at 1.86 and 2.04 eV, and they result from indirect transitions between states of *a* and e_1 - type symmetries.

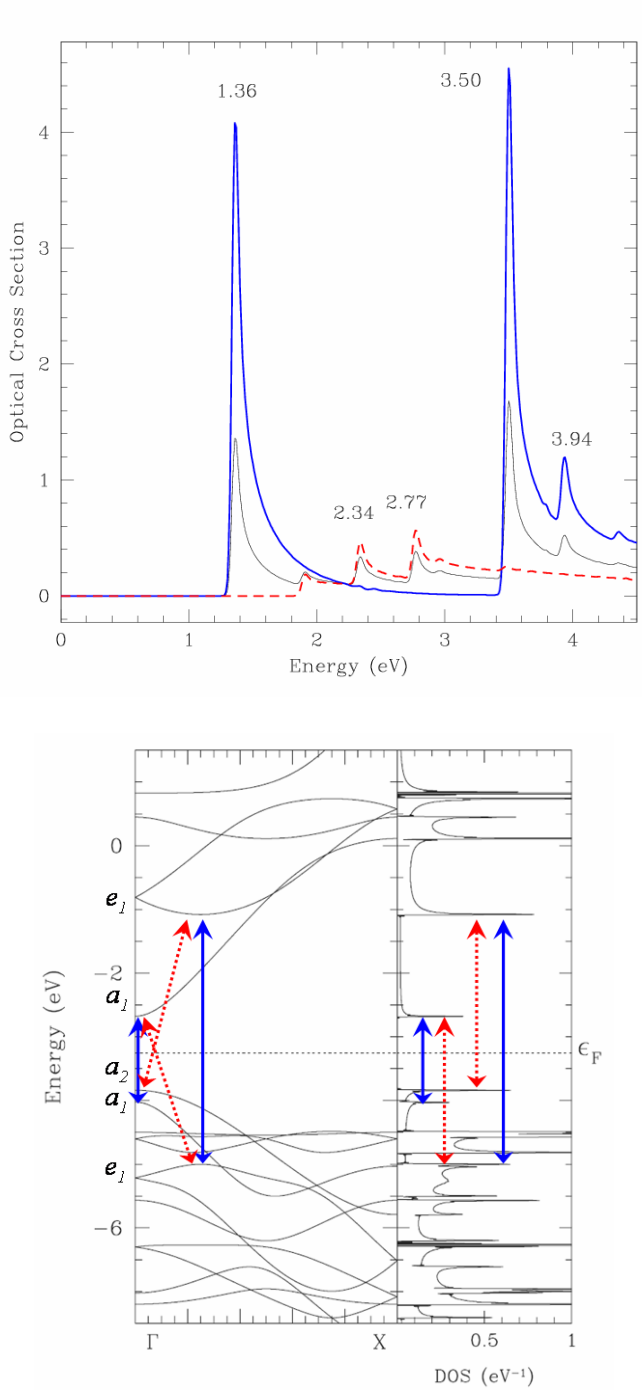

Figure 4-8. Optical absorption spectra and corresponding band structure and density of states for the (4,0) ZnOSWNT. Solid blue lines represent peaks corresponding to parallel polarizations, dashed red lines represent peaks corresponding to perpendicular polarizations, and black solid lines represent the total spectra.

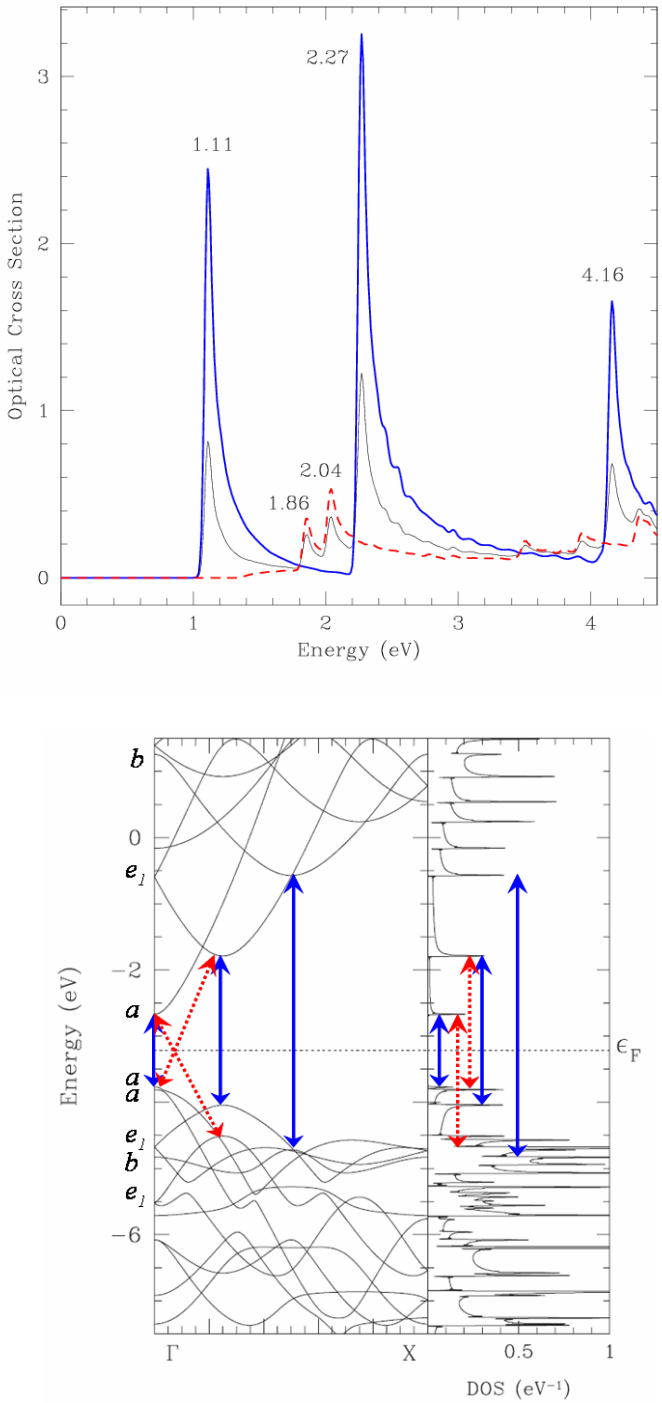

Figure 4-9. Optical absorption spectra and corresponding band structure and density of states for the (4,4) ZnOSWNT. Solid blue lines represent peaks corresponding to parallel polarizations, dashed red lines represent peaks corresponding to perpendicular polarizations, and black solid lines represent the total spectra.

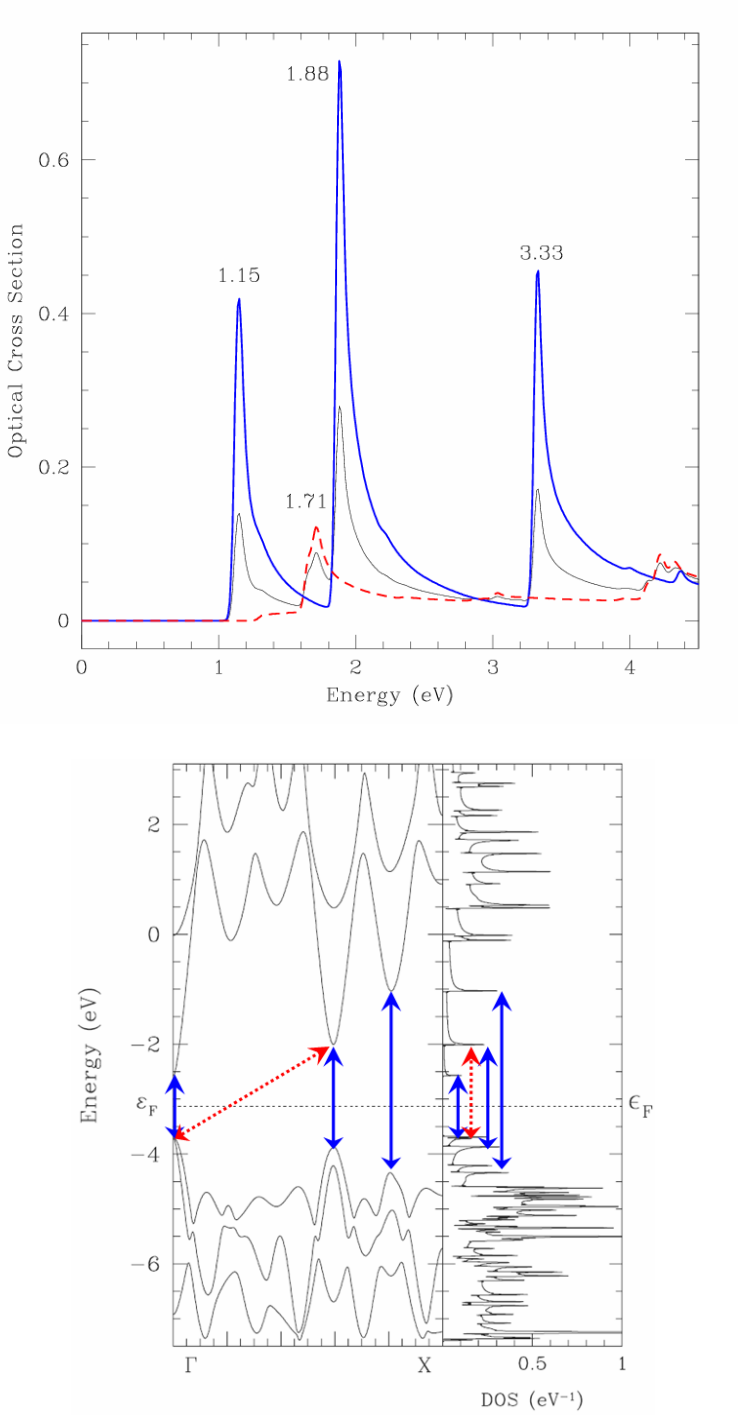

Figure 4-10. Optical absorption spectra and corresponding band structure and density of states for the (7,3) ZnOSWNT. Solid blue lines represent peaks corresponding to parallel polarizations, dashed red lines represent peaks corresponding to perpendicular polarizations, and black solid lines represent the total spectra.

The trend associated with the second parallel transition discussed previously holds true for all the single-wall nanotubes; the location of the second peak consistently increases as nanotube radius decreases. If we just consider the first two direct transitions, schematically illustrated in Fig. 4-11, along with the band gap, we observe the trend in peak energy versus nanotube radius plotted in Fig. 4-12. The corresponding numerical data is displayed in Table V. The band gap is defined as the difference between the lowest point of the conduction band and the highest point of the valence band at the central point (Γ) of the Brillioun zone.

In comparison to the second absorption peak, the energies of the band gap and first absorption peak remain fairly constant, (see Fig. 4-12). This is in contrast to behavior in carbon nanotubes; for in carbon nanotubes both peaks exhibit a dependence on nanotube radii. Upon further inspection, however, the energies of the band gap and first optical peak exhibit a peculiar trend, as revealed in Fig. 4-13. As the nanotube radius increases from approximately 2.10 Å to 5.38 Å, the band gap energy and energy of the first optical peak decrease, albeit not monotonically, as the nanotube radius increases. As the nanotube radius increases beyond 4.0 Å, the band gap energy and first optical peak energy increases somewhat before leveling off. Furthermore, as the nanotube radius increases, the band gap energy and first optical peak energy achieve a better agreement with one another.

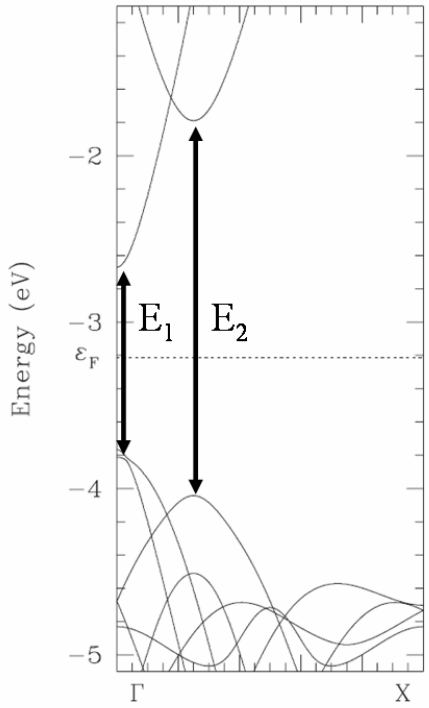

Figure 4-11. Schematic of energies corresponding to the first two excitations in the (4,4) ZnOSWNT due to parallel polarizations. The first transition is labeled as (E_1), while the second transition is designated as (E_2).

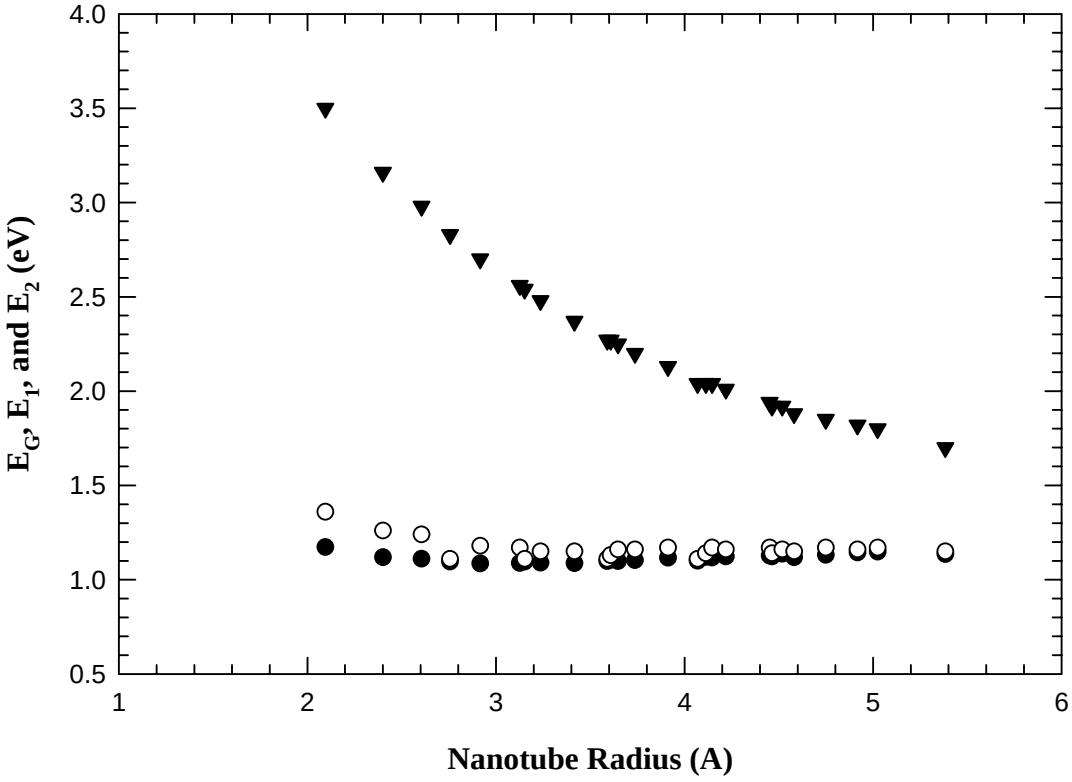

Figure 4-12. Energies corresponding to the band gap and first two excitations due to parallel polarizations versus nanotube radius for all ZnOSWNTs considered herein. The band gap is designated by closed circles (●), and the first optical absorption peak is designated by open circles (○). The second peak (E_2), represented by solid triangular points (▼), exhibits an energetic dependence on nanotube radius, while the first peak (E_1), does not exhibit a similar energetic dependence on nanotube radius.

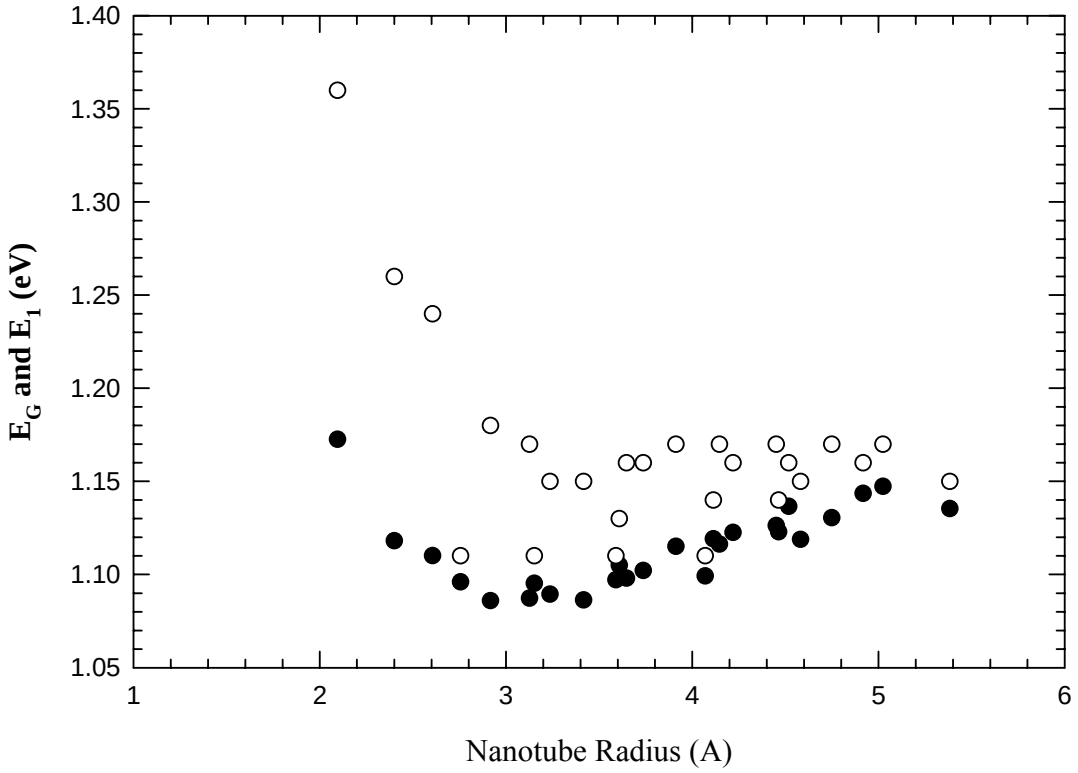

Figure 4-13. Zoomed-in perspective of the energies corresponding to only the band gap and first excitation due to parallel polarizations versus nanotube radius for all ZnOSWNTs considered herein. The band gap, E_G, is designated by closed circles (●), and the first optical absorption peak, E_1, is represented by open circles (○).

Structure	Radius (Å)	E_G (eV)	E_1 (eV)	E_2 (eV)
(4,0)	2.0951	1.1726	1.36	3.50
(4,1)	2.4002	1.1181	1.26	3.16
(5,0)	2.6050	1.1102	1.24	2.98
(4,2)	2.7569	1.0960	1.11	2.83
(5,1)	2.9162	1.0860	1.18	2.70
(6,0)	3.1260	1.0873	1.17	2.56
(4,3)	3.1524	1.0953	1.11	2.54
(5,2)	3.2365	1.0895	1.15	2.48
(6,1)	3.4165	1.0864	1.15	2.37
(4,4)	3.5905	1.0972	1.11	2.27
(5,3)	3.6084	1.1050	1.13	2.27
(7,0)	3.6470	1.0980	1.16	2.25
(6,2)	3.7371	1.1022	1.16	2.20
(7,1)	3.9127	1.1152	1.17	2.13
(5,4)	4.0692	1.0993	1.11	2.04
(6,3)	4.1135	1.1192	1.14	2.04
(8,0)	4.1460	1.1164	1.17	2.04
(7,2)	4.2195	1.1226	1.16	2.01
(8,1)	4.4515	1.1263	1.17	1.94
(5,5)	4.4643	1.1230	1.14	1.92
(6,4)	4.5180	1.1366	1.16	1.92
(7,3)	4.5818	1.1189	1.15	1.88
(8,2)	4.7498	1.1305	1.17	1.85
(6,5)	4.9175	1.1436	1.16	1.82
(7,4)	5.0244	1.1474	1.17	1.80
(6,6)	5.3838	1.1354	1.15	1.70

Table V. Energies of the first two excitation peaks due to parallel polarizations for ZnOSWNTs. Structures are listed according to increasing nanotube radii.

4.3.6 Structural Deformation Effects I: Longitudinal, Transverse, and Shear Strain

We now describe the procedure for determining the coordinates for a stretched nanotube obtained by first straining a 2D ZnO sheet with graphitic geometry and then mapping the atomic coordinates to the surface of a cylinder, thus creating the strained nanotube. We take into account the following quantities which are dimensionless: longitudinal (ε_l), transverse (ε_t), and shear (ε_s) strains.

This procedure is best explained by example, where we assume that we have an (n_1,n_2) single-wall nanotube where n_1 and n_2 are relatively prime. In this case, there are two atoms per unit cell – one Zinc and one Oxygen. (Otherwise there are 2N ZnO atom pairs per unit cell, where N is the greatest common divisor of the nanotube indices.) First we determine the (x,y) coordinates of the ZnO atom pair in the 2D sheet, where d represents the bond length between Zn and O nearest neighbors:

$$r_1 = \begin{pmatrix} 0 \\ d/2 \end{pmatrix} \tag{4.4a}$$

$$r_2 = \begin{pmatrix} 0 \\ -d/2 \end{pmatrix} \tag{4.4b}$$

We transform the coordinates to the "strip" reference frame as follows

$$x' = \frac{\left(\vec{r} \cdot \vec{R}\right)}{\left|\vec{R}\right|} \tag{4.5a}$$

$$y' = \frac{\left(\vec{r} \times \vec{R}\right) \cdot \hat{z}}{\left|\vec{R}\right|} \tag{4.5b}$$

These coordinates, now strained, are expressed as

$$x'' = (1 + \varepsilon_t)x' + \varepsilon_s y' \tag{4.6a}$$

$$y'' = (1 + \varepsilon_l) y' \tag{4.6b}$$

The strained coordinates are now transformed into cylindrical coordinates:

$$\rho = \frac{\left|\vec{R}''\right|}{2\pi} \tag{4.7}$$

$$\phi = \frac{2\pi \vec{r}'' \cdot \vec{R}''}{\left|\vec{R}''\right|^2} = \frac{2\pi x''}{R''} \tag{4.8}$$

Upon rolling up the sheet and forming the nanotube, the longitudinal strain (ε_l) corresponds to stretching the nanotube along the z-axis, the transverse strain (ε_t) is a radial expansion analogous to the radial breathing mode present in carbon nanotubes, and the shear strain (ε_s) represents a torsional twist along the nanotube's axis.

We are interested in changes to the total energy, Mulliken atomic population and optical properties upon introducing strain. In our following discussion, we consider three types of tubes, the (4,0) zigzag, (4,4) armchair, and the (7,3) chiral ZnO SWNTs. The starting point of the geometry of the nanotubes was already optimized according to bond length. We find that the total energies of the systems are not generally lowered upon introducing strain. Results of the total energies upon straining suggest that the geometrical configurations obtained previously, due to variations in bond length alone, are very close to optimal.

Figure 4-14 shows the change in total energy versus longitudinal strain. Although the (4,0) ZnO SWNT experiences a negligible lowering of total energy (approximately 2×10^{-4} Hartrees) upon compression, in general, the total energies of the nanotubes increase quadratically about zero upon introducing longitudinal strain. The total energy is

plotted versus transverse strain in Fig. 4-15. Again, the optimized energies are primarily centered about zero, indicating that ZnO single-wall nanotubes prefer not to be strained.

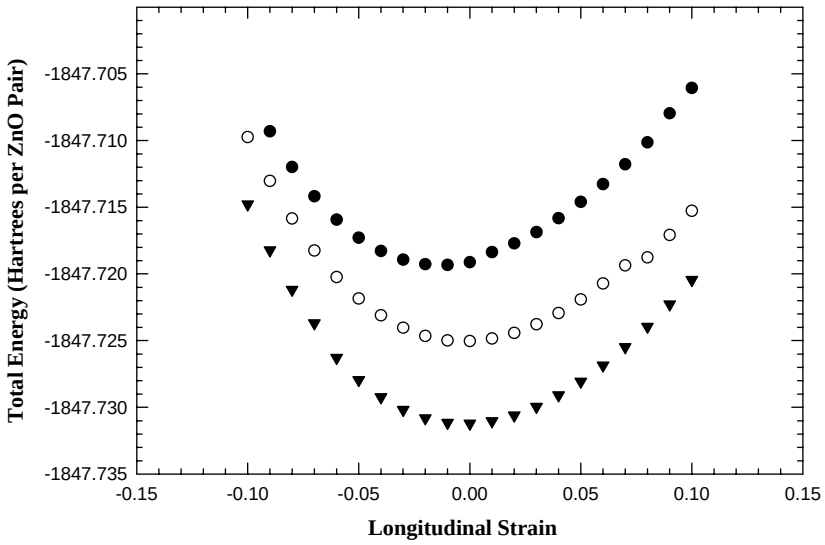

Figure 4-14. Total energy versus longitudinal strain for the (●) (4,0), (○) (4,4), and (▼) (7,3) ZnOSWNTs.

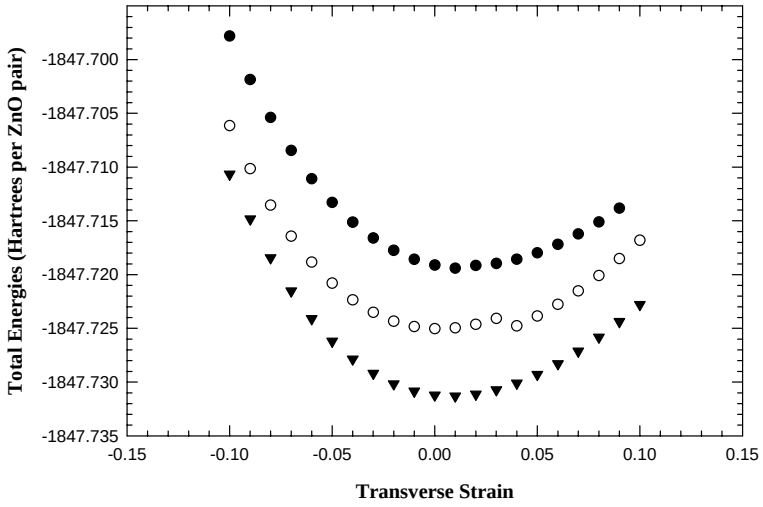

Figure 4-15. Total energy versus transverse strain for the (●) (4,0), (○) (4,4), and (▼) (7,3) ZnOSWNTs.

In Fig. 4-16. the total energy is plotted versus shear strain. While the total energy versus strain curve is smooth for the (7,3) ZnO SWNT, a similar smooth trend is not present for the tubes with higher symmetry, particularly with respect to the (4,4) ZnO SWNT. These results indicate that the (4,4) nanotube may prefer to experience a minor shear strain. However, these fluctuations are most likely a result of numerical noise.

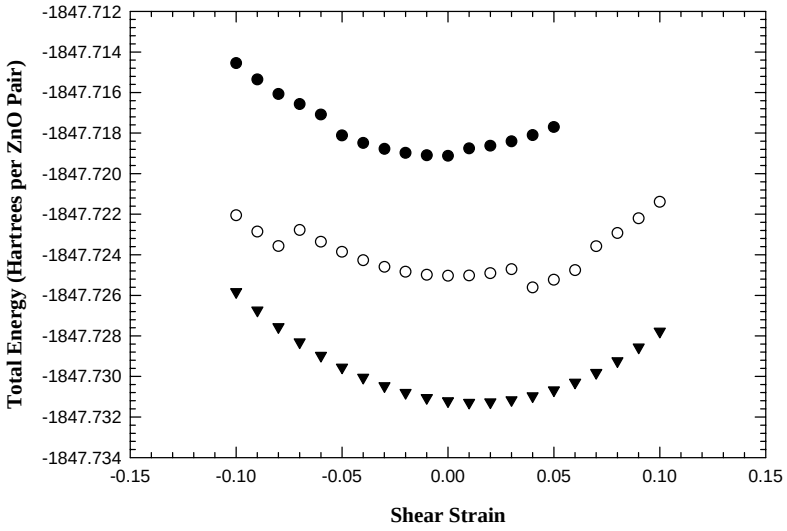

Figure 4-16. Total energy versus shear strain for the (●) (4,0), (○) (4,4), and (▼) (7,3) ZnOSWNTs.

Figures 4-17 and 4-18 illustrate the changes in Mulliken atomic populations due to longitudinal and transverse strain, respectively. Total charge transfer decreases as strain increases for both longitudinal and transverse strain. The Mulliken population decreases slightly faster with respect to longitudinal strain for the (4,0) nanotube, as indicated by Fig. 4-17. In addition, the (4,0) ZnO SWNT also exhibits a slightly different behavior with respect to transverse strain, as indicated in Fig. 4-18. The effect on atomic population is less as strain decreases, in comparison to the (4,4) and (7,3) nanotubes. The differences in behavior could be due to the (4,0) having a smaller radius in comparison to the other structures.

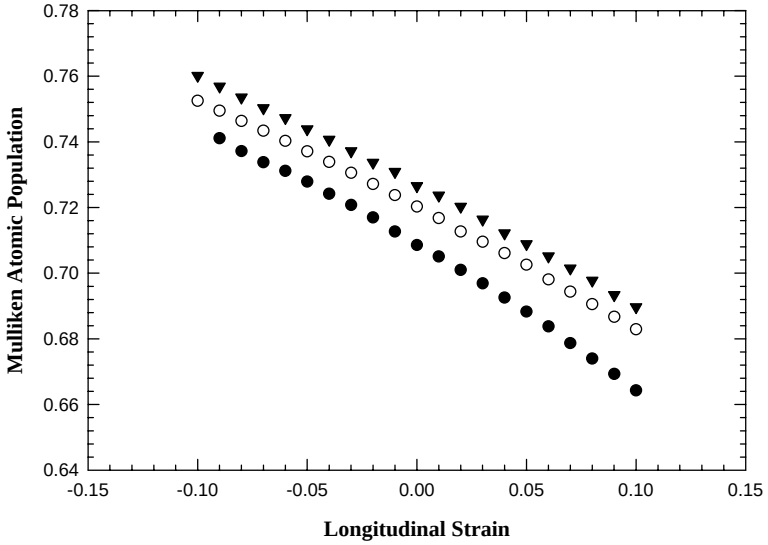

Figure 4-17. Mulliken atomic population versus longitudinal strain for the (●) (4,0), (○) (4,4), and (▼) (7,3) ZnOSWNTs.

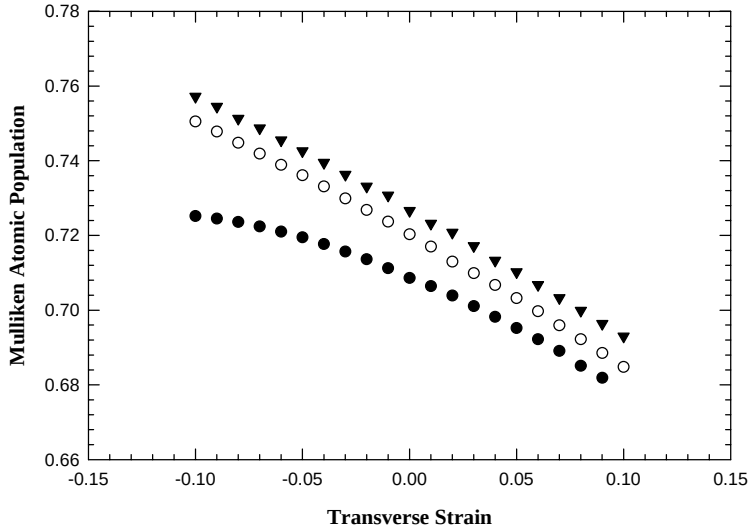

Figure 4-18. Mulliken atomic population versus transverse strain for the (●) (4,0), (○) (4,4), and (▼) (7,3) ZnOSWNTs.

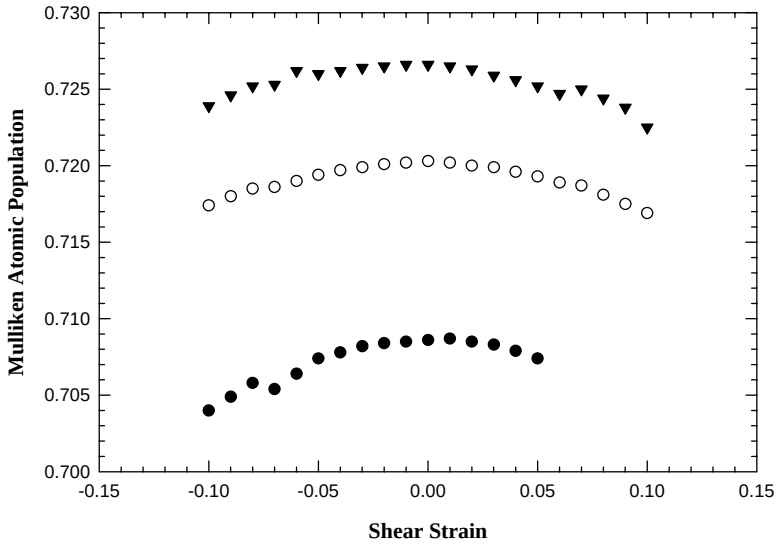

Figure 4-19. Mulliken atomic population versus shear strain for the (●) (4,0), (○) (4,4), and (▼) (7,3) ZnOSWNTs.

The optical absorption peaks shift in energy as a function of transverse and longitudinal strain. The E_1 and E_2 optical cross section peaks shift to higher energies in response to negative strain values, and they shift lower in energy in response to positive strain values. Figure 4-20. illustrates this concept for the (4,0) ZnOSWNT. Changes in the E_1 and E_2 optical absorption peaks due to longitudinal and transverse strain are shown in Figs. 4-21 and 4-24, respectively. We are primarily concerned with the behavior of the peaks resulting from direct transitions, as they are more intense than peaks due to indirect transitions in the optical spectra. Changes in the peaks due to shear strain are less straightforward. As illustrated in Figs. 4-25 through 4-27, the peaks split due to lifting of degeneracy.

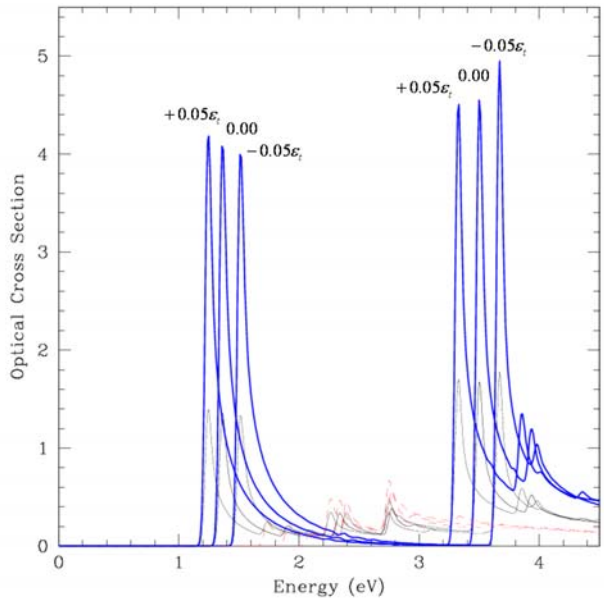

Figure 4-20. Changes in optical absorption spectra for the (4,0) ZnOSWNT due to transverse strain. Solid blue lines represent peaks corresponding to parallel polarizations, dashed red lines represent peaks corresponding to perpendicular polarizations, and black solid lines represent the total spectra.

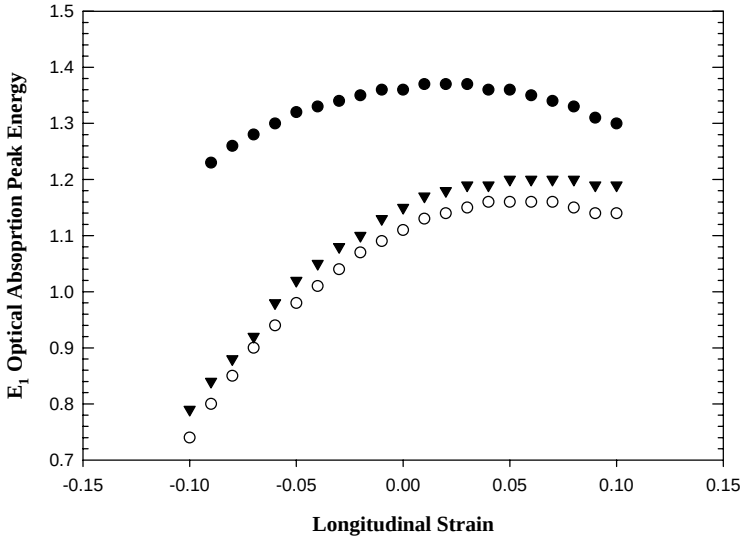

Figure 4-21. E_1 optical absorption peak position versus longitudinal strain for the (●) (4,0), (○) (4,4), and (▼) (7,3) ZnOSWNTs.

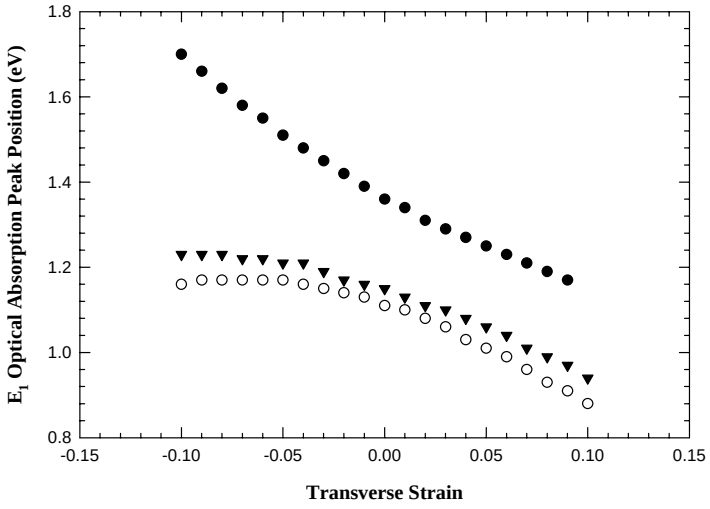

Figure 4-22. E_1 optical absorption peak position versus transverse strain for the (●) (4,0), (○) (4,4), and (▼) (7,3) ZnOSWNTs.

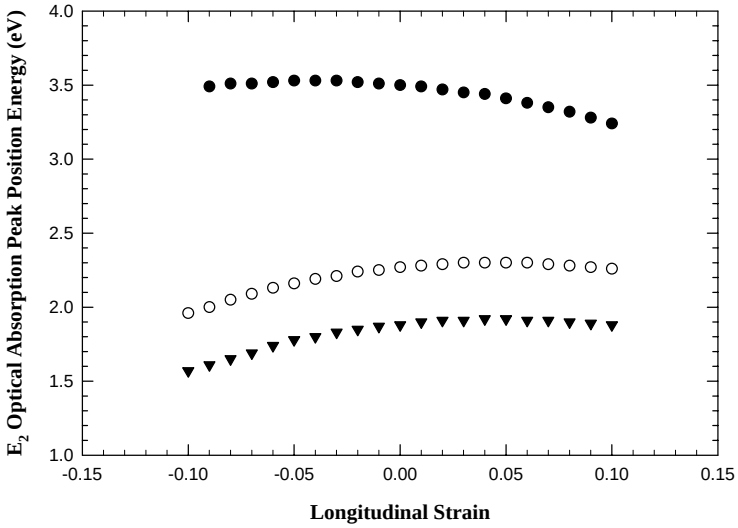

Figure 4-23. E_2 optical absorption peak position versus longitudinal strain for the (●) (4,0), (○) (4,4), and (▼) (7,3) ZnOSWNTs.

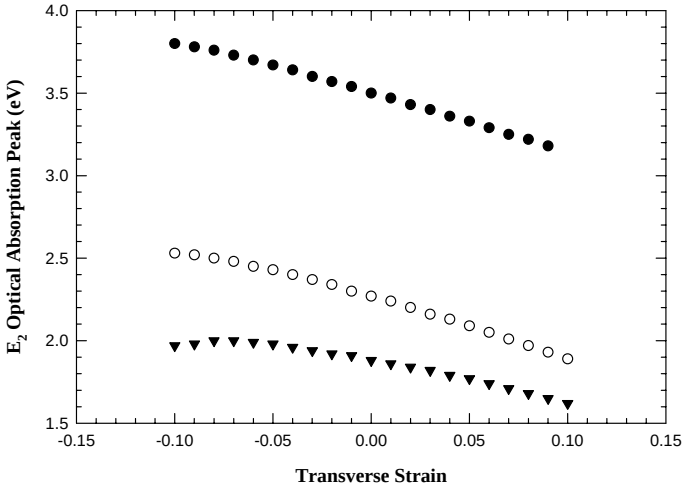

Figure 4-24. E_2 optical absorption peak position versus transverse strain for the (●) (4,0), (○) (4,4), and (▼) (7,3) ZnOSWNTs.

The optical absorption spectra for the unstrained and shear-strained cases are given in Fig. 4-25. for the (4,0) ZnO SWNT. The first longitudinal absorption peak for the unstrained nanotube is located at 1.36 eV, but upon introducing a shear strain, the peak splits into two separate peaks located at 1.05 and 1.35 eV. For the second peak, a shoulder appears in the spectra, indicating a possible splitting. As shown in Fig. 4-26, a similar situation arises for the (4,4) ZnO SWNT. The first longitudinal peak occurs at 1.11 eV, and upon inducing shear strain, two peaks are present at 0.97 and 1.23 eV. For the (4,4) ZnO SWNT, the splitting is also present in the second longitudinal peak occurring at 2.27 eV. Upon introducing shear strain, the second peak splits into two peaks located at 2.21 and 2.71 eV. The splitting is a result of breaking the symmetry which lifts the degenerate states located at the top of the valence band. The same splitting behavior arises in the (7,3) chiral ZnO SWNT, as shown in Fig. 4-27 For the (7,3) unstrained nanotube, the first peak occurs at 1.15 eV, and it splits into two peaks occurring at 0.95 and 1.26 eV. The second longitudinal peak, located at 1.88 eV for the unstrained case, splits into two peaks occurring at 1.78 and 2.20 eV. For the (7,3) nanotube, we also observe splitting of the third longitudinal peak.

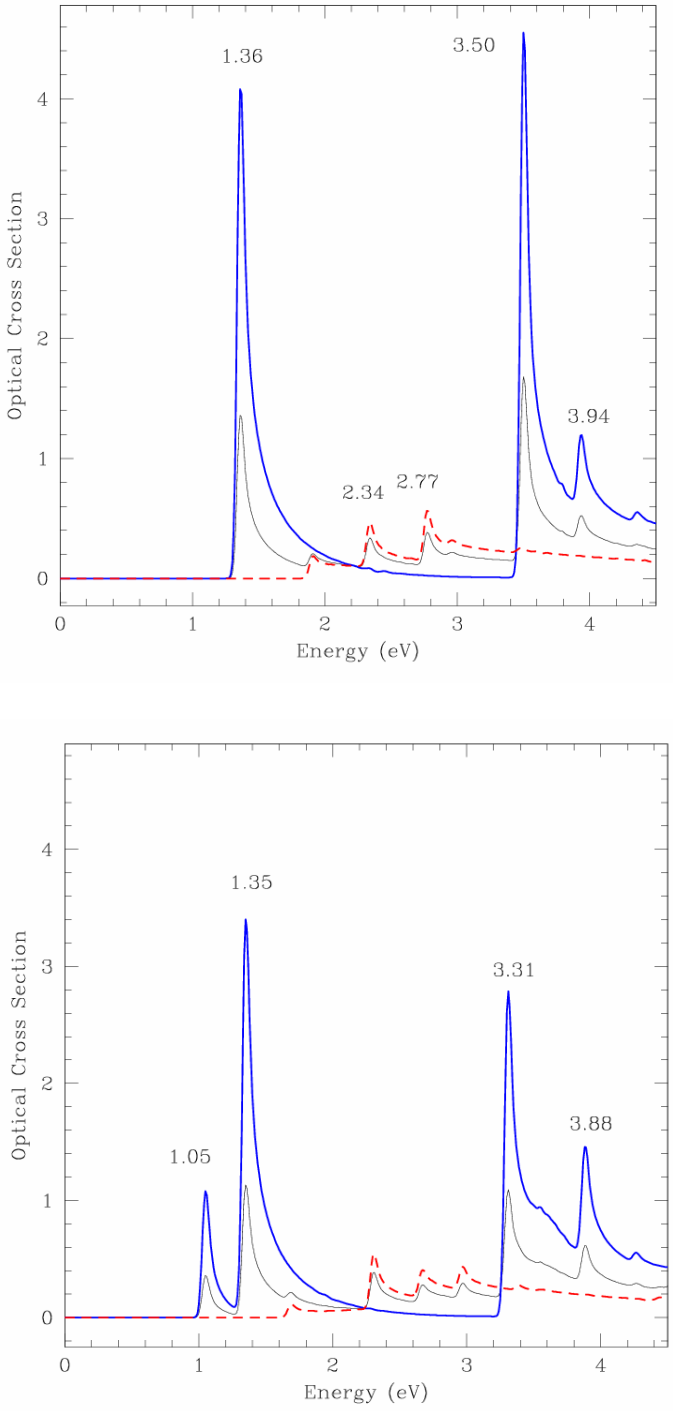

Figure 4-25. Optical absorption spectra for the (Top) unstrained and (Bottom) shear strained (-0.10 ε_s) (4,0) ZnOSWNT.

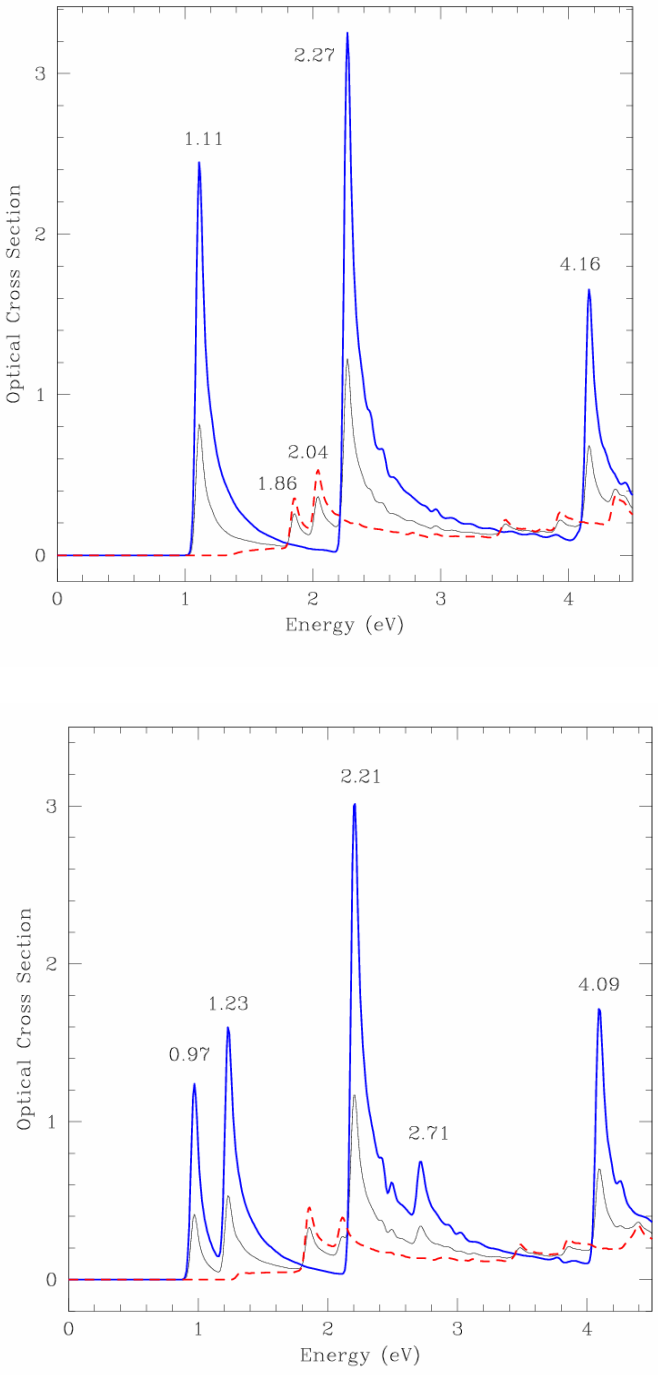

Figure 4-26. Optical absorption spectra for the (Top) unstrained and (Bottom) shear strained (-0.10 ε_s) (4,4) ZnOSWNT.

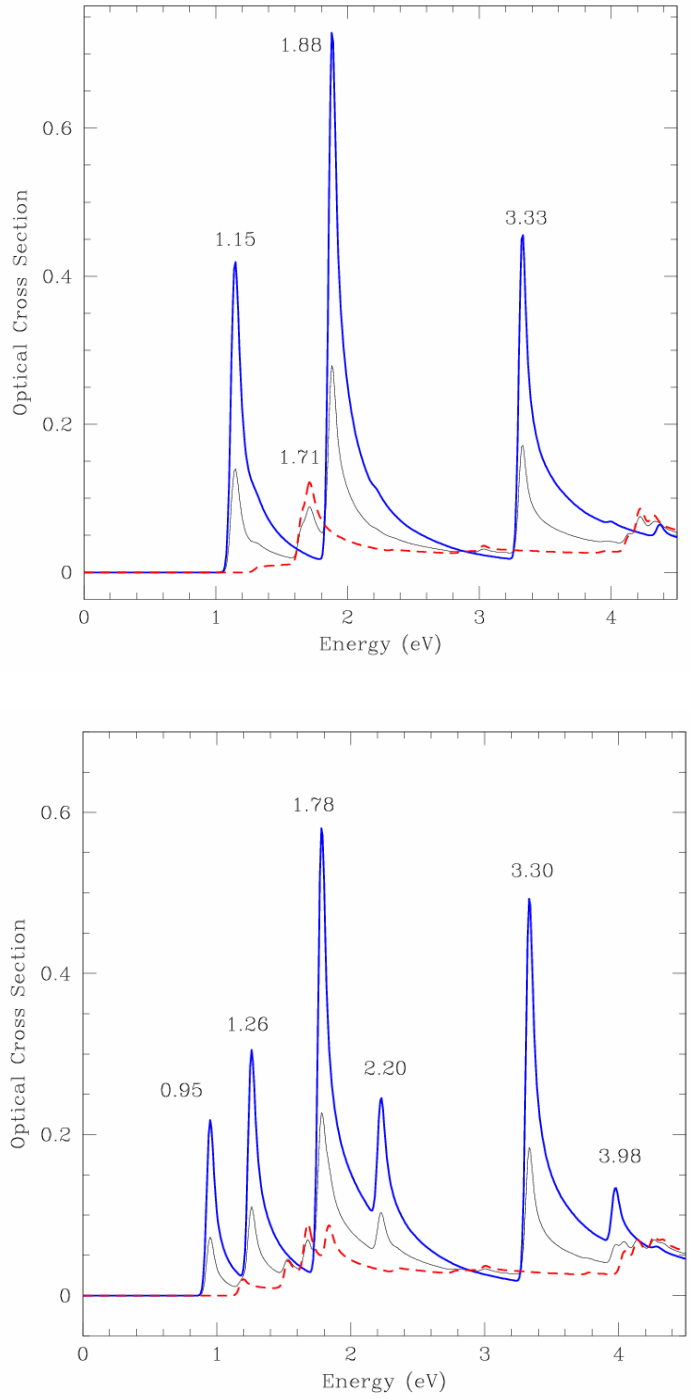

Figure 4-27. Optical absorption spectra for the (Top) unstrained and (Bottom) shear strained (-0.10 ε_s) (7,3) ZnOSWNT.

4.3.7 Structural Deformation Effects II: Puckering

The most energetically favorable structure for ZnO in bulk form is the tetrahedrally coordinated hexagonal wurtzite configuration. Due to the lack of experimental evidence concerning single-wall nanotubes, the possibilities pertaining to the detailed energetically favorable geometries of these systems remain open for consideration. The theoretical study reported by Claeyssens et al. [27] suggested that in thin films, ZnO may indeed favor a flat graphic-like structure. Although this supports the idea of ZnO being stable in a carbon nanotube-like configuration, other possibilities exist.

For example, would the "flat" structure preferable, or would a "puckered" configuration be more favorable for the single-wall nanotubes? In the study carried out by Erkoç and Kökten, they suggested that the ends of finite ZnO SWNTs may prefer to be puckered. Specifically, for the (4,0) ZnO SWNT, the ends terminated by Zn atoms preferred to be puckered inwards towards the *z*-axis of the nanotube, and although the (4,4) ZnO SWNT did not exhibit a similar behavior on the ends of the nanotube, the Zn and O atoms did not strictly lie within the same cylindrical plane.[104] We point towards another study, as motivation, in which the stability and electronic structures of phosphorus nanotubes with a puckered configuration were examined.[106]

Figure 4-28. illustrates the puckered geometry of the (4,4) ZnO SWNT considered herein. Two different geometrical variations were considered. The equilibrium or starting point configuration is shown in Figure 4-28(a) where both the Zinc and Oxygen atoms lie within the same cylindrical plane and hence along the same circumference. Figure 4-28(b) illustrates another possible puckered configuration in which the oxygen atoms are moved towards the inside of the nanotube and hence along the plane of a

smaller cylinder, indicated by the dashed line. In Figure 4-28(c), the oxygen atoms are moved outside of the plane of the original nanotube, lying in the plane of a cylinder with a larger radius, again denoted by a dashed line.

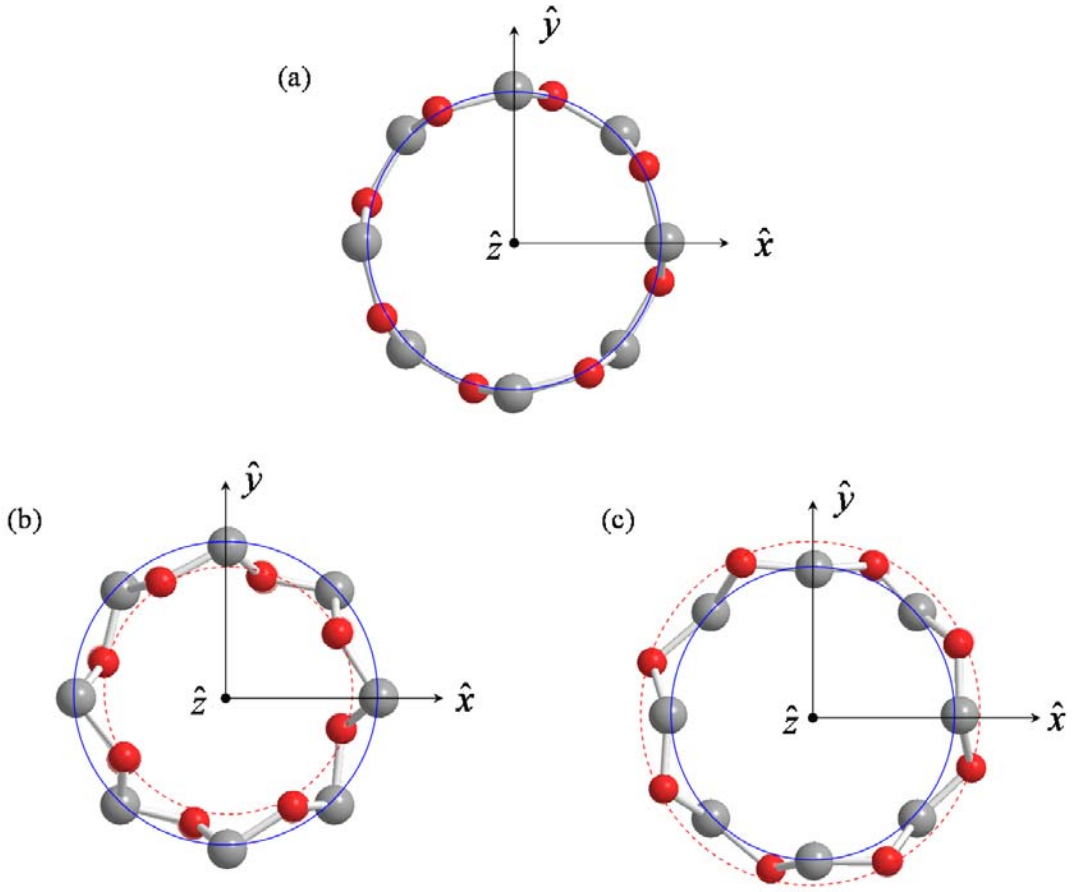

Figure 4-28. Puckered geometry of the (4,4) ZnOSWNT: (a) equilibrium conformation, i.e. Zn and O atoms lie along the same radius, (b) Oxygen atoms moved inside the nanotube along the circumference of a smaller radius, and (c) Oxygen atoms moved outside of the nanotube along the circumference of a larger radius.

Figure 4-29 illustrates the change in total energy versus pucker for the (4,4) ZnOSWNT. The amount of pucker is quantified by the change in radius of the plane in which the oxygen atoms lie, as indicated in Fig. 4-28. In this case, by increasing the radius of oxygen atoms in the nanotube by only a fraction of an Angstrom, the total energy decreases by a mere 4×10^{-5} Hartrees. As a result, due to the extremely fine deviations in energy, it is a safe approximation to assume that the single-wall nanotubes do not prefer substantial puckering.

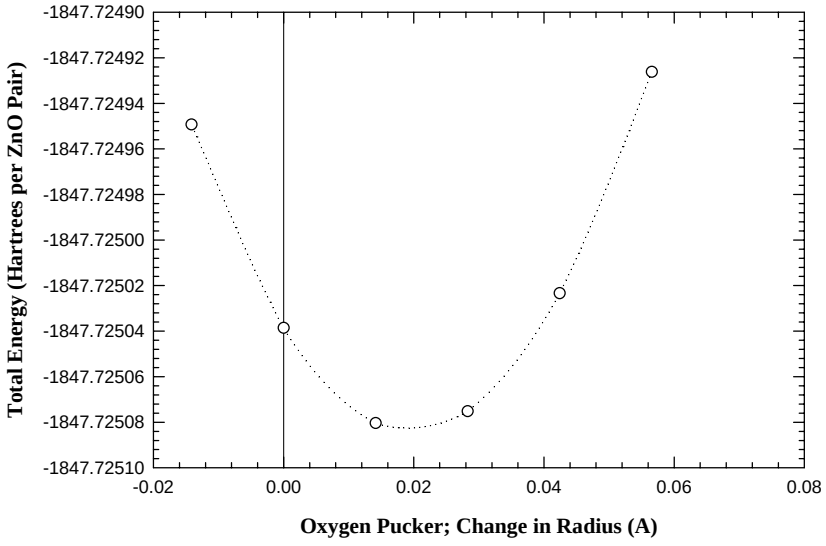

Figure 4-29. Total energy versus change in oxygen radius for the (4,4) ZnOSWNT.

Changes in Mulliken atomic population and changes in optical properties may are indicated in Figs. 4-30 to 4-32, respectively. As the oxygen atoms move outwards, increasing in radius up to 0.06 Å, the Mulliken population increases by nearly .04*e*. In Figs. 2.31 and 2.32, the E_1 and E_2 optical absorption peaks are plotted versus pucker. For the first absorption peak, E_1, the energy value changes from approximately 1.1 eV to 1.18 eV upon increasing the oxygen radius as much as 0.06 Å. The second peak, E_2, changes from approximately 2.27 eV to 2.32 eV.

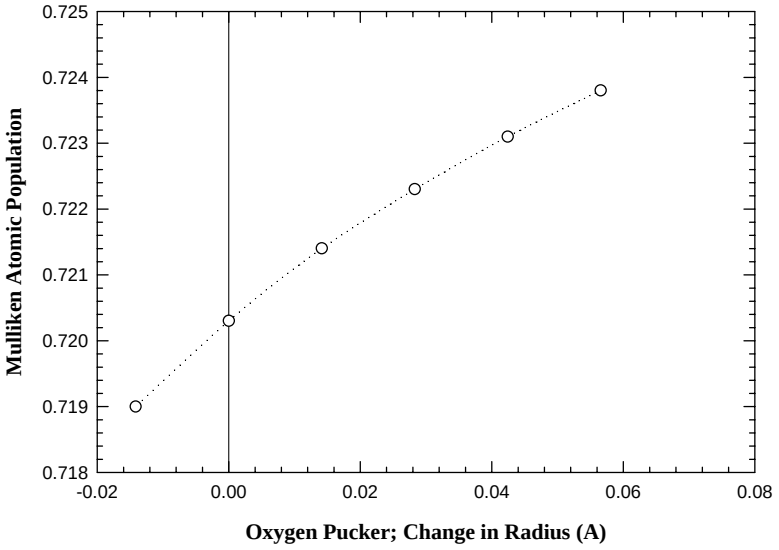

Figure 4-30. Mulliken atomic population versus change in oxygen radius for the (4,4) ZnOSWNT.

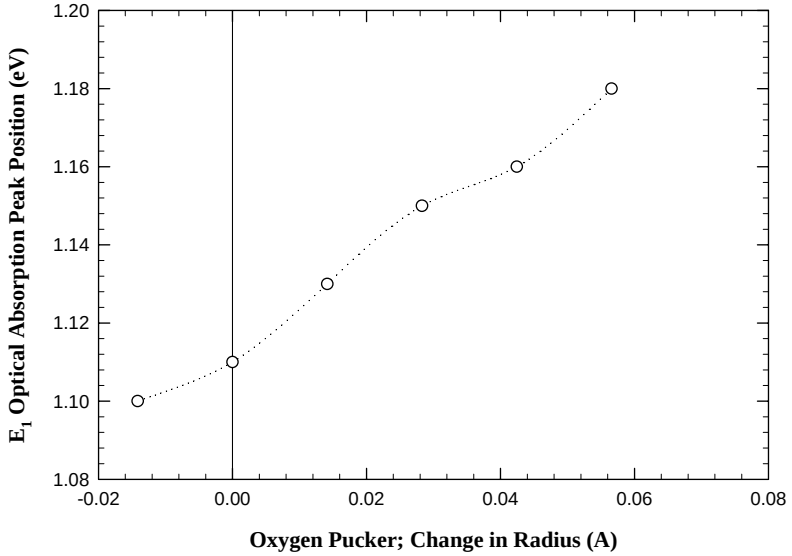

Figure 4-31. E_1 optical absorption peak position versus change in oxygen radius for the (4,4) ZnOSWNT.

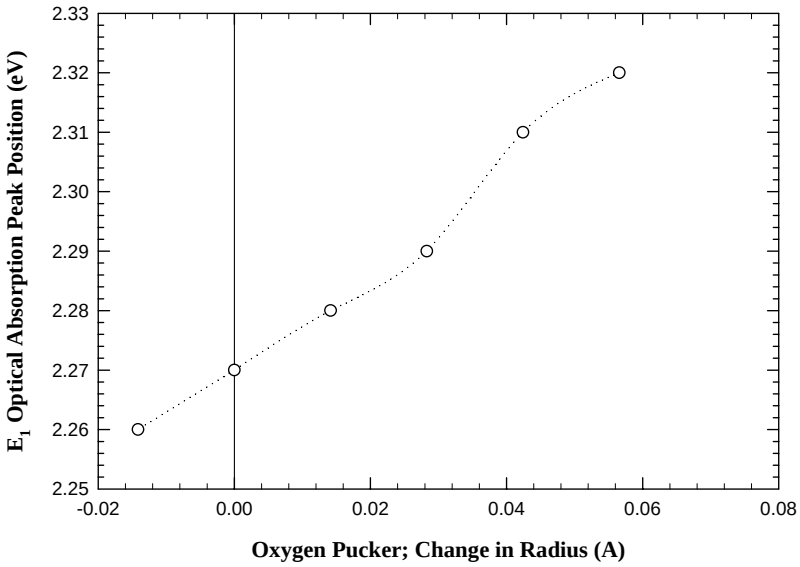

Figure 4-32. E_2 optical absorption peak position versus change in oxygen radius for the (4,4) ZnOSWNT.

4.3.8 Summary of Results

First-principles calculations were carried out on twenty-six ZnO single-wall nanotubes with different chiralities and radii ranging from 2.10 Å to 5.38 Å. The total energies of the single-wall nanotubes did not exhibit a dependence on nanotube radii, but results from the Mulliken population analysis do show some dependence on nanotube radii. While a strict linear trend is not present, the degree of charge transfer from Zn to O is generally less for nanotubes of smaller radii, approximately ±0.710*e*, and slightly more for larger nanotubes, approximately ±0.725*e*. The optical absorption spectra show a fascinating trend. While the first peak associated with a direct transition stays relatively stationary, roughly 1.25 eV, as nanotube radius varies, the second optical peak resulting from a direct transition displays a blue-shift from 1.70 eV to 3.50 eV with decreasing nanotube radius.

The analysis was extended to include structural deformation effects. Two types of effects were considered: straining and puckering. Overall, it is not energetically preferred to strain or pucker the single-wall tubes. The Mulliken atomic populations decrease linearly as longitudinal and transverse strain increases. With respect to puckering, as the oxygen atoms in the (4,4) nanotube move outwards, the Mulliken atomic population decreases.

The optical absorption spectra proved very sensitive to even the smallest structural deformations. For example, upon introducing a small transverse strain of ±0.05 ε_t, the first optical absorption peak, E_1, shifted from 1.36 eV to 1.25 eV and 1.51 eV, respectively, while the second peak, E_2, shifted from 3.50 eV to 3.33 eV and 3.67 eV, respectively. Upon taking into account shear strain, the peaks often split due to a lifting

of degeneracy. The optical absorption spectra of the (4,4) ZnOSWNT also reveals a shifting of peaks. For both the E_1 and E_2 peaks, the energies increase on the order of 0.05 eV as the oxygen atoms move outside of the nanotube's original cylindrical plane.

If these ZnO single-wall nanotubes which are structurally analogous to carbon nanotubes are ever produced experimentally, their greatest utility will likely involve their geometrically sensitive optical absorption spectra. In the next section, we explore ultrathin nanowires and a different type of ZnO nanotube; these nanotubes are modeled from cutting the core out of an ultra-thin ZnO nanowire in a hexagonal wurtzite or rocksalt structure, as opposed to mapping a sheet of atoms onto the surface of a cylinder. The results obtained in the next section also indicate that the single-wall ZnO nanotubes in a carbon nanotube-like configuration are the most energetically favorable nanotube structure.

4.4 ZnO Nanowires and Nanotubes: Bulk-Like

4.4.1 Overview

The most common growth direction for the ZnO nanorods and nanowires is along the $\pm[0001]$ direction, the *c*-axis, of the hexagonal wurtzite structure. However, ZnO may also crystallize in a zinc-blende or rock-salt structure under certain conditions. The two configurations we consider are hexagonal wurtzite and rock-salt. Ultrathin nanowires are calculated for both configurations. Due to the computational expense of large unit cell sizes, a limited variety of these structures were calculated. Nonetheless, because the radii of these ultra-thin nanowires are on the order of the single-wall nanotubes, they provide for some interesting comparisons. Bulk-like single-wall nanotubes were also considered. As opposed to the graphitic-like single-wall nanotubes discussed in the previous section, these bulk-like single-wall nanotubes are modeled directly from bulk configurations by 'cutting' a core section from the center of either the hexagonal wurtzite structure or the rocksalt structure.

Herein, our study includes two ultra-thin nanowires, one with a wurtzite structure and one with a rocksalt structure. We consider two types of bulk-like nanotubess constructed from the wurtzite structure: the (1,2) 3yH and (2,3) 6yH nanotubes, along with a rocksalt nanotube constructed from the rocksalt nanowire with a hallowed-out core. We proceed by introducing the detailed geometry of these systems. A discussion of results then follows, including a discussion of energetic results (total energies and Mulliken population analysis), band structures and densities of states, and optical cross sections.

4.4.2 Geometries

Most II-IV compound semiconductors (including ZnO) crystallize in either a hexagonal wurtzite or cubic zinc-blende structure where each anion is surrounded by four cations at the corners of a tetrahedron, and vice versa.[8] These materials exhibit substantial ionic character, even though the tetrahedral coordination is typical of sp^3 covalent bonding. [8] ZnO is most commonly found in the wurtzite phase, but it has also been observed in the zinc-blende phase in thin films and in the rocksalt phase under high-pressure conditions. The wurtzite structure has a hexagonal unit cell with two lattice parameters, *a* and *c*, as indicated in the nanowire segment oriented along the *c*-axis of the hexagonal wurtizte structure shown in Fig. 4-33., with an ideal ratio of $c/a = \sqrt{8/3} = 1.633$. In a real crystal, these parameters differ slightly from the ideal structure likely due to lattice stability, defects such as oxygen vacancies, and ionicity.[8] The lattice parameters typically range from 3.2475 to 3.2501 Å for the *a* parameter and from 5.2042 to 5.2075 Å for the *c* parameter.[8] In our calculations, *c* = 5.2 Å and *a* = 3.184 Å, yielding a c/a ratio of approximately 1.633. The bond-length between ZnO pairs is approximately 1.95 Å, which was calculated to be more energetically favorable for these structures within the LDA formalism.

Similar to other II-VI semiconductors, wurtzite ZnO can change into the rocksalt (NaCl) structure under high-pressure conditions. A segment of a ZnO nanowire in the rocksalt structure is shown in Fig. 4-33. The high-pressure phase transition from the wurtizte to the rocksalt structure decreases the lattice constant to the range of 4.271 Å to 4.294 Å.[8] From our first-principles calculations, a slightly smaller lattice constant of

4.13 Å proved energetically favorable. The reduction of lattice dimensions purportedly causes the interionic Coulomb interaction characteristic of ZnO to favor the ionic behavior over the covalent character. [8]

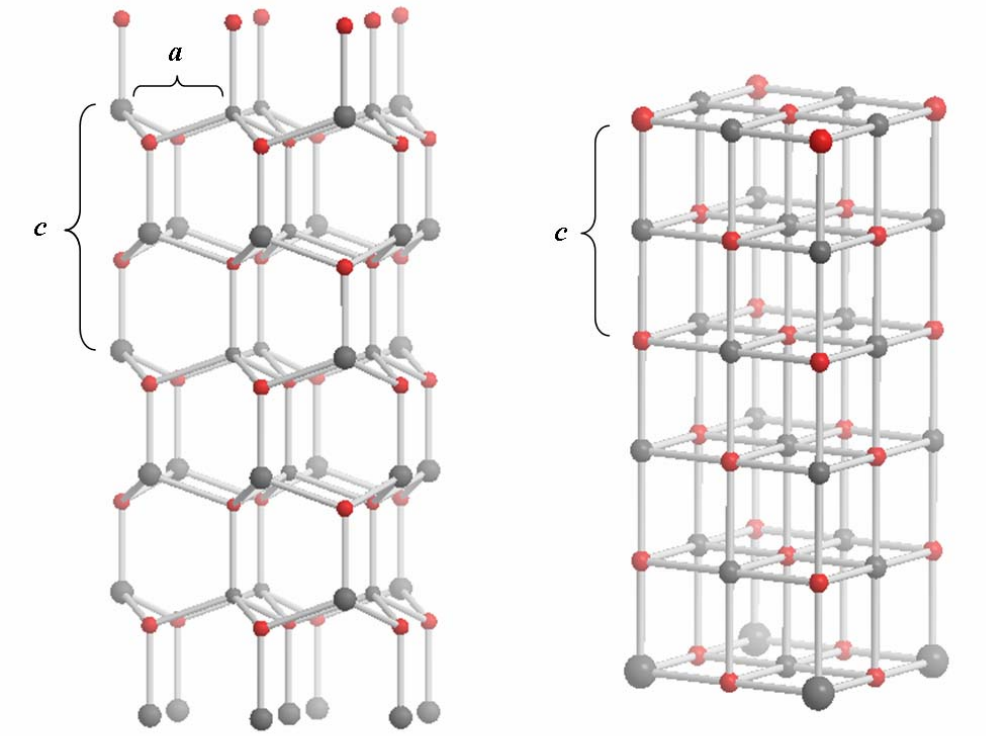

Figure 4-33. Ball and stick model of the ZnO wire segments constructed from the following bulk structures: (left) hexagonal wurtzite, and (right) rocksalt. In our calculations for wurtzite, c = 5.2 Å and a = 3.184 Å, yielding a c/a ratio of 1.633. For rocksalt, a lattice constant of c = 4.13 Å proved energetically favorable.

Ivanka Milošević and co-workers recently reported a theoretical study involving the symmetry of zinc oxide nanostructures.[107] In their work, they provided a rather elegant method of classifying various structures of zinc-oxide nanotubes made from bulk wurtzite-structures. A zinc-oxide bulk-like nanowire, distinct from the single-wall nanotubular structures discussed in the previous section, is essentially a wire structure with a core hollowed out of the center – thus representing a tube which preserves the periodicity along the *z*-axis of the bulk structure. The wurtzite configuration has two types of rotational axes along the z-direction: a third-order rotational axis which runs through the atoms and a sixth-order screw axis which goes through the centers of the hexagons formed by the atoms. Thus, according to the classification scheme proposed by Milošević et al. one may obtain two types of nanowires or nanotubes: 3H or 6H.[107]

We shall briefly discuss these classification schemes in relation to the structures that we have considered herein. The structures may be further classified as: 3xH, 3yH, 6xH, and 6yH. In our calculations, we consider structures of type 3yH and 6yH, shown in Figs. 4-34 through 4-37, respectively. A 3yH structure (Fig. 4-34) may be obtained by cutting the bulk structure along the planes perpendicular to $e_y = \boldsymbol{b}_1$ and along vectors successively rotated by $\pi/3$. The nanotube is parameterized as (n_1, n_2), where n_1 represents the line along the inner cut, and n_2 represents the line along the outer cut. For example, the structure illustrated in Fig. 4-36. is a (1,2) 3yH nanotube. Similarly, a 6yH structure is constructed by cutting along the bulk structure as indicated in Fig. 4-35. The 6H type nanotubes are characterized again by (n_1, n_2), but with $1 < n_1 < n_2$. As such, the structure shown in Fig. 4-37 is a (2,3) 6yH nanotube.

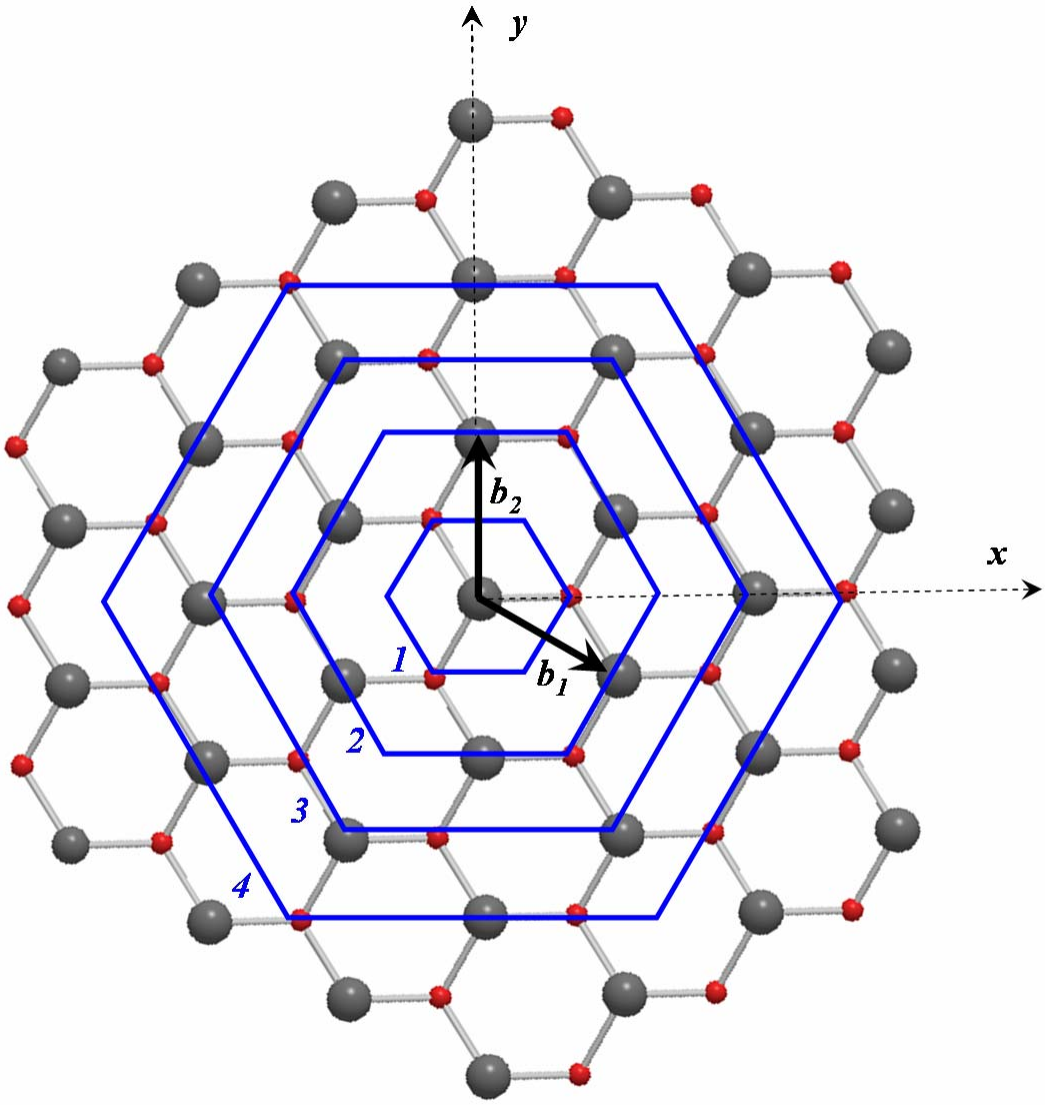

Figure 4-34. Schematic diagram illustrating nanotubes of the 3yH type.

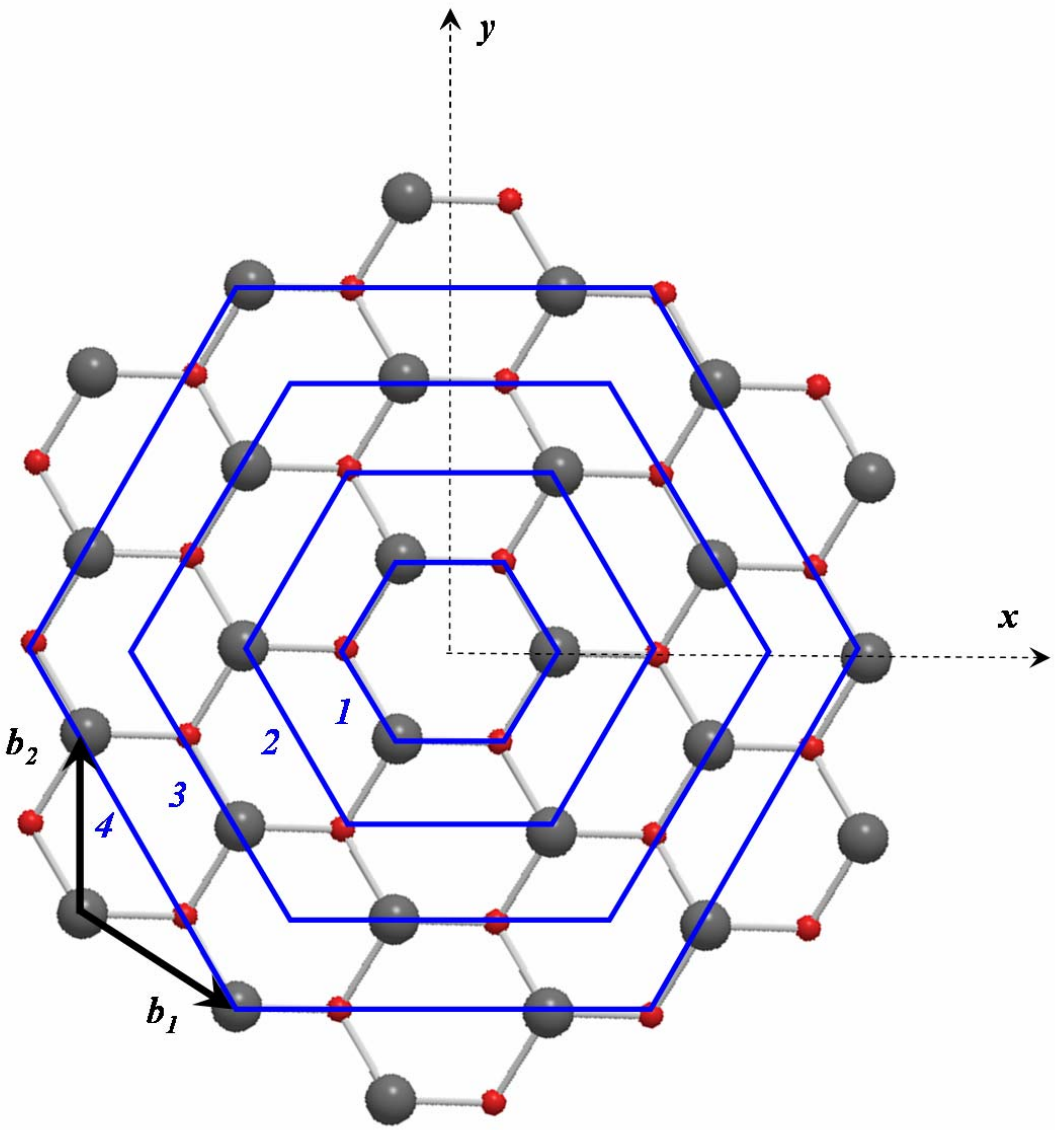

Figure 4-35. Schematic diagram illustrating nanotubes of the 6yH type.

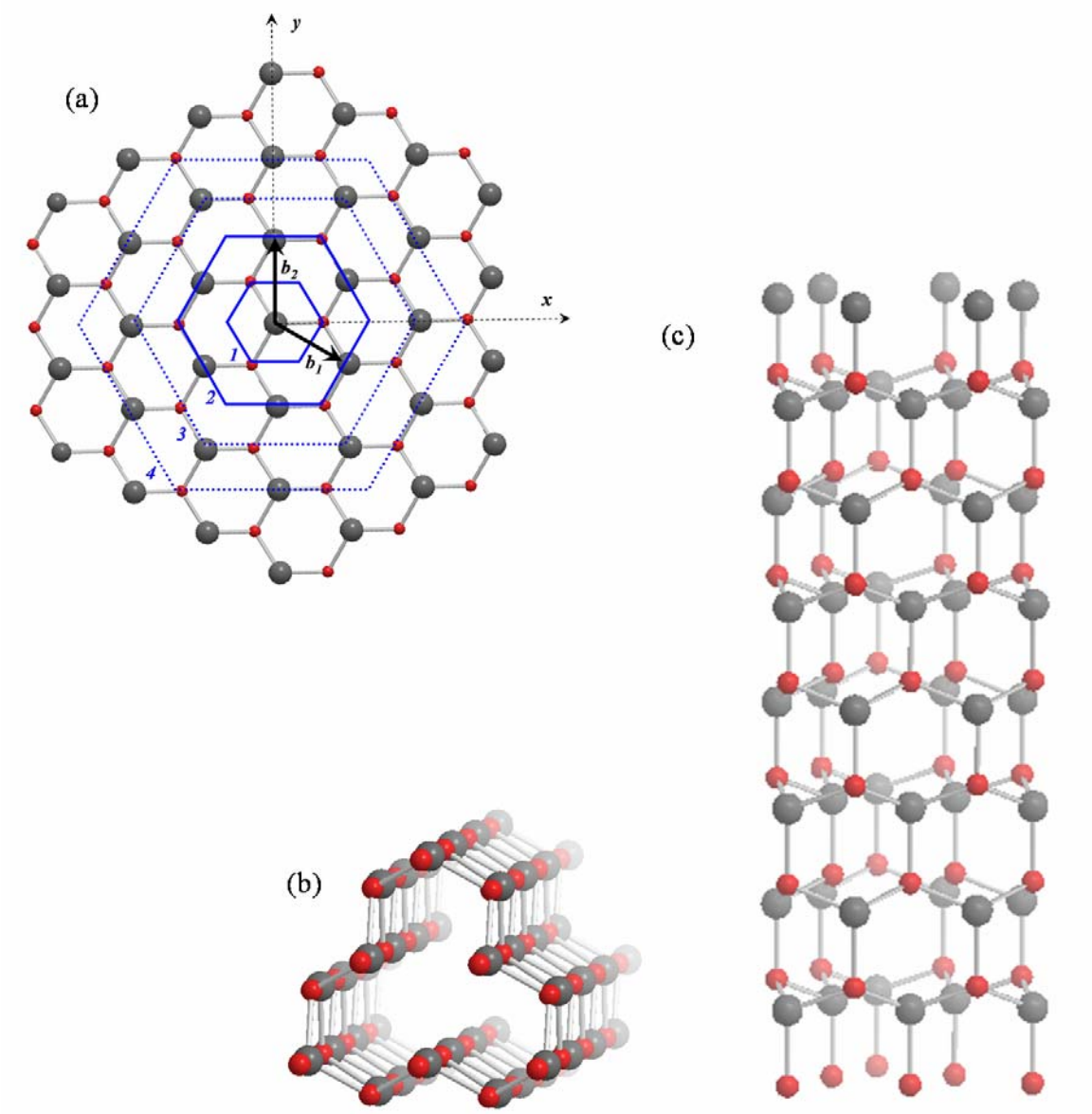

Figure 4-36. Models of the (1,2) 3yH ZnO nanotube. (a) Top view schematic of the construction from a bulk-wire, (b) perspective view down the z-axis of the nanotube, (c) side view of the nanotube structure.

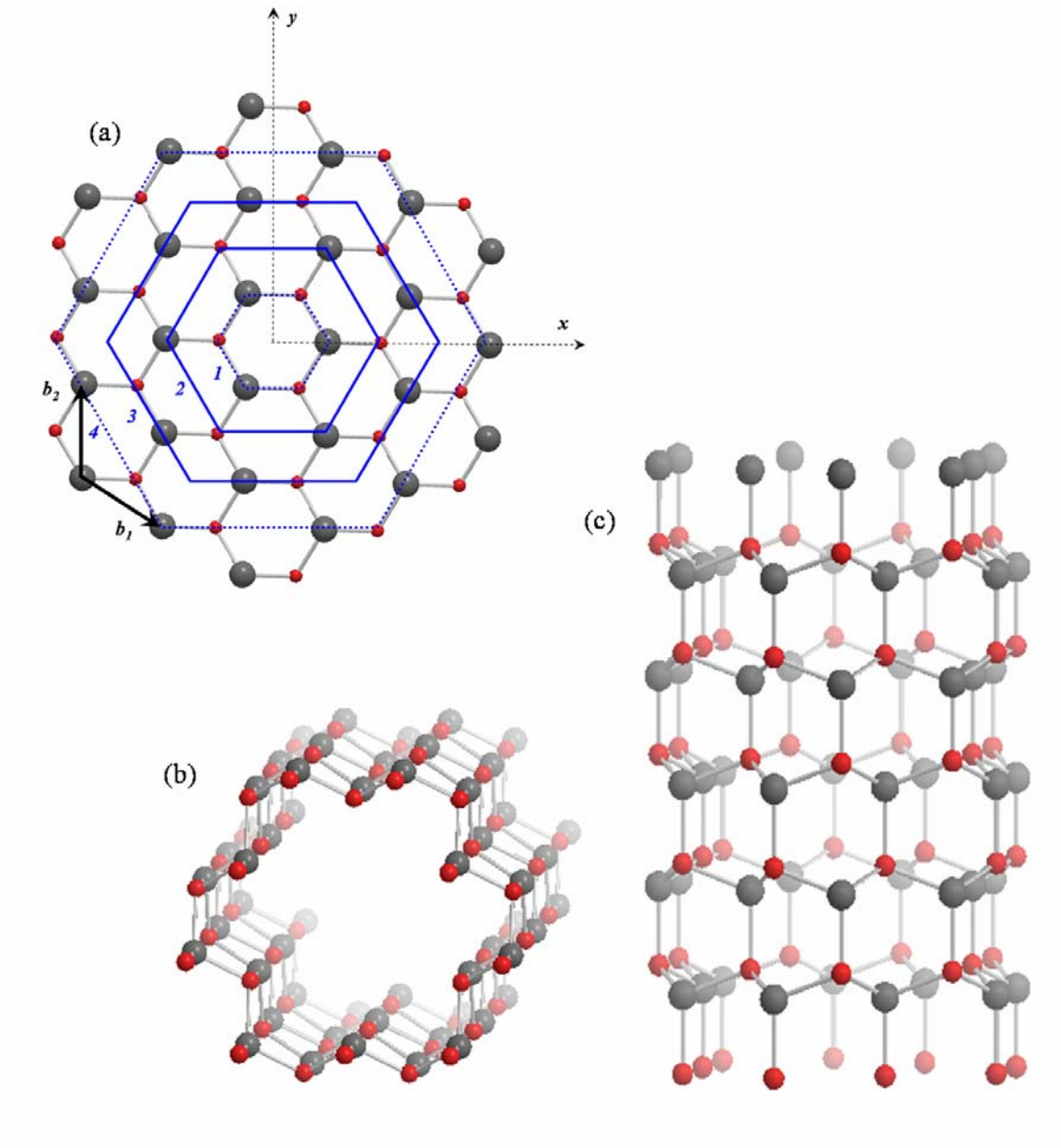

Figure 4-37. Models of the (2,3) 6yH ZnO nanotube. (a) Top view schematic of the construction from a bulk-wire, (b) perspective view down the z-axis of the nanotube, (c) side view of the nanotube structure.

4.4.3 Energetic Results

For ZnO in bulk geometrical configurations, the total energy is most energetically favorable for hexagonal wurtzite, with zinc blende closely related and rocksalt the least energetically favorable.[8] As the dimensionality of these systems decrease, the bulk-like characteristics do not necessarily hold true. In our calculations, for the ultrathin nanowire configurations, the wurtzite structure with a radius of approximately 3.5 Å had a total energy per ZnO pair of -1847.7239 Hartrees, while the total energy per ZnO pair for the rocksalt structure with a radius of approximately 3.0 Å was -1847.7243 Hartrees per ZnO pair.

The bulk-like nanotubes were much higher in total energy than both the bulk-like nanowires and the graphitic-like single-wall nanotubes. Upon comparing the bulk-like nanotubes, the (1,2) 3yH ZnO nanotube, with a radius of approximately 3.5 Å, has a slightly lower total energy per ZnO pair of -1847.7059 Hartrees, in comparison to the (2,3) 6yH ZnO nanotube, with a radius of approximately 5 Å, has a total energy per ZnO pair of -1847.7051 Hartrees. The results of the total energies are presented in Table X and plotted in Fig. 4-38 with respect to radii. The energetic results are more dependent on structure than radii, i.e. the total energies are lower for the nanowires than the nanotubes, but a clear trend is not present with respect to structure radii.

Structure	Radius (Å)	Total Energy (Hartrees per ZnO Pair)
Nanowires		
Hexagonal Wurtzite Nanowire	3.5	-1847.7239
Rocksalt Nanowire	3.0	-1847.7243
Nanotubes		
(1,2) 3yH (Hexagonal Wurtzite)	3.5	-1847.7059
(2,3) 6yH (Hexagonal Wurtzite)	5.0	-1847.7051
Rocksalt	3.0	-1847.7084

Table VI. Total energies of the ZnO Bulk-like nanotubes and nanowires.

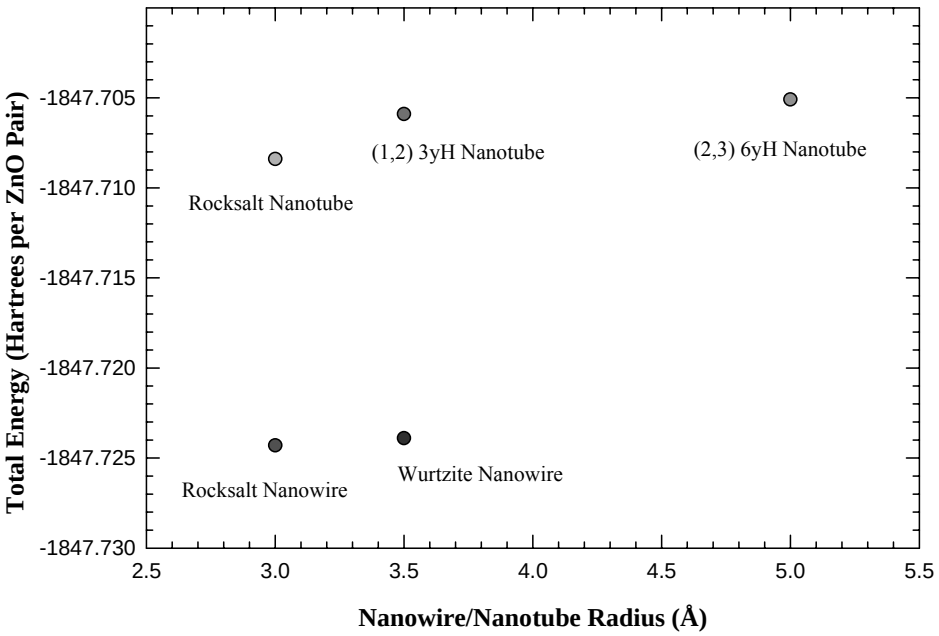

Figure 4-38. Total energies of the ZnO Bulk-like nanotubes and nanowires versus radius.

Results from the Mulliken population analysis of the hexagonal wurtzite and rocksalt nanowires are shown as follows, with charges on Zinc (gray) and Oxygen (red) atoms indicated in units of *e*. In general, for the hexagonal wurtzite wire (Fig. 4-39), the charges on Zn along the outer perimeter of the wire range from +.6443*e* to +.6639*e*, and the charges for oxygen atoms lying along the outer perimeter range from -.6518*e* to -.6443*e*. The charges associated with the central ZnO atom pair and the atoms bonded directly to the central atoms exhibit a slightly different behavior. The charge on the central Zn atom is only +.4529*e*, while the charge on the central O atom is -.7255*e*. The remaining three Zn atoms which are bonded to the central O atom have charges of +.8044*e*, while the remaining three oxygen atoms which (which when translated periodically) bond to the central Zn atom have charges of -.7383*e*. The change in atomic population versus the radial distance from the atom position and (*x*,*y*) origin of the wurtzite nanowire is displayed graphically in Fig 4-41.

Results from the Mulliken population analysis for the (1,2) 3yH and (2,3) 6yH Wurtzite Nanotubes are shown in Figs. 4-40 and 4-42, with charges on Zinc (gray) and Oxygen (red) atoms indicated in units of *e*. Figs. 4-41 and 4-43. display the change in atomic population versus the radial distance from the atomic positions and (*x*,*y*) origin of the (1,2) 3yH and (2,3) 6yH Nanotubes, respectively.

For the (1,2) 3yH Nanotube, the atoms are located at three incremental distances from the origin of the nanotube. The Zinc atoms located closest to the origin and furthest away from the origin have the greatest positive charge (+.75*e*), while the Zinc atoms located mid-distance have the least atomic charge (+.62*e*). The Oxygen atoms located on

the outer-edge of the nanotube exhibit slightly more negative charge (-.70*e*) than the Oxygen atoms located closest to the nanotube origin (+-.68*e*) and at mid-distance (-.66*e*) from the origin.

For the (2,3) 6yH Nanotube, the atoms are located at two incremental distances from the origin of the nanotube. The Zinc atoms located at the distance furthest from the origin have a more positive atomic charge (+.71*e*) than the Zinc atoms located closer (+.53*e*) to the origin of the nanotube. The Oxygen atoms possess a similar degree of negative charge (-.65*e*) independent of their distances from the nanotube origin.

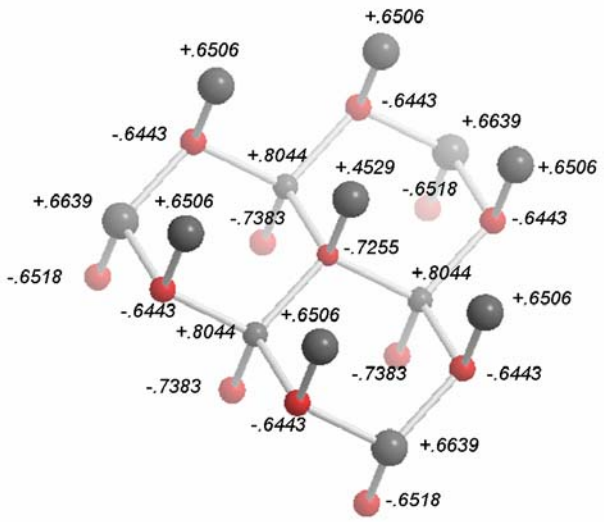

Figure 4-39. Ball and stick model of the unit cell for the wurtzite structure ZnO wire. Charges associated with the Mulliken population analysis are indicated in units of *e*.

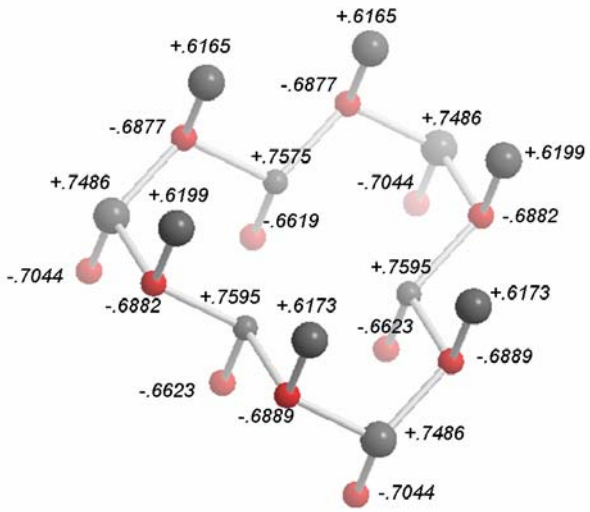

Figure 4-40. Ball and stick model of the unit cell for the (1,2) 3yH ZnO nanotube. Charges associated with the Mulliken population analysis are indicated in units of *e*.

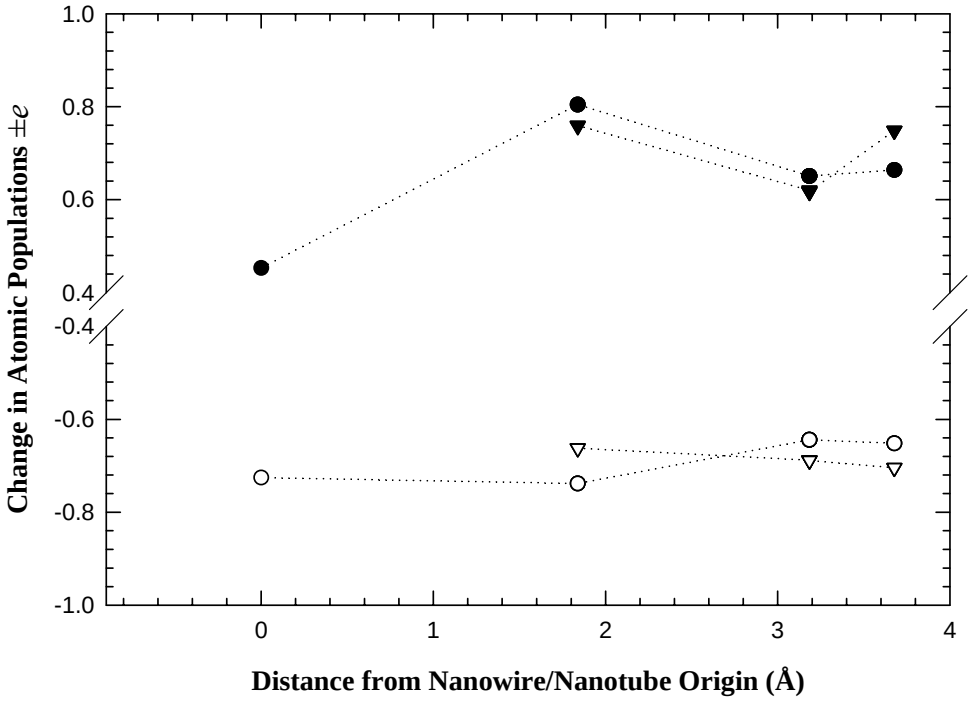

Figure 4-41. Change in atomic populations versus distance from nanowire/nanotube origin for Zn (●, ▼) and O (○, ▽) atoms in the hexagonal wurtzite nanowire and the (1,2) 3yH nanotube, respectively.

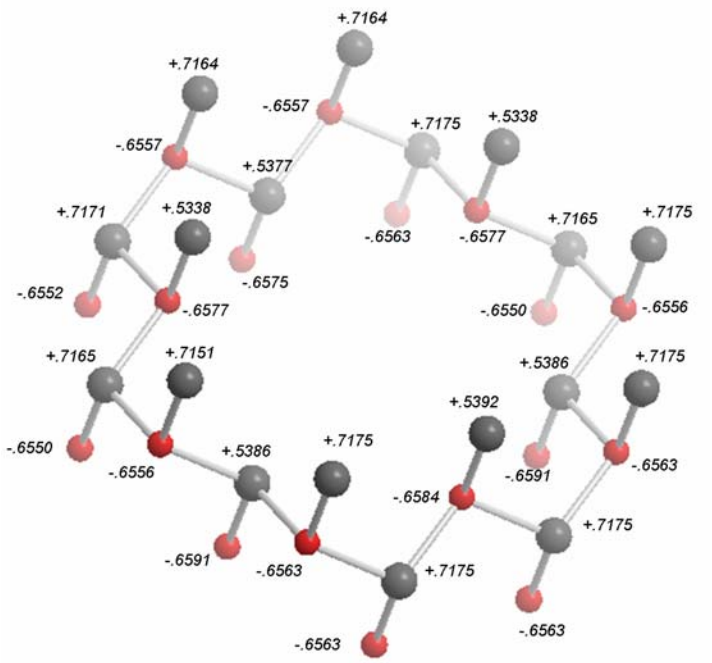

Figure 4-42. Ball and stick model of the unit cell for the (2,3) 6yH ZnO nanotube. Charges associated with the Mulliken population analysis are indicated in units of *e*.

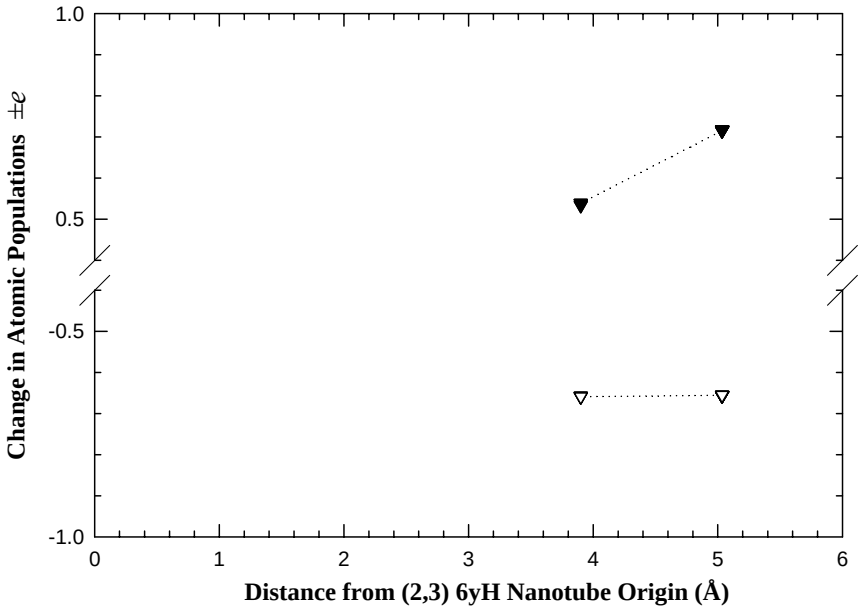

Figure 4-43. Change in atomic populations versus distance from nanotube origin for Zn (▼) and O (∇) atoms in the (2,3) 6yH ZnO nanotube.

For the rocksalt wire, shown in Fig. 4.44., the central ZnO atom pair also exhibit different charges in comparison to the atoms along the outer perimeter of the wire. For rocksalt, the central Zn atom has a charge of +1.0478*e*, while the O atom has a charge of -.7437*e*. In comparison, the Zn atoms lying furthest away from the core of the wire have charges ranging from +.5866*e* to +.5917*e*, and the O atoms lying furthest away from the core have charges ranging from -.6292*e* to -.6315*e*. Fig x. exhibits the change in atomic population versus the radial distance from the atom position and (*x*,*y*) origin of the rocksalt nanowire.

For the rocksalt nanotube (Fig. 4-45), the excess charge of +1.0478e previously located on the central Zn atom in the wire, is disbursed to the outer Zn atoms of the nanotube increasing their charges by +.2*e* in comparison to the rocksalt nanowire. In contrast, the Zn atoms located closer to the core have lost .1*e* in charge.

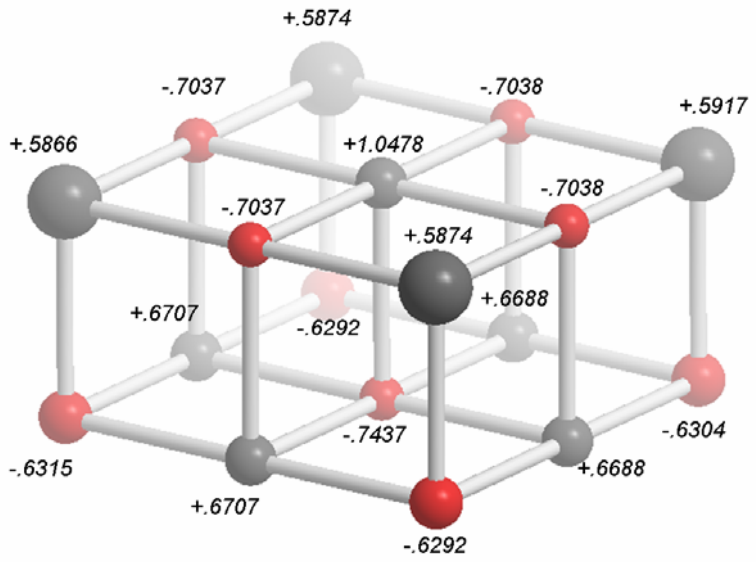

Figure 4-44. Ball and stick model of the unit cell for the rocksalt structure ZnO wire. Charges associated with the Mulliken population analysis are indicated in units of *e*.

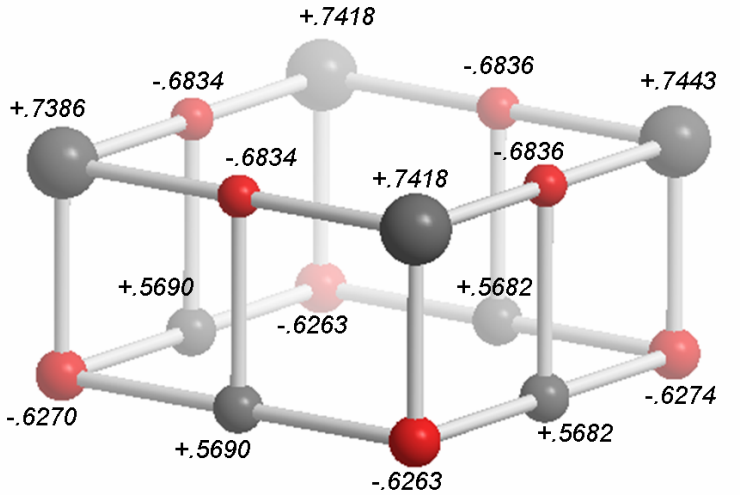

Figure 4-45. Ball and stick model of the unit cell for the rocksalt structure ZnO tube. Charges associated with the Mulliken population analysis are indicated in units of *e*.

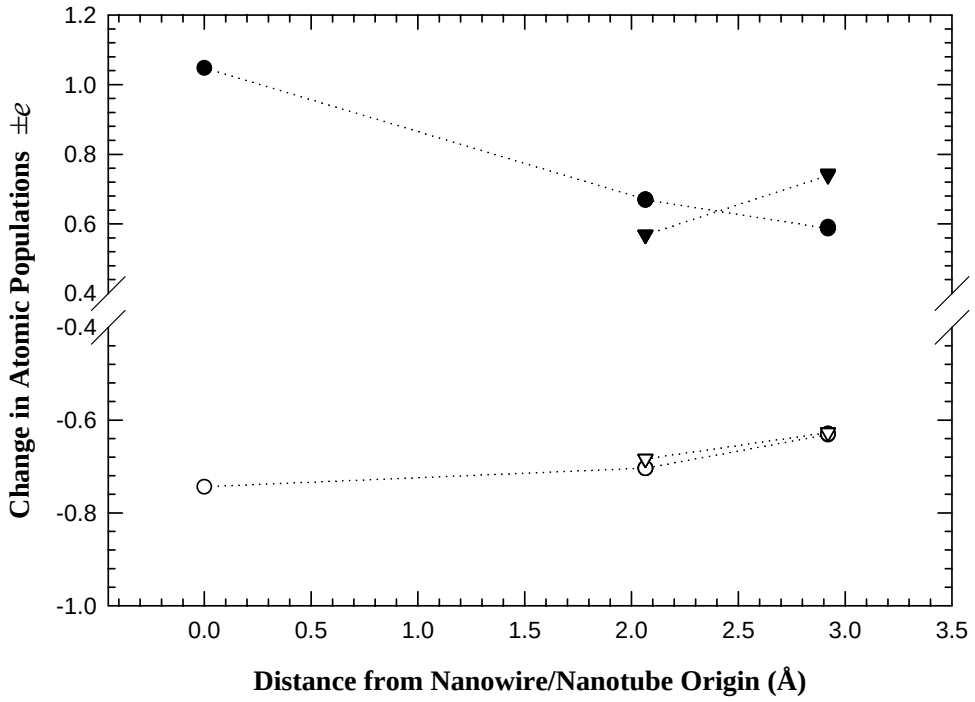

Figure 4-46. Change in atomic populations versus distance from nanowire/nanotube origin for Zn (▼) and O (∇) atoms in the rocksalt nanowire and nanotube.

4.4.4 Band Structures and Densities of States

The first-principles band structures and densities of states for the hexagonal wurtzite and rocksalt nanowires and nanotubes are shown in Figs. 4-47 through 4-51. Although their band structures and densities of states exhibit similar characteristics, the rocksalt band structure displays an interesting result, as there is no longer a direct band gap.

The first-principles band structures and densities of states for the wurtzite nanowire, the (1,2) 3yH ZnO and the (2,3) 6yH ZnO nanotubes are shown in Figs. 4-47 through 4-49, respectively. The difference between the lowest unoccupied conduction band and the highest occupied valence band at the Γ point is 0.8073 eV for the hexagonal wurtzite nanowire, while it shifts to 0.5672 eV and 0.8052 eV for the (1,2) 3yH and the (2,3) 6yH nanotubes, respectively. The band structures and densities of states for the rocksalt nanowire and nanotube are shown in Figs. 4-50 and 4-51, respectively.

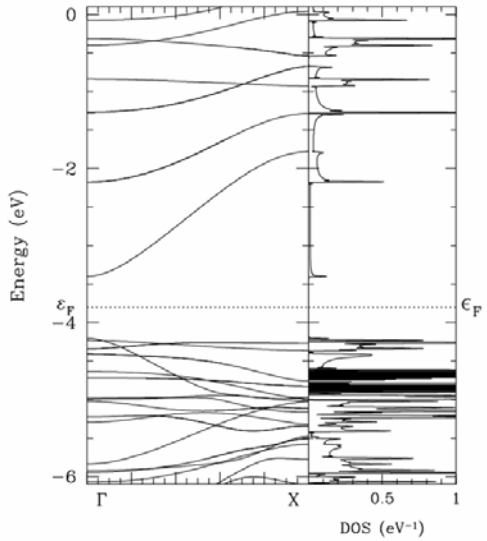

Figure 4-47. Band structure and density of states for the hexagonal wurtzite ZnO nanowire. The Fermi level is indicated at -3.8041 eV.

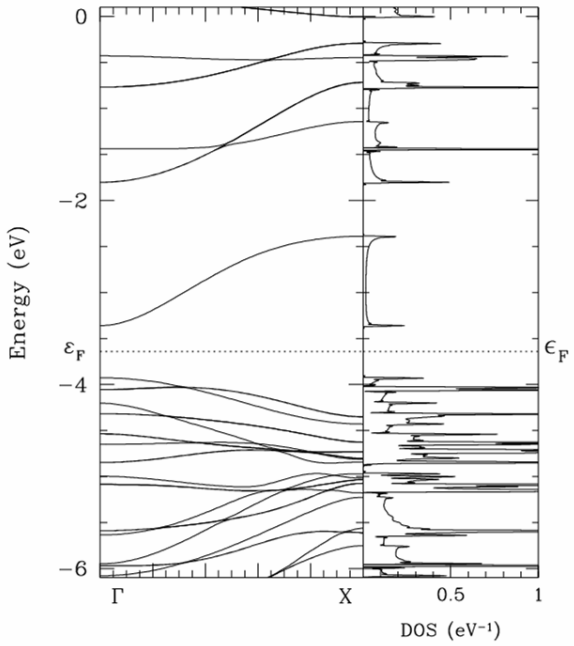

Figure 4-48. Band structure and density of states for the (1,2) 3yH ZnO nanotube. The Fermi level is indicated by the dashed line at -3.6432 eV.

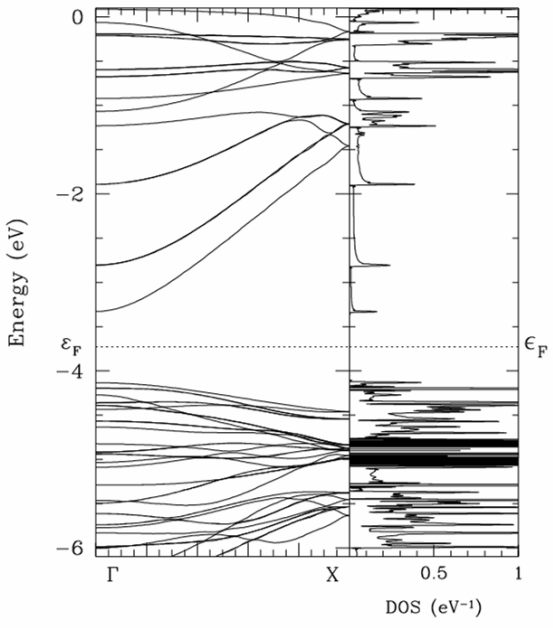

Figure 4-49. Band structure and density of states for the (2,3) 6yH ZnO nanotube. The Fermi level is indicated by the dashed line at -3.7307 eV.

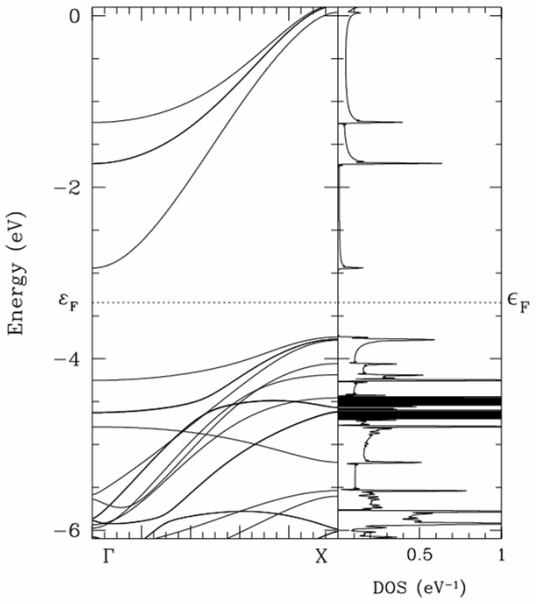

Figure 4-50. Band structure and density of states for the rocksalt ZnO nanowire. The Fermi level is indicated at -3.3446 eV.

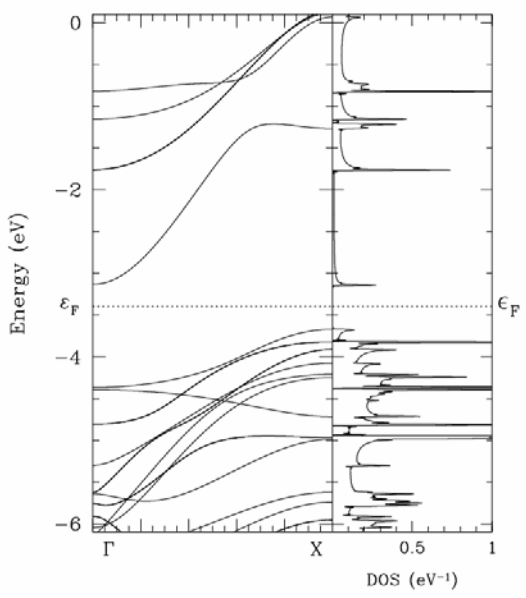

Figure 4-51. Band structure and density of states for a rocksalt ZnO nanotube. The Fermi level is indicated by the dashed line at -3.4004 eV.

4.4.5 Optical Absorption Spectra

The optical spectra for the hexagonal wurtzite ZnO nanostructures and rocksalt nanostructures are given in Figs. 4-52 to 4-54, respectively. The absorption peak energies of the wurtzite and rocksalt structures are very different due to the indirect band gap calculated in the rocksalt band structure. Qualitatively, however, the absorption spectra are similar as they are both dominated by direct transitions due to parallel excitations.

For the hexagonal wurtzite nanowire (Fig. 4-52), the first allowed transition due to parallel excitations is located at 0.82 eV. The optical spectra for the (1,2) 3yH nanotube given in Fig. 4-52. undergoes only minor changes upon transitioning from the nanowire to the nanotube structure. In comparison the absorption spectra of the (2,3) 6yH larger bulk-like nanotube (Fig.4-53) is relatively different, as the peaks associated with parallel transitions are much closer to each other in the larger nanotube.

The optical spectra for the rocksalt nanotube and nanowire are given in Fig. 4-54. In the rocksalt nanowire, the first peak associated with a direct transition is at 2.58 eV, while the first peak in the nanotube is shifted lower in energy, to 2.18 eV. The second peak associated with the nanotube is also now further apart and higher in intensity. Specifically, the difference between the first two allowed parallel transitions in the nanowire is 0.17 eV, while the difference between the same peaks in the nanotube is twice as much at 0.34 eV.

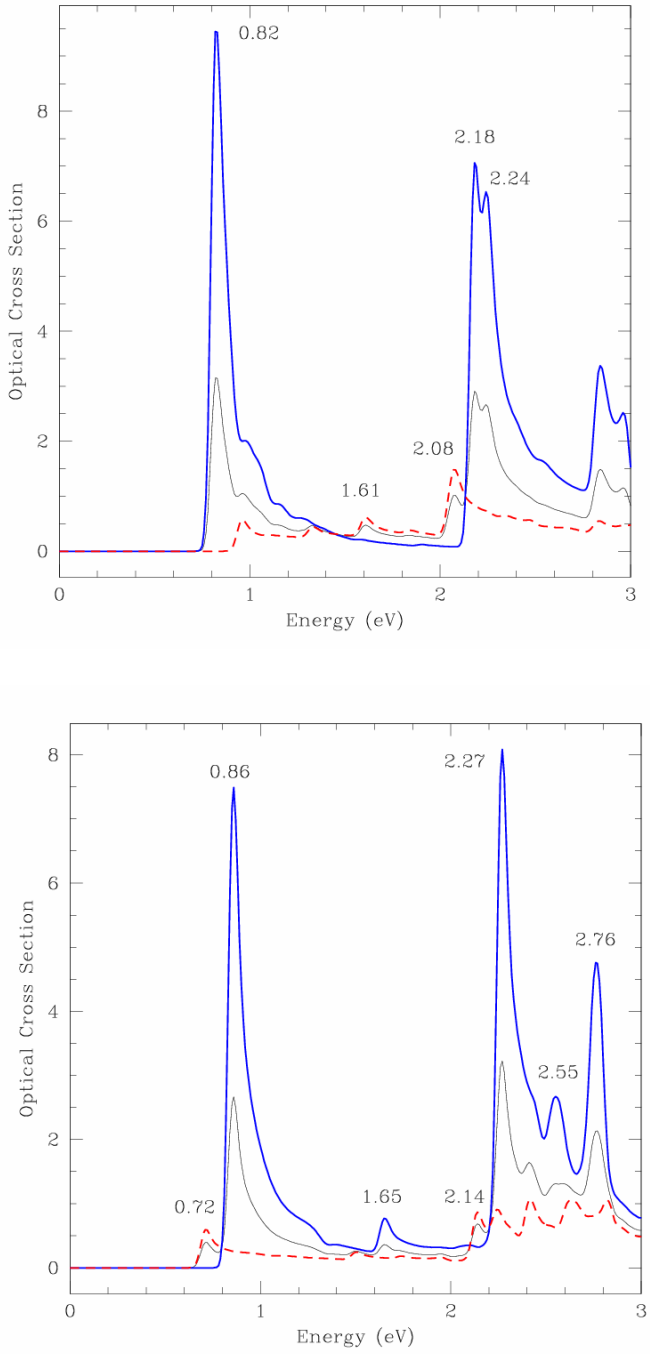

Figure 4-52. Optical absorption spectra for a (upper) hexagonal wurtzite ZnO nanowire and (lower) the (1,2) 3yH nanotube. Solid blue lines represent peaks corresponding to parallel polarizations, dashed red lines represent peaks corresponding to perpendicular polarizations, and black solid lines represent the total spectra.

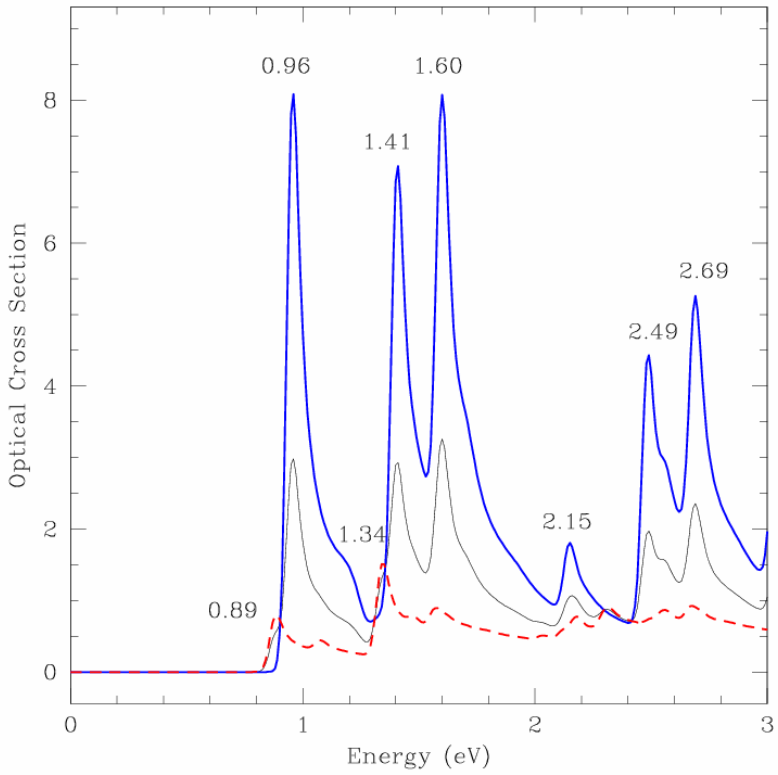

Figure 4-53. Optical absorption spectra for the (2,3) 6yH ZnO nanotube. Solid blue lines represent peaks corresponding to parallel polarizations, dashed red lines represent peaks corresponding to perpendicular polarizations, and black solid lines represent the total spectra.

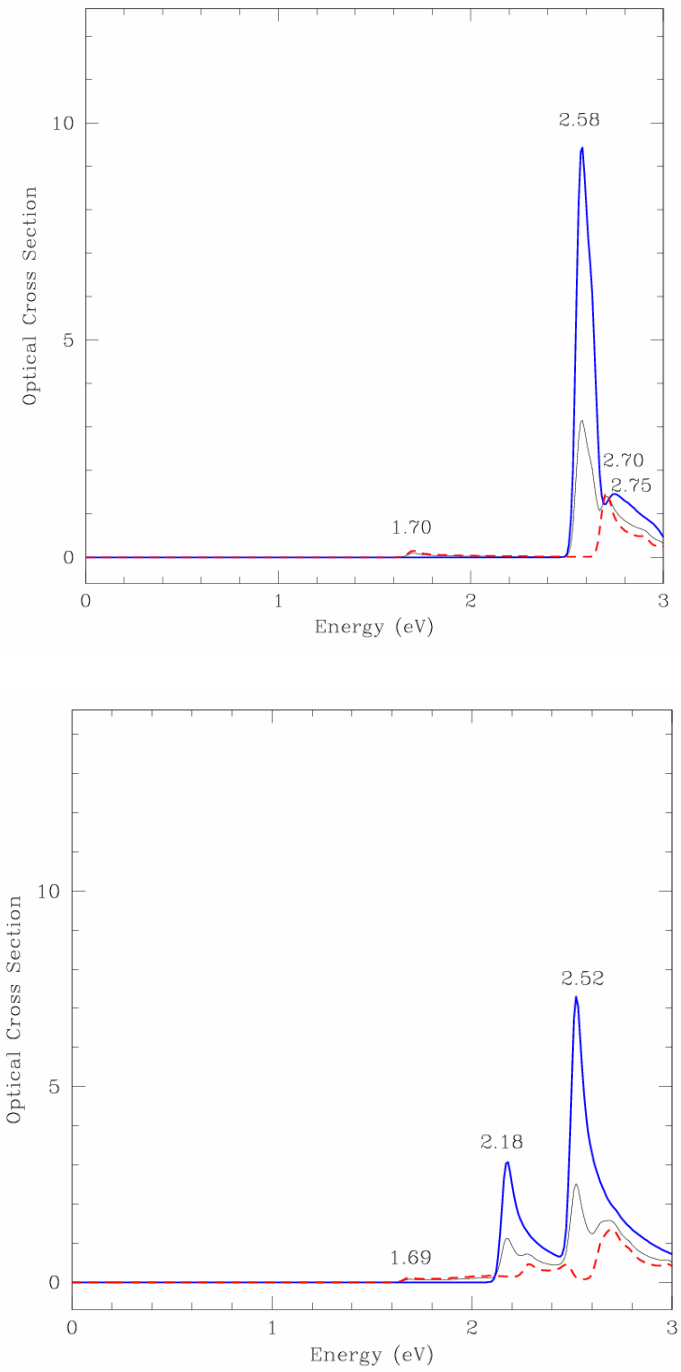

Figure 4-54. Optical absorption spectra for a rocksalt (top) ZnO nanowire and (bottom) nanotube. Solid blue lines represent peaks corresponding to parallel polarizations, dashed red lines represent peaks corresponding to perpendicular polarizations, and black solid lines represent the total spectra.

The results associated with the first two parallel excitations for the bulk-like ZnO nanowires and nanotubes are displayed numerically in Table VII. Due to the indirect bandgap associated with the rocksalt structure, it is difficult to compare the results with the wurtzite nanowires and nanotubes. While the locations of the peaks associated with the first and second allowed parallel transitions for the wurtzite nanotubes do not exhibit a trend versus radius, the difference between the two peaks does exhibit a trend: as the nanotube radius increases from 3.5 Å in the (1,2) 3yH structure to 5.0 Å in the (2,3) 6yH structure, the first two peaks become closer together. The difference between the first two peaks decreases from 0.79 eV for the smaller (1,2) 3yH nanotube to 0.45 eV for the larger (2,3) 6yH nanotube.

Structure	**Radius (Å)**	**E_1 (eV)**	**E_2 (eV)**	**(E_2-E_1) (eV)**
Nanowires				
Hexagonal Wurtzite Nanowire	3.5	0.82	2.18	1.36
Rocksalt Nanowire	3.0	2.58	2.75	.17
Nanotubes				
(1,2) 3yH (Hexagonal Wurtzite)	3.5	0.86	1.65	0.79
(2,3) 6yH (Hexagonal Wurtzite)	5.0	0.96	1.41	0.45
Rocksalt	3.0	2.18	2.52	0.34

Table VII. Energies for the first two optical absorption peaks corresponding to parallel excitations for the ZnO bulk-like nanowires and nanotubes.

4.4.6 Summary of Results

Using our first-principles LDF approach, we studied ultrathin bulk-like ZnO nanowires and nanotubes. Hexagonal wurtzite and rocksalt nanowires were considered, as well as bulk-like nanotubes constructed from the wire structures. We now summarize the results obtained for these structures. Further discussion in the next section highlights similarities and differences between these bulk-like 1D structures and the single-wall nanotubes studied in the previous chapter.

Not surprisingly, the solid nanowire structures were approximately 0.5 eV lower in total energy than the hollow nanotube structures for both wurtzite and rocksalt configurations. Within each structure (i.e. nanowire or nanotube), however, systems with rocksalt geometry were somewhat energetically more favorable than the corresponding wurtzite structures. For example, the rocksalt nanowire was roughly .01 eV lower in energy than the hexagonal wurtzite nanowire. These results are somewhat in contrast to what we expected because in bulk configurations wurtzite is clearly more energetically favorable. In our case, since the energies differences are so small, it is difficult to conclude if the rocksalt structures are preferable over the wurtzite structures for 1D geometries.

The Mulliken populations of these structures were also analyzed. The most appreciable differences were with respect to the wurtzite and rocksalt nanowires. While the Zn and O atom pair in the rocksalt structure had atomic populations of +0.4529*e* and -0.7255*e*, respectively, the Zn and O atom pair in the rocksalt structure had atomic populations of +1.0478*e* and -0.7437*e*, respectively. Upon removing the central ZnO

atom pair for both wurtzite and rocksalt wires, thus forming a tube, the outer Zn atoms became more positively charged by at least 0.1e. The outer O atoms in the wurtzite structure became proportionally more negatively charged, while the outer O atoms in the rocksalt structure remained relatively unchanged.

While the band structures were similar within all wurtzite structures and all types of rocksalt structures, respectively, the wurtzite structure exhibited a direct band gap, while the rocksalt structures displayed an indirect band gap. The tight-binding bands were also qualitatively similar to the first principles results, although the magnitudes of the band gaps were quantitatively larger.

Although all structures were dominated by peaks due to parallel polarizations, the optical absorption spectra varied from structure to structure. Due to the indirect band gap present in the rocksalt structure, the presence of the first allowed parallel peak associated with a direct transition was shifted on the order of 1.5 eV higher in energy. For the wurtizite structures, the (2,3) 6yH nanotube with the larger radius exhibited a blue-shifting of the second allowed optical absorption peak arising from parallel polarization. This result is similar to the findings in the single-wall nanotubes; as nanotube radius increased, the second peak occurred at relatively lower energies.

4.5 Assessment of Results: Single-Wall Nanotubes vs. Bulk-Like 1D Structures

The energetic results for the single-wall nanotubes and bulk-like nanotubes and nanowires are summarized in Table VIII. The total energies of the graphitic-like single-wall nanotubes range from -1847.7317 to -1847.7136 Hartrees per ZnO pair, an energy range of approximately 0.5 eV. The bulk-like nanotubes are the least energetically favorable, roughly 0.25 eV higher in energy than the upper range of the single-wall nanotubes. The total energies of the nanowires were within the range of the single-wall graphitic-like nanotubes. The band gaps of the graphitic-like single-wall nanotubes were approximately 1.10 eV, while the bulk-like structures ranged from 0.5 eV to 0.8 eV.

ZnO Structure	**Total Energy (Hartrees/ ZnO)**	**Band Gap (eV)**
Single-Wall Nanotubes		
Graphitic-Like	-1847.7317 to -1847.7136	1.08-1.14
Bulk-Like:		
(1,2) 3yH	-1847.7059	.5672
(2,3) 6yH	-1847.7051	.8052
Rocksalt	-1847.7084	.8039*
Nanowires:		
Wurtzite	-1847.7239	.8073
Rocksalt	-1847.7243	.5302*

Table VIII. Total energies and band gaps of all ZnO nanotube and nanowire structures considered. (*) Denotes an indirect band gap.

4.6 A Comparative Analysis with NRL/OSU POLYXA and Crystal 03

4.6.1 Overview

The NRL/OSU POLYXA code calculates the electronic structures for 1D materials. Different program packages can be utilized in order to model materials in 2D and 3D. For comparison, we chose to employ Crystal03 which has the capabilities of modeling structures in 0D, 1D, 2D, and 3D. Although crystal symmetry is taken into account by Crystal03, only translational periodicity is implemented, thus limiting the 1D structures that we can model using a reasonable unit cell size. Crystal03 proved useful for modeling structures in higher dimensions, and it demonstrated comparable behavior to POLYXA when it came to modeling the single-wall ZnO nanotubes, described in detail in section *4.6.4*.

Using Crystal03, we modeled the following ZnO structures within the context of LDA: the 3D hexagonal wurtzite bulk form, a 2D sheet with a graphitic monolayer structure, and the (4,4) ZnOSWNT, the only common structure taken into account using both programming packages. Although comparable, the results for the SWNT were not exactly the same, thus we address some discrepancies within the results. As a final step, utilizing POLYXA, we calculate 1D ZnO graphitic-like strips and estimate the expected energy for the 2D sheet.

4.6.2 Hexagonal Wurtzite in 3D

As stated previously, the lattice parameters for ZnO in the hexagonal wurtzite crystal structure typically range from 3.2475 to 3.2501 Å for the *a* parameter and from 5.2042 to 5.2075 Å for the *c* parameter.[8] In our hexagonal wurtzite wire calculations *c* = 5.2 Å and *a* = 3.184 Å, yielding a c/a ratio of approximately 1.633. Here, for the bulk calculation using CRYSTAL03, we considered a small range of parameters from Ref. 14, and we found the values that we used (*c* = 5.2 Å and *a* = 3.184 Å) in our wire calculations were also more energetically favorable for the 3D hexagonal wurtzite model.

The calculated results obtained with Crystal03 [11] are summarized in Table IX along with selected results from the literature for comparison. Within the LDA approximation we obtain a total energy of -1847.7496 Hartrees per ZnO pair, and we calculate the band gap energy to be 0.82 eV. We find our band gap of 0.82 eV within the LDA approximation to be consistent with what others have obtained. Figure 4-55 illustrates the first Brillioun zone for a hexagonal wurtzite crystal. The band structure generated with Crystal03 is shown in Fig. 4-56.

Theory	*Band Gap (eV)*
Current Study:	
LDA	0.82
From Literature:	
LDA [108]	0.74
GGA [108]	0.80
LDA-PP [8, 109]	0.23
LDA-SIC-PP [8, 109]	3.77

Table IX. Energetic results obtained in this study using Crystal03 [11] along with selected results from literature for ZnO in the bulk hexagonal wurtzite structure. GGA, generalized gradient approximation; LDA-PP, local-density approximation pseudopotential; LDA-SIC-PP, local-density approximation self-interaction-corrected pseudopotential [8, 109] .

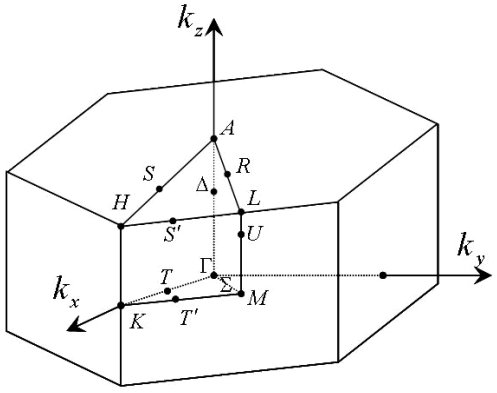

Figure 4-55. First Brillioun Zone of the hexagonal wurtzite crystal structure.

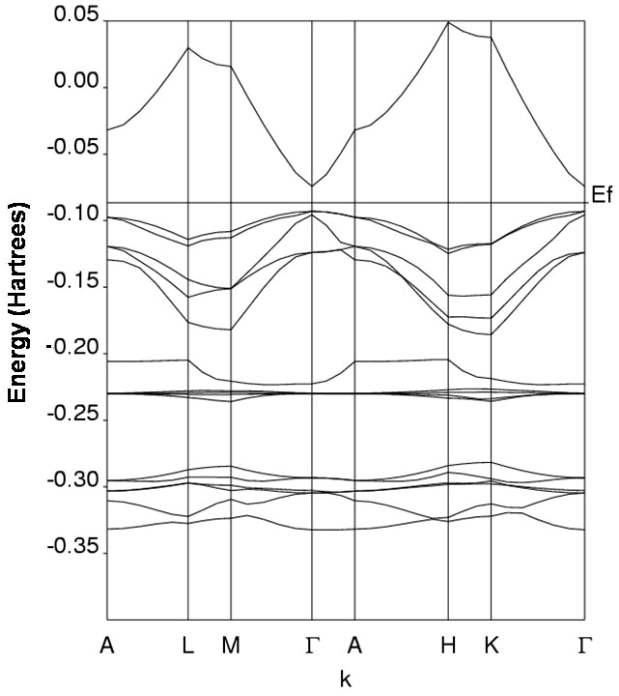

Figure 4-56. Energy bands of ZnO in the hexagonal wurtzite crystal structure within the LDA approximation obtained using Crystal03 [11].

4.6.3 ZnO in a 2D Graphitc-Like Sheet

As mentioned previously, Claeyssens et al. calculated a new energetically favorable 'graphitic'-like structure for ZnO thin films (< 10 layers). [27] Because the single-wall ZnO nanotubes studied in section xx. are essentially a rolled-up sheet of ZnO in a graphitic-like geometrical configuration, we are interested in determining the strain energy for the single-wall nanotube as a result of rolling up the sheet. Herein, using Crystal03, we evaluate the total energy and band structure for ZnO in a 2D graphitic-like geometrical configuration illustrated in Fig. 4-57.

The band structure generated with Crystal03 is given in Fig. 4-58. The total energy within the LDA approximation is -1847.7234 Hartrees per ZnO pair, with a band gap of approximately 1.20 eV. The total energy of the 2D sheet is 0.0262 Hartrees (~ 0.7129 eV) higher in energy than the 3D hexagonal wurtzite structure. It is comparable with our results for the single-wall nanotubes, but we would expect the sheet energy to be lower in energy than the single-wall nanotubes (i.e. less than -1847.73 Hartrees), which is not the case using Crystal03. Therefore, in the following section, we compare our results using POLYXA for the (4,4) ZnO SWNT to the results obtained using CRYSTAL03.

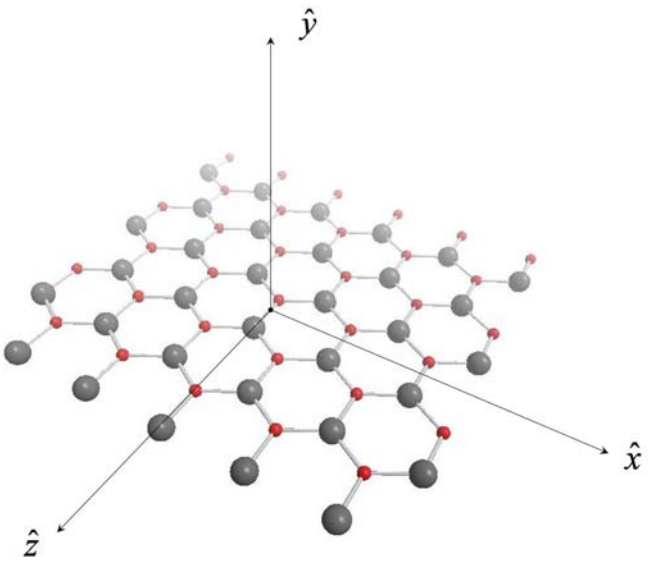

Figure 4-57. Ball and stick model of a 2D ZnO sheet in a graphitic structure. The sheet is periodic along the *x* and *z* – axes.

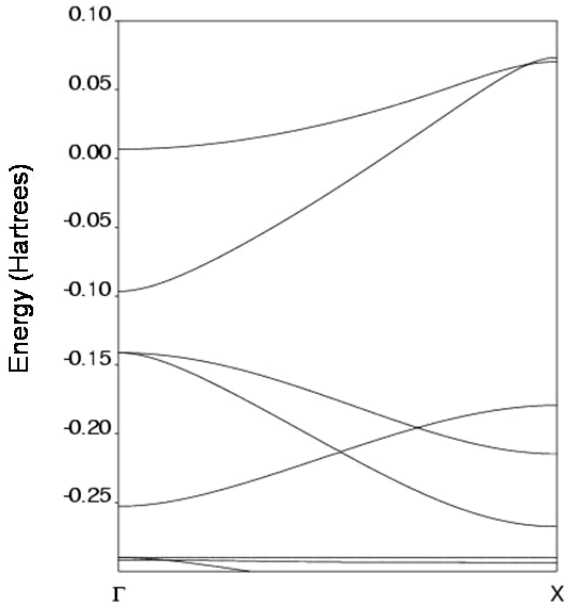

Figure 4-58. Energy bands of ZnO in a 2D graphitic-like structure within the LDA approximation obtained using CRYSTAL03 [11].

4.6.4 The (4,4) ZnOSWNT Revisited

Can we accurately compare our results using POLYXA with results obtained using CRYSTAL03? Our choice of 1D systems using CRYSTAL03 (with translational symmetry) was very limited due to chirality and symmetry constraints. The achiral ZnOSWNTs have either C_{nv} or C_n type symmetry, and CRYSTAL03 has such symmetries available through C_{4v}. Therefore, we chose to model the (4,4) ZnO SWNT.

The energy obtained for the (4,4) ZnOSWNT using CRYSTAL03 within the LDA approximation was -1847.7227 Hartrees per ZnO pair. The energy was quite comparable to the value obtained with POLYXA: -1847.7250 Hartrees per ZnO pair. Through further investigation, we determined the exact numerical deviation to be most likely attributed to numerical variations arising from grid differences. Upon adjusting the grid for POLYXA, the total energy varied from -1847.7221 to -1847.7279 Hartrees per ZnO pair, a variation on the order of ± 0.003 Hartrees.

The band structures for the (4,4) ZnO SWNT are shown in Fig. 4-59; the bands obtained using POLYXA are shown in (a), the bands generated with CRYSTAL03 are shown in (b), and they are plotted together in (c). The helical bands originally generated with POLYXA (see Fig. 4-6) were shifted to correspond to what would be obtained with translational periodicity. The most immediate difference is the location of the Fermi levels. Using POLYXA, the Fermi level in (a) is calculated at -3.2150 eV, while Fermi level in (b) obtained using CRYSTAL03 is calculated to be -3.3266 eV, a difference of 0.1116 eV. Therefore, in order to accurately compare the results, the bands obtained with CRYSTAL03 are shifted by 0.1116 eV in (c) in order to match the Fermi level calculated

using POLYXA. The shift in the Fermi level most likely originates from how the two codes truncate the long-range interactions differently.

One important result is that the band gaps obtained within the LDA approximation are essentially the same: roughly 1.10 eV, using POLYXA and CRYSTAL03. This is again in sharp contrast to the values obtained by Erkoç and Kökten; recall they calculated the bandgap of the (4,4) ZnO SWNT to be 0.20 eV, using semiempirical molecular orbital self-consistent field calculations at the level of AM1 method within the RHF formulation.[104]

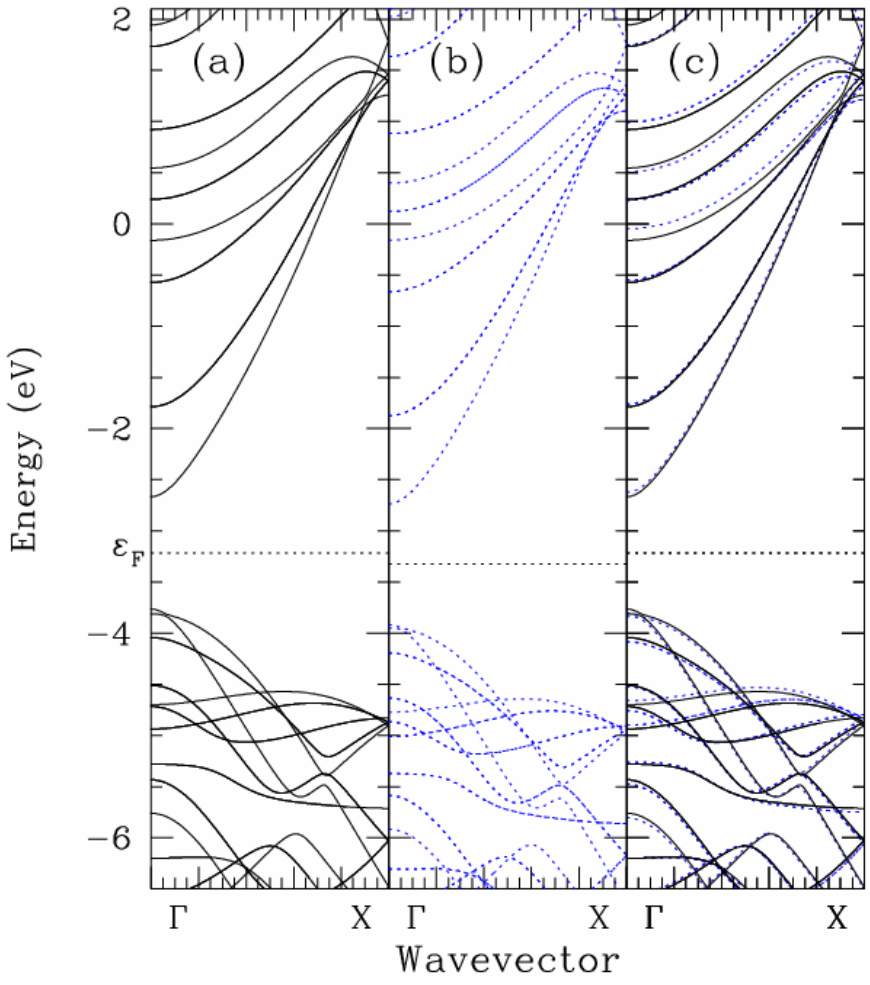

Figure 4-59. Energy bands of the (4,4) ZnO SWNT within the LDA approximation generated with (a) NRL/OSU POLYXA, (b) CRYSTAL03 [11], and (c) NRL/OSU POLYXA and CRYSTAL03 together. The Fermi level obtained with NRL/OSU POLYXA is indicated in (a) at -3.2150 eV, and the Fermi level calculated using CRYSTAL03 is designated in (b) at -3.266 eV. In (c), the bands calculated using CRYSTAL03 are shifted to match the Fermi level for POLYXA (-3.2150 eV).

4.6.5 Graphitic-Like Strips in 1D

Unlike single-wall carbon nanotubes, whose strain energies scale as $1/R^2$, where R is the nanotube radius, such a trend is not present within the results for ZnO SWNTs. (See Fig. 4-3). Therefore, it is not possible simply to extrapolate the expected 2D sheet energy from the single-wall nanotube energies. As a final task using POLYXA, we calculated the total energies of 1D graphitic-like strips, as illustrated in Fig. 4-60. By taking into account total energy changes with increasing strip widths (hence increasing unit cell sizes), we estimated the expected value for ZnO in a 2D graphitic-like sheet to be -1847.7229 Hartrees per ZnO pair.

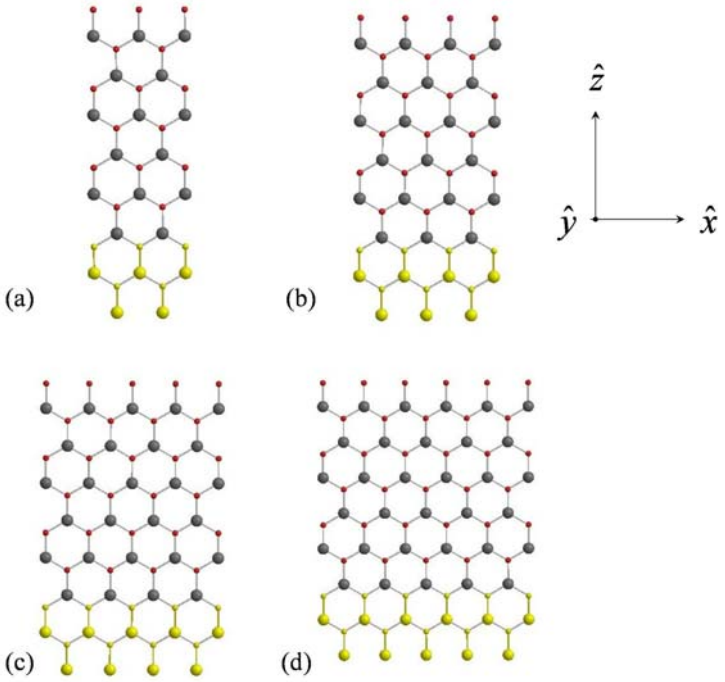

Figure 4-60. Ball and stick models of 1D Graphitic-Like ZnO Strips, periodic along the z-axis, depicted in (a – d) with increasing strip width. The atoms comprising the unit cells are highlighted in yellow.

The energetic results obtained for the 1D graphitic-like ZnO strips are displayed in Table X. The total energies per ZnO pair for the individual strips were what we expected – slightly higher in energy than the single-wall nanotubes. The band gaps exhibit an interesting behavior; they increase somewhat as the strip width increases. This is a topic that may be explored further in future work. The band structures are given in Fig. 4-61. The objective of calculating the 1D strips was to determine the approximate energy of a 2D sheet using the POLYXA code. To calculate the expected sheet total energy (TE), we take the difference between strips and divide by the increase in the number of ZnO unit pairs:

$$TE_{Sheet} \approx \lim_{N \to \infty} \frac{\Delta TE_{Strip}}{\Delta N} \qquad (4.9)$$

The estimated sheet energy, -1847.7229 Hartrees per ZnO pair should be a little lower in energy – on the order of the -1847.7234 value calculated using CRYSTAL03 for the 2D sheet. Calculations with larger strips may be necessary in order to validate the approximation.

1D Strips	*ZnO Pairs N*	*Total Energy (Hartrees/Unit Cell)*	*ΔTE/ΔN (Hartrees/N)*	*Total Energy / ZnO Pair*	*Band Gap (eV)*
(a)	5	-9238.4249	------	-1847.6850	0.8609
(b)	7	-12933.8712	-1847.72315	-1847.6959	0.9130
(c)	9	-16629.3146	-1847.7217	-1847.7016	0.9286
(d)	11	-20324.76045	-1847.7229	-1847.7055	0.9459
Estimated 2D Sheet Energy:		-1847.7229 (Hartrees per ZnO Pair)			

Table X. Total energy and band gap summary of 1D ZnO strips, along with the expected extrapolated energy for a 2D ZnO sheet.

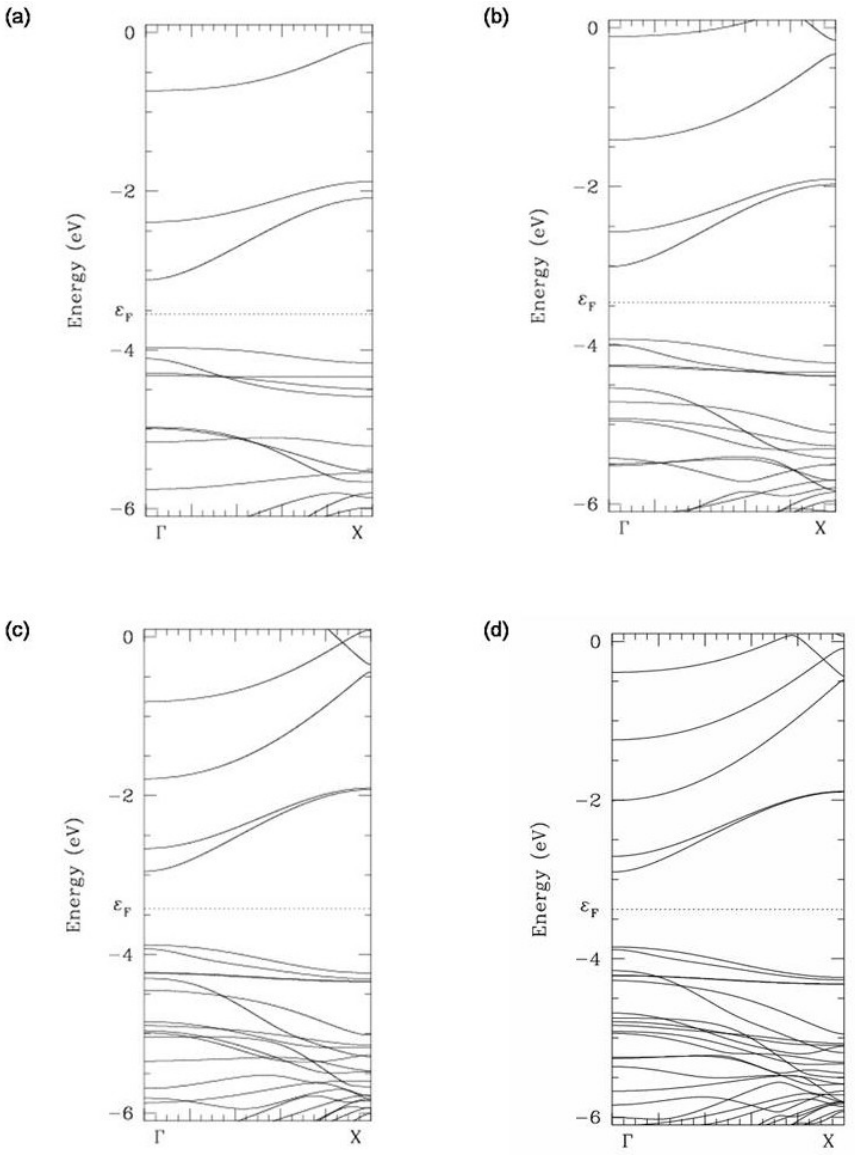

Figure 2.61. Band structures obtained using POLYXA for the ZnO 1D strips in a graphitic configuration with (a) 5, (b) 7, (c) 9, and (d) 11 ZnO atom pairs per unit cell.

4.6.6 Interpretation of Results

Table XI summarizes the energetic results obtained using POLYXA and CRYSTAL03. In section 4.6.4, we discussed the small differences in energy for the (4,4) SWNT as obtained by POLYXA and CRYSTAL03. The values are in fairly good agreement, as the values in total energy for the (4,4) ZnO SWNT are similar, irrespective of the software utilized. However, the difference in total energy between the (4,4) SWNT and the extrapolated 2D sheet, using POLYXA, is roughly 0.0021 Hartrees, while the difference between the (4,4) SWNT and the actual 2D sheet value, obtained with CRYSTAL03, is approximately 0.0007 Hartrees. We would expect these differences to be closer, and further investigation is required to determine the exact mechanism driving these disparities. The most reasonable explanation is that the estimated sheet value obtained using POLYXA is not a good enough approximation; larger strips may be necessary in order to improve the approximation.

ZnO Structure	Total Energy (LDA) (Hartrees/ ZnO)	Band Gap Energy (eV)
POLYXA:		
Single-Wall Nanotubes		
Range:	-1847.7317 to -1847.7136	1.08-1.14
(4,4) SWNT	-1847.7250	1.10
Bulk-Like:		
(1,2) 3yH	-1847.7059	0.5672
(2,3) 6yH	-1847.7051	0.8052
Rocksalt	-1847.7084	0.8039*
Nanowires		
Wurtzite	-1847.7239	0.8073
Rocksalt	-1847.7243	0.5302*
Strips (listed by ZnO Pair)		
5	-1847.6850	0.8609
7	-1847.6959	0.9130
9	-1847.7016	0.9286
11	-1847.7055	0.9459
Extrapolated 2D Sheet:	-1847.7229	---------
XSTAL03		
Bulk	-1847.7496	0.82
Sheet	-1847.7234	1.20
(4,4) SWNT	-1847.7227	1.09

Table XI. Summary of energetic results using POLYXA and CRYSTAL03. * Denotes an indirect band gap.

4.7 Perspectives and Future Work

The geometrical versatility of ZnO nanostructures leads to encouraging results and raises new possibilities. For example, the optical spectra varies from 3.50 eV to 1.70 eV for the second absorption peak as the radius of the single-wall nanotubes varies from 1.2096 Å to 3.1260 Å, independent of chirality. The small sampling of bulk-like nanotubes indicates that a similar trend may be present for the bulk-like nanotube structures derived from the hexagonal wurtzite structure.

Although the optical spectra and energetic results change according to structure, one important feature stays the same: all of the ZnO 1D structures are semiconducting. This is a significant finding, as others have predicted the opposite: Erkoç and Kökten suggested that the (4,0) armchair ZnO nanotube is a conductor while the (4,4) zigzag ZnO nanotube is semiconducting.[104]

Perhaps the most interesting findings within the ZnO study are the changes in optical absorption spectra. We considered the diagonal elements of the dielectric tensor of the form $\varepsilon_2^{\alpha\alpha}(\omega)$. In future work, further improvements can be made by taking into account the local field effects. Hybertsen and Louie discuss an approach within the local-density approximation in which the full dielectric matrix is calculated and information about the local fields is obtained.[110] The off-diagonal elements of the dielectric matrix in reciprocal space contain the information about the local fields, the inhomogeneity of the microscopy response of the electrons. Hybernsten and Louie developed their approach using the perturbative technique of Adler [111] and Wiser [112] for the independent-particle polarizability and the local-density approximation to include the exchange and correlation effects.

CHAPTER 5

FINAL STATEMENTS

As a result of the current boom in nanotechnology, much emphasis has been placed on size confinement effects arising from the changes in properties as the transition is made from bulk to the nanoscale. Even within the nanoscale, further modifications can result simply by varying the geometry of the system. Utilizing our first-principles local density functional approach, adapted for helical symmetry, we carried out two separate studies on silver and zinc oxide one-dimensional systems.

The study involving helical silver single-wall nanotubes presented in Chapter 3 was motivated by experimental work in which helical gold nanowires and a single-wall gold nanotube structure were reported. [12, 13] We examined the electronic structures of a variety of silver single-wall nanotubes and nanowires. We were particularly interested in energetic changes with respect to nanotube radius and the number of conduction channels related to the calculated band structures. Two different approaches were used in modeling the silver structures: conventional helical geometry and strand-by-strand helical geometry. Within the conventional approach, we found that the total energies of the nanotubes do not decrease monotonically as radius increases, as in carbon nanotubes. Within the strand-by-strand approach, however, we find that total energy decreases inversely proportional to the number of strands, falling off further upon adding the last strand and thus completing the nanotube or nanowire structure. In addition, the number

of conduction channels did not always correspond to the number of helical strands. If these structures are produced experimentally in the future, the helical orbital densities may prove to be the most useful result of the study, as other have already suggested that the smallest helical gold nanowires may be good candidates for nanometer-scale solenoids. [72]

The ZnO study carried out in Chapter 4 also involved nanotubes and nanowires. For this study, two different types of nanotubes were taking into account: single-wall nanotubes with structures analogous to carbon nanotubes and bulk-like nanotubes modeled from cutting the core region from a hexagonal wurtzite or rocksalt bulk-like nanowire. All of the nanotube and nanowire structures were found to be semiconducting. The total energies of the nanowires were within a similar range as the single-wall nanotubes. The bulk-like single-wall nanotubes were least energetically favorable.

Results in the optical absorption spectra presented some interesting findings, particularly in regards to the single-wall nanotubes. The optical absorption spectra varied from structure to structure. Although the first peak associated with a direct transition stayed relatively constant, approximately 1.25 eV, the second optical peak resulting from a direct transition displayed a blue-shift from 1.70 eV to 3.50 eV with decreasing nanotube radius.

The final section of Chapter 4 included an assessment of results obtained using our in-house POLYXA code and the commercially available CRYSTAL03 software. The results obtained using the two programs were surprisingly comparable for the (4,4) ZnOSWNT.

BIBLIOGRAPHY

1. Iijima, S., *Helical Microtubules of Graphitic Carbon.* Nature (London), 1991. **354**: p. 56.

2. Law, M., Goldberger, J. and Yang, P., *Semiconductor Nanowires and Nanotubes.* Annu. Rev. Mater. Res., 2004. **34**: p. 82.

3. Tao, A., Kim, F. and Hess, G., *Langmuir-Blodgett Silver Nanowire Monolayer of Molecular Sensing Using Surface-Enhanced Raman Spectroscopy.* Nano Lett., 2003. **3**: p. 1229.

4. Yin, M., Gu, Y., Kuskovsky, I.L. and Andelman, T., *Zinc Oxide Quantum Rods.* J. Am. Chem. Soc., 2004. **126**: p. 6206.

5. Wang, X., Ding, Y., Summers, C.J. and Wang, Z.L., *Large-Scale Synthesis of Six-Nanometer-Wide ZnO Nanobelts.* J. Phys. Chem. B, 2004. **108**: p. 8773.

6. Law, M., Greene, L.E., Johnson, J.C., Saykally, R. and Yang, P., *Nanowire Dye-Sensitized Solar Cells.* Nature Materials, 2005. **4**: p. 455.

7. Gao, P.X., Ding, Y., Mai, W., Hughes, W.L., Lao, C. and Wang, Z.L., *Conversion of Zinc Oxide Nanobelts into Superlattice-Structured Nanohelices.* Science, 2005. **309**: p. 1700.

8. Özgür, Ü., Alivov, Y.I., Liu, C., Teke, A. and Reschikov, M.A., *A Comprehensive Review of ZnO Materials and Devices.* J. Appl. Phys., 2005. **98**: p. 041301.

9. Pearton, S.J., Norton, D.P., Ip, K., Heo, Y.W. and Steiner, T., *Recent Progress in Processing and Properties of ZnO.* Progress in Materials Science, 2005. **50**: p. 293.

10. Service, R.F., *Materials and Biology: Nanotechnology Takes Aim at Cancer.* Science, 2005. **310**: p. 1132.

11. Saunders, V.R., Dovesi, R., Roetti, C., Orlando, R., Zicovich-Wilson, C.M., Harrison, N.M., Doll, K., Civalleri, B., Bush, I., D'Arco, P., and Llunell, M., *CRYSTAL2003 User's Manual*, University of Torino: Torino.

12. Kondo, Y. and Takayanagi, K., *Synthesis and Characterization of Helical Multi-Shell Gold Nanowires.* Science, 2000. **289**: p. 606.

13. Oshima, Y., Onga, A. and Takayanagi, K., *Helical Gold Nanotube Synthesized at 150 K.* Phys. Rev. Lett., 2003. **91**: p. 205503.

14. Elizondo, S.L. and Mintmire, J.W., *Simulations of Metal Nanowires.* Int. J. Quantum Chem., 2005. **105**: p. 772.

15. Elizondo, S.L. and Mintmire, J.W., *First-Principles Study of Helical Silver Single-Wall Nanotubes and Nanowires.* Proceedings of the Materials Research Society, 2005.

16. Elizondo, S.L. and Mintmire, J.W., *Ab initio Study of Helical Silver Single-Wall Nanotubes and Nanowires.* Phys. Rev. B, 2006. **73**(8).

17. Yi, G.-C., Wang, C. and Park, W.I., *ZnO Nanorods: Synthesis, Characteristics and Applications.* Semicond. Sci. Technol., 2005. **20**: p. S22.

18. Arnold, M.S., Avouris, P., Pan, Z.W. and Wang, Z.L., *Field-Effect Transistors Based on Single Semiconducting Oxide Nanobelts.* J. Phys. Chem. B, 2003. **107**: p. 659.

19. Huang, M.H., Mao, M., Feick, H., Yan, H.Q., Wu, Y.Y., Kind, H., Weber, E., Russo, R. and Yang, P.D., *Room-Temperature Ultraviolet Nanowire Nanolasers.* Science, 2001. **292**: p. 1897.

20. Keem, K., Kim, H., Kim, G.T., Lee, J.S., Min, B., Cho, K., Sung, M.Y. and Kim, S., *Photocurrent in ZnO Nanowires Grown from Au Electrodes.* Appl. Phys. Lett., 2004. **84**: p. 4376.

21. Lee, C.J., Lee, T.J., Lyu, S.C., Zhang, Y., Ruh, H. and Lee, H.J., *Field Emission From Well-Aligned Zinc Oxide Nanowires Grown at Low Temperature.* Appl. Phys. Lett., 2002. **81**: p. 3648.

22. Park, J.H., Choi, H.J., Choi, Y.J., Sohn, S.H. and Park, J.G., *Ultrawide ZnO Nanosheets.* J. Mater. Chem., 2004. **14**: p. 35.

23. Park, J.H., Choi, H.J. and Park, J.G., *Scaffolding and Filling Process: A New Type of 2D Crystal Growth.* J. Cryst. Growth, 2004. **263**: p. 237.

24. Park, W.I., Jun, Y.H., Jung, S.W. and Yi, G.C., *Excitonic Emissions Observed in ZnO Single Crystal Nanorods.* Appl. Phys. Lett., 2003. **82**: p. 964.

25. Wang, Z.L., *Nanostructures of Zinc Oxide.* Materials Today, 2004. **7**: p. 26.

26. Zhang, X., Zhang, Y., Xu, J., Wang, Z., Chen, X. and Yu, D., *Peculiar ZnO Nanopushpins and Nanotubes Synthesized via Simple Thermal Evaporation.* Appl. Phys. Lett., 2005. **87**(123111): p. 123111.

27. Claeyssens, F., Freeman, C.L., Allan, N.L., Sum, Y., Ashfold, M.N.R. and Harding, J.H., *Growth of ZnO Thin Films - Experiment and Theory.* J. Mater. Chem., 2004. **15**: p. 139.

28. Ehrenreich, H. and Cohen, M.H., *Self-Consistent Field Approach to the Many-Electron Problem.* Physical Review, 1959. **115**: p. 786.

29. Elizondo, S.L., *Simulations of Metal Nanowires*, in *Department of Physics*. 2005, Oklahoma State University: Stillwater, OK.

30. Miao, M.S., Camp, P.E.V., Doren, V.E., Ladik, J.J. and Mintmire, J.W., *Conformation and Electronic Structure of Polyethlene: A Density-Functional Approach.* Phys. Rev. B, 1996. **54**: p. 10430.

31. Mintmire, J.W., in *Density Functional Methods in Chemistry*, J.K. Labanowski, Editor. 1990, Springer-Verlag: Berlin. p. 125.

32. White, C.T. and Mintmire, J.W., *Fundamental Properties of Single-Wall Carbon Nanotubes.* J. Phys. Chem. B, 2005. **109**: p. 52.

33. Fujita, H. and Imamura, A., *Electronic Structures of Polymers Using the Tight-Binding Approximation. II. Polyethylene and Polyglycine by the CNDO Method.* Journal of Chemical Physics, 1970. **53**: p. 4555.

34. Imamura, A., *Electronic Structures of Polymers Using the Tight-Binding Approximation. I. Polyethlyene by the Extended Huckel Method.* Journal of Chemical Physics, 1970. **52**: p. 3168.

35. Robertson, D.H., Brenner, D.W. and Mintmire, J.W., *Energetics of Nanoscale Graphite Tubules.* Phys. Rev. B, 1992. **45**: p. 12592.

36. Jensen, F., *Introduction to Computational Chemistry*. 1999, West Sussex, England: John Wiley & Sons, Ltd.

37. Leach, A.R., *Molecular Modelling Principles and Applications*. 2nd ed. 2001, Essex, England: Pearson Education.

38. Schatz, G.C. and Ratner, M.A., *Quantum Mechanics in Chemistry*. 2002, Mineola, New York: Dover Publications, Inc.

39. Slater, J.C., *Solid-State and Molecular Theory: A Scientific Biography*. 1975, New York: John Wiley & Sons, Inc.

40. Szabo, A. and Ostlund, N.S., *Modern Quantum Chemistry Introduction to Advanced Electronic Structure Theory*. 1996, Mineola, New York: Dover Publications, Inc.

41. Slater, J.C., *A Simplification of the Hartree-Fock Method.* Physical Review, 1951. **81**(385).

42. Hohenberg, P. and Kohn, W., *Inhomogeneous Electron Gas.* Physical Review 1964. **136**: p. B864.

43. Kohn, W. and Sham, L.J., *Self-Consistent Equations Including Exchange and Correlation Effects.* Physical Review, 1965. **140**: p. A1133.

44. Marder, M.P., *Condensed Matter Physics*. . 2000, New York: John Wiley and Sons, Inc.

45. Kittel, C., *Introduction to Solid State Physics*. seventh ed. 1996, New York: John Wiley and Sons, Inc.

46. Mintmire, J.W. and White, C.T., *Local-Density-Functional Approach to All-trans-polyacetylene.* Phys. Rev. B, 1983. **28**: p. 3283.

47. Mintmire, J.W. and White, C.T., *Xα Approach for the Determination of the Electronic and Geometric Structure of Polyacetylene and Other Chain Polymers.* Phys. Rev. Lett., 1983. **50**: p. 101.

48. Mintmire, J.W. and White, C.T., *Theoretical Treatment of the Dielectric Response of all-trans-polyacetylene.* Phys. Rev. B, 1983. **27**: p. 1447.

49. Mintmire, J.W. and White, C.T., *Local-Density-Functional Results for the Dimerization of trans-polyacetylene: Relationship to the Band-Gap Problem.* Phys. Rev. B, 1987. **35**: p. 4180.

50. Mulliken, R.S., *Electronic Population Analysis on LCAO-MO Molecular Wave Functions. I.* J. Chem. Phys., 1955. **23**: p. 1833.

51. Mintmire, J.W. and White, C.T., *Electronic Structure Simulations of Carbon Nanotubes.* Synth. Met., 1996. **77**: p. 231.

52. Mintmire, J.W. and Dunlap, B.I., *Fitting the Coulomb Potential Variationally in Linear-Combination-of-Atomic-Orbitals Density-Functional Calculations.* Phys. Rev. A, 1982. **25**: p. 88.

53. Harrison, W.A., *Electronic Structure and the Properties of Solids*. 1980, San Fransisco: Freeman.

54. Dunlap, B.I., Connolly, J.W.D. and Sabin, J.R., *On Some Approximations in Applications of Xα Theory.* J. Chem. Phys., 1979. **71**: p. 3396.

55. Dunlap, B.I., Connolly, J.W.D. and Sabin, J.R., *On First-Row Diatomic Molecules and Local Density Models.* J. Chem. Phys., 1979. **71**: p. 4993.

56. Sambe, H. and Felton, R., *Calculation of the Ionization Potentials of Ozone and Ammonia by a LCAO-X Method.* J. Chem. Phys., 1974. **61**: p. 3862.

57. Sambe, H. and Felton, R., *A New Computational Approach to Slater's SCF–X Equation.* J. Chem. Phys., 1975. **62**: p. 1122.

58. Whitten, J.L., *Coulombic potential energy integrals and approximations.* J. Chem. Phys., 1973. **58**: p. 4496.

59. Dunlap, B.I. and Cook, M., *LCAO-X-Alpha Calculations of Rotational Energy Barriers - Prototypes of Chemical-Reactions.* Int. J. Quantum Chem., 1986. **29**(4): p. 767.

60. Becke, A.D., *A multicenter numerical integration scheme for polyatomic molecules.* J. Chem. Phys., 1988. **88**: p. 2547.

61. Hong, B.H., Bae, S.C., Lee, C., Jeong, S. and Kim, K.S., *Ultrathin Single-Crystalline Silver Nanowire Arrays Formed in Ambient Solution Phase.* Science, 2001. **294**: p. 348.

62. Nilius, N., Wallis, T.M. and Ho, W., *Development of One-Dimensional Band Structure in Artificial Gold Chains.* Science, 2002. **297**: p. 1853.

63. Ohnishi, H., Kondo, Y. and Takayanagi, K., *Quantized Conductance Through Individual Rows of Suspended Gold Atoms.* Nature (London), 1998. **395**: p. 780.

64. Rodrigues, V., Bettini, J., Rocha, A.R., Rego, L.G.C. and Ugarte, D., *Quantum Conductance in Silver Nanowires: Correlation Between Atomic Structures and Transport Properties.* Phys. Rev. B, 2002. **65**: p. 153402.

65. Wallis, T.M., Nilius, N. and Ho, W., *Electronic Density Oscillations in Gold Chains Assembled Atom by Atom.* Phys. Rev. Lett., 2002. **89**: p. 236802.

66. Watanabe, M., Minoda, H. and Takayanagi, K., *Fabrication of Gold Nanowires Using Contact Mode Atomic Force Microscope.* Jpn. J. Appl. Phys., Part 1, 2004. **43**: p. 6347.

67. Xiong, Y., Xie, Y., Wu, C., Yang, J., Li, Z. and Xu, F., *Formation of Silver Nanowires Through a Sandwiched Reduction Process.* Adv. Mater., 2003. **15**: p. 405.

68. Zhao, Q., Qiu, J., Zhao, C., Hou, L. and Zhu, C., *Synthesis and Formation Mechanism of Silver Nanowires by a Templateless and Seedless Method.* Chem. Lett., 2005. **34**: p. 30.

69. Smit, R.H.M., Untiedt, C., Yanson, A.I. and Ruitenbeek, J.M.v., *Common Origin for Surface Reconstruction and the Formation of Chains of Metal Atoms.* Phys. Rev. Lett., 2001. **87**: p. 266102.

70. Agrawal, B.K., Agrawal, S. and Singh, S., *Ab initio Study of the Structural and Electronic Properties of Very Thin Silver Nanowires.* J. Nanosci. Nanotech., 2005. **5**: p. 635.

71. Hasegawa, A., Yoshizawa, K. and Hirao, K., *Electronic Structures of Gold Nanowires.* Chem. Phys. Lett., 2001. **93**: p. 196807.

72. Ono, T. and Hirose, K., *First-Principles Study of Electron - Conduction Properties of Helical Gold Nanowires.* Phys. Rev. Lett., 2005. **94**: p. 206806.

73. Senger, R.T., Dag, S. and Ciraci, S., *Chiral Single-Wall Gold Nanotubes.* Phys. Rev. Lett., 2004. **93**: p. 196807.

74. Tosatti, E., Prestipino, S., Kostlmeier, S., Corso, A.D. and Tolla, F.D.D., *String Tension and Stability of Magic Tip-Suspended Nanowires.* Science 2001. **291**: p. 288.

75. Yang, C.-K., *Theoretical Study of the Single-Walled Gold (5,3) Nanotube.* Appl. Phys. Lett., 2004. **85**: p. 2923.

76. Zhao, J., Buia, C., Han, J. and Lu, J.P., *Quantum Transport Properties of Ultrathin Silver Nanowires.* Nanotechnology, 2003. **14**: p. 501.

77. Tekman, E. and Ciraci, S., *Theoretical Study of Transport Through a Quantum Point Contact.* Phys. Rev. B, 1991. **109**: p. 52.

78. Wees, B.J.v., Houten, H.v., Beenakker, C.W.J., Williamson, J.G., Kouwenhoven, L.P., Marel, D.v.d. and Foxon, C.T., *Quantized Conductance of Point Contacts in a Two-Dimensional Electron Gas.* Phys. Rev. Lett., 1988. **60**: p. 848.

79. Dobbs, K.D. and Hehre, W.J., *Molecular Orbital Theory of the Properties of Inorganic and Organometallic Compounds. 6. Extended Basis Sets for Second-Row Transition Metals.* J. Comput. Chem., 1987. **8**: p. 880.

80. Elizondo, S.L., *Simulations of Metal Nanowires*, in *Department of Physics*. 2005, Oklahoma State University: Stillwater, OK.

81. Douglas, M. and Kroll, N.M., *Quantum Electrodynamical Corrections to the Fine Structure of Helium.* Annals of Physics, 1974. **82**: p. 89.

82. Hay, P.J. and Wadt, W.R., *Ab initio Effective Core Potentials for Molecular Calculations. Potentials for the Transition Metal Atoms Sc to Hg.* J. Chem. Phys., 1985. **82**: p. 270.

83. Hess, B.A., *Applicability of the No-Pair Equation with Free-Particle Projection Operators to Atomic and Molecular Structure Calculations.* Phys. Rev. A, 1985. **32**: p. 756.

84. Hess, B.A., *Relativistic Electronic-Structure Calculations Employing a Two-Component No-Pair Formalism with External-Field Projection Operators.* Phys. Rev. A, 1986. **33**: p. 3742.

85. Wolf, A., Reiher, M. and Hess, B.A., *The Generalized Douglas-Kroll Transformation.* J. Chem. Phys., 2002. **117**: p. 9215.

86. Wang, Z.L. and Song, J., *Piezoelectric Nanogenerators Based on Zinc Oxide Nanowire Arrays.* Science, 2006. **312**: p. 242.

87. Xing, Y.J., Xi, Z.H., Zhang, X.D., Song, J.H., Wang, R.M., Xu, J., Xue, Z.Q. and Yu, D.P., *Nanotubular Structures of Zinc Oxide.* Solid State Commun., 2004. **129**: p. 671.

88. Ng, H.T., Chen, B., Li, J., Han, J. and Meyyappan, M., *Optical Properties of Single-Crystalline ZnO Nanowires on m-Sapphire.* Appl. Phys. Lett., 2003. **82**: p. 2023.

89. Vayssieres, L., *Growth of Arrayed Nanorods and Nanowires of ZnO From Aqueous Solutions.* Adv. Mater., 2003. **15**: p. 464.

90. Kong, X., Sun, X., Li, X. and Li, Y., *Catalytic Growth of ZnO Nanotubes.* Mater. Chem. Phys., 2003. **82**: p. 997.

91. Wang, R.M., Xing, Y.J., Xu, J. and Yu, D.P., *Fabrication and Microstructure Analysis on Zinc Oxide Nanotubes.* New Journal of Physics, 2003. **5**: p. 115.

92. Xu, W.Z., Ye, Z.Z., Ma, D.W. and Lu, H.M., *Quasi-Aligned ZnO Nanotubes Grown on Si Substrates.* Appl. Phys. Lett., 2005. **87**: p. 093110.

93. Wang, R.-C., Liu, C.-P., Huang, J.-L. and Chen, S.-J., *Growth and Feld-Emission Properties of Single-Crystalline Conic ZnO Nanotubes.* Nanotechnology, 2006. **17**: p. 753.

94. Wu, J.-J., Liu, S.-C., Wu, C.-T., Chen, K.-H. and Chen, L.-C., *Heterostructures of ZnO-Zn Coaxial Nanocables and ZnO Nanotubes.* Appl. Phys. Lett., 2002. **81**: p. 1312.

95. Zhang, B.P., Binh, N.T., Wakatsuki, K., Segawa, Y., Yamada, Y., Usami, N., Kawasaki, M. and Koinuma, H., *Formation of Highly Aligned ZnO Tubes on Sapphire (0001) Substrates.* Appl. Phys. Lett., 2004. **84**: p. 4098.

96. Hu, J.Q. and Bando, Y., *Growth and Optical Properties of Single-Crystal Tubular ZnO Whiskers.* Appl. Phys. Lett., 2003. **82**: p. 1401.

97. Hu, J.Q., Li, Q., Meng, X.M., Lee, C.S. and Lee, S.T., *Thermal Reduction Route to the Fabrication of Coaxial Zn/ZnO Nanocables and ZnO Nanotubes.* Chem. Mater., 2003. **15**: p. 305.

98. Jian-Feng, Y., You-Ming, L., Hong-Wei, L., Yi-Chun, L., Bing-Hui, L., Xi-Wu, F. and Jun-Ming, Z., *Growth and Properties of ZnO Nanotubes Grown on Si(111) Substrate by Plasma-Assisted Molecular Beam Epitaxy.* J. Cryst. Growth, 2005. **280**: p. 206.

99. Li, Q., Kumar, V., Li, Y., Zhang, H., Marks, T.J. and Chang, R.P.H., *Fabrication of ZnO Nanorods and Nanotubes in Aqueous Solution.* Chem. Mater., 2005. **17**: p. 1001.

100. Liang, H.W., Lu, Y.M., Shen, D.Z., Li, B.H., Zhang, Z.Z., Shan, C.X., Zhang, J.Y., Fan, X.W. and Du, G.T., *Growth of Vertically Aligned Single Crystal ZnO Nanotubes by Plasma-Molecular Beam Epitaxy.* Solid State Commun., 2006. **137**: p. 182.

101. Sun, Y., Fuge, G.M., Fox, N.A., Riley, D.J. and Ashfold, M.N.R., *Sythesis of Aligned Arrays of Ultrathin ZnO Nanotubes on a Si Wafer Coated with a Thin ZnO Film.* Adv. Mater. (Weinheim, Fed. Repub. Ger.), 2005. **17**: p. 2477.

102. Wu, D., Huang, L., Wang, Q., Zhao, X., Li, A., Chen, Y. and Ming, N., *Bell-Mouthed Single-Crystalline Tubular ZnO Prepared by a Soft Solution Method.* Mater. Chem. Phys., 2006. **96**: p. 51.

103. Xing, Y.J., Xi, Z.H., Xue, Z.Q., Zhang, X.D., Song, J.H., Wang, R.M., Xu, J., Song, Y., Zhang, S.L. and Yu, D.P., *Optical Properties of the ZnO Nanotubes Synthesized via Vapor Phase Growth.* Appl. Phys. Lett., 2003. **83**: p. 1689.

104. Erkoc, S. and Kokten, H., *Structural and Electronic Properties of Single-Wall ZnO Nanotubes.* Physica E, 2005. **28**: p. 162.

105. Hehre, W.J., Ditchfield, R. and Pople, J.A., *Self-Consistent Molecular Orbital Methods. XII. Further Extensions of Gaussian-Type Basis Sets for Use in Molecular Studies of Organic Molecules.* J. Chem. Phys., 1972. **56**: p. 2257.

106.\ Cabria, I. and Mintmire, J.W., *Stability and Electronic Structure of Phosphorus Nanotubes.* Europhys. Lett., 2004. **65**: p. 82.

107. Milosevic, I., Stevanovic, V., Tronc, P. and Damnjanovic, M., *Symmetry of Zinc Oxide Nanostructures.* J. Phys.: Condens. Matter, 2006. **18**: p. 1939.

108. Karazhanov, S.Z., Ravindran, P., Kjekhus, A., Fjellvag, H., Grossner, U. and Svensson, B.G., *Electron Structure and Band Parameters for ZnX (X = O, S, Se, Te).* J. Cryst. Growth, 2006. **287**: p. 162.

109. Vogel, D., Kruger, P. and Pollmann, J., *Ab initio Electronic-Structure Calculations for II-VI Semiconductors Using Self-Interaction-Corrected Pseudopotentials.* Physical Review B, 1995. **52**: p. R14316.

110. Hybertsen, M.S. and Louie, S.G., *Ab initio Static Dielectric Matrices from the Density-Functional Approach. I. Formulation and Application to Semiconductors and Insulators.* Phys. Rev. B, 1987. **35**: p. 5585.

111. Adler, S.L., *Quantum Theory of the Dielectric Constant in Real Solids.* Physical Review, 1962. **126**: p. 413.

112. Wiser, N., *Dielectric Constant with Local Field Effects Included.* Physical Review, 1963. **129**: p. 62.

VITA

SHELLY LEIGH ELIZONDO

Candidate for the Degree of

Doctor of Philosophy

Thesis: AB INITIO STUDY OF INORGANIC NANOWIRES

Major Field: Photonics

Biographical:

Personal Data: Born in Enid, Oklahoma, on June 29, 1977, the daughter of Lonnie and Sue Mathis.

Education: Received Bachelor of Science degree in Mathematics, Economics, and Statistics from the University of Central Oklahoma in December 2000. Received a Master of Science degree in Natural and Applied Sciences from Oklahoma State University in May 2005. Completed the requirements for the Doctor of Philosophy degree with a major in Photonics at Oklahoma State University in July 2006.

Experience: Employed by Oklahoma State University, Department of Physics as a graduate research assistant and graduate teaching assistant January 2003 to present.

Professional Memberships: American Physical Society

Name: Shelly Elizondo Date of Degree: July, 2006

Institution: Oklahoma State University Location: Stillwater, Oklahoma

Title of Study: AB INITIO STUDY OF INORGANIC NANOWIRES

Pages in Study: 171 Candidate for the Degree of Doctor of Philosophy

Major Field: Photonics

Scope and Method of Study: In this work, we report simulations of the electronic structure pertaining to two types of quasi-one-dimensional nanostructures: silver and zinc-oxide nanotubes and nanowires. The electronic structures were investigated within a first-principles, all-electron, self-consistent local density functional approach (LDF) adapted for helical symmetry. Two different approaches were used in modeling the silver structures: conventional helical geometry and strand-by-strand helical geometry. Within the silver study, we were particularly interested in energetic changes with respect to nanotube radius and the number of conduction channels related to the calculated band structures. Within the zinc oxide study, we were interested in the changes of optical properties in response to changes in nanotube diameter, and as such, the optical cross sections of the zinc-oxide nanotubes and nanowires are calculated using an Ehrenreich – Cohen formalism.

Findings and Conclusions:

For the silver study, we found that the total energies of the nanotubes do not decrease monotonically as radius increases, as in carbon nanotubes. Within the strand-by-strand approach, we found that the total energy decreases inversely proportional to the number of strands, falling off further upon adding the last strand and thus completing the nanotube or nanowire structure. In addition, the number of conduction channels did not always correspond to the number of helical strands. For the zinc oxide study, all single-wall nanotubes were semiconducting with little variation in the band gap. The optical absorption spectra exhibited a fascinating trend. While the first peak associated with a direct transition stays relatively stationary, roughly 1.25 eV, as nanotube radius varies, the second optical peak resulting from a direct transition displays a blue-shift from 1.70 eV to 3.50 eV as nanotube radius decreases from 1.20 Å to 3.13 Å. The optical absorption spectra of the zinc oxide nanostructures proved very sensitive to even the smallest structural deformations.

Advisor's Approval: Dr. John Mintmire